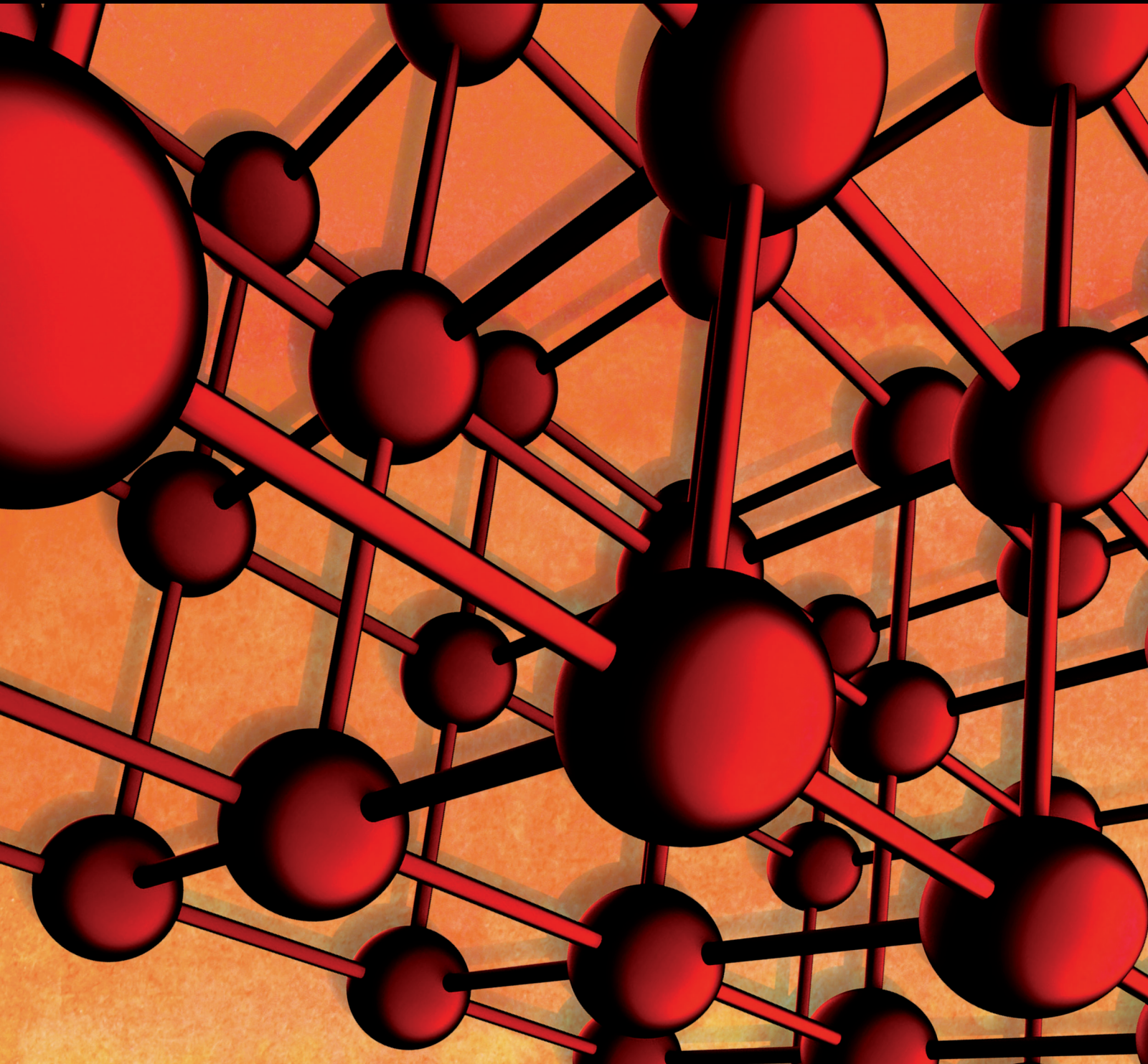


Advances in Materials Science and Engineering

Advances in Friction Welding

Guest Editors: Wenyu Li, Achilleas Vairis, and R. Mark Ward





Advances in Friction Welding

Advances in Materials Science and Engineering

Advances in Friction Welding

Guest Editors: Wenya Li, Achilleas Vairis, and R. Mark Ward



Copyright © 2014 Hindawi Publishing Corporation. All rights reserved.

This is a special issue published in “Advances in Materials Science and Engineering.” All articles are open access articles distributed under the Creative Commons Attribution License, which permits unrestricted use, distribution, and reproduction in any medium, provided the original work is properly cited.

Editorial Board

K. G. Anthymidis, Greece
Robert S. Averbach, USA
Amit Bandyopadhyay, USA
Zoe Barber, UK
Yucel Birol, Turkey
Susmita Bose, USA
Steve Bull, UK
Peter Chang, Canada
Daolun Chen, Canada
Manish U. Chhowalla, USA
S. Chinnappanadar, India
Chi-Wai Chow, Taiwan
Jie Dai, Singapore
Chapal K. Das, India
J. Paulo Davim, Portugal
Seshu B. Desu, USA
Yong Ding, USA
Wei Feng, China
Sergi Gallego, Spain
Lian Gao, China
Hiroki Habazaki, Japan
Richard Hennig, USA
Dachamir Hotza, Brazil
Chun-Hway Hsueh, Taiwan
Shyh-Chin Huang, Taiwan
Rui Huang, USA
Wei Huang, China
Baibiao Huang, China
Jacques Huot, Canada
Jae-Ho Kim, Korea
Jaehwan Kim, Korea
Sridhar Komarneni, USA
Hongchao Kou, China
Prashant Kumta, USA
Jui-Yang Lai, Taiwan

Pavel Lejcek, Czech Republic
Markku Leskela, Finland
Bin Li, China
Feng Li, China
Ying Li, USA
Hai Lin, China
Yuanhua Lin, China
Zhimin Liu, China
Ying Liu, USA
Yuan Liu, China
Gang Liu, China
Tao Liu, China
Jun Liu, China
Meilin Liu, Georgia
Wei Liu, France
Yunqi Liu, China
Maria A. Loi, The Netherlands
Haiming Lu, China
Peter Majewski, Australia
Shuichi Miyazaki, Japan
Hossein Moayed, Malaysia
Paul Munroe, Australia
Ali Nazari, Iran
Luigi Nicolais, Italy
Tsutomu Ohzuku, Japan
Xiaoqing Pan, USA
Ganapathiraman Ramanath, USA
Raju V. Ramanujan, Singapore
Manijeh Razeghi, USA
S.M. Sapuan, Malaysia
Jainagesh A. Sekhar, USA
Jiangbo Sha, China
Liyuan Sheng, China
You Song, China
Aloysius Soon, Korea

Charles C. Sorrell, Australia
Steven L. Suib, USA
Sam-Shajing Sun, USA
Weihua Tang, China
Somchai Thongtem, Thailand
Achim Trampert, Germany
Vladimir Tsukruk, USA
Krystyn Van Vliet, USA
Rui Vilar, Portugal
Min Wang, China
Hao Wang, China
Rui Wang, China
Rong Wang, USA
Qiang Wang, China
Lu Wei, China
Jörg M K Wieszorek, USA
Wei Wu, USA
Gongnan Xie, China
Aiguo Xu, China
Hemmige S. Yathirajan, India
Jianqiao Ye, UK
Wenbin Yi, China
Jinghuai Zhang, China
Jing Zhang, China
Li Zhang, China
Tao Zhang, China
Bin Zhang, China
Jian Zhang, Singapore
Jun Zhang, China
Yufeng Zhang, China
Kai Zhang, China
Kai Zhang, China
Rui Zhang, China
Ming-Xing Zhang, Australia
Wei Zhou, China

Contents

Advances in Friction Welding, Wenya Li, Achilleas Vairis, and R. Mark Ward
Volume 2014, Article ID 204515, 1 page

Friction Stir Spot Welding: A Review on Joint Macro- and Microstructure, Property, and Process Modelling, X. W. Yang, T. Fu, and W. Y. Li
Volume 2014, Article ID 697170, 11 pages

Processing Parameters Influence on Wear Resistance Behaviour of Friction Stir Processed Al-TiC Composites, E. T. Akinlabi, R. M. Mahamood, S. A. Akinlabi, and E. Ogunmuyiwa
Volume 2014, Article ID 724590, 12 pages

Advantages of the Green Solid State FSW over the Conventional GMAW Process, Hasan I. Dawood, Kahtan S. Mohammed, and Mumtaz Y. Rajab
Volume 2014, Article ID 105713, 10 pages

Friction Welding of Aluminium and Aluminium Alloys with Steel, Andrzej Ambroziak, Marcin Korzeniowski, Paweł Kustroń, Marcin Winnicki, Paweł Sokołowski, and Ewa Harapińska
Volume 2014, Article ID 981653, 15 pages

The Importance of Materials Data and Modelling Parameters in an FE Simulation of Linear Friction Welding, R. Turner, F. Schroeder, R. M. Ward, and J. W. Brooks
Volume 2014, Article ID 521937, 8 pages

Mechanical Behaviors of Friction Stir Spot Welded Joints of Dissimilar Ferrous Alloys under Opening-Dominant Combined Loads, Md. Abu Mowazzem Hossain, Md. Tariqul Hasan, Sung-Tae Hong, Michael Miles, Hoon-Hwe Cho, and Heung Nam Han
Volume 2014, Article ID 572970, 12 pages

Upset Prediction in Friction Welding Using Radial Basis Function Neural Network, Wei Liu, Feifan Wang, Xiawei Yang, and Wenya Li
Volume 2013, Article ID 196382, 9 pages

Editorial

Advances in Friction Welding

Wenya Li,¹ Achilleas Vairis,² and R. Mark Ward³

¹ Shaanxi Key Laboratory of Friction Welding Technologies, School of Materials Science and Engineering, Northwestern Polytechnical University, Xi'an, Shaanxi 710072, China

² Department of Mechanical Engineering, School of Technology, TEI of Crete, P.O. Box 1939, Estavromenos, 71004 Heraklion, Greece

³ School of Metallurgy and Materials, University of Birmingham, Birmingham B15 2TT, UK

Correspondence should be addressed to Wenya Li; liwy@nwpu.edu.cn

Received 3 June 2014; Accepted 3 June 2014; Published 3 July 2014

Copyright © 2014 Wenya Li et al. This is an open access article distributed under the Creative Commons Attribution License, which permits unrestricted use, distribution, and reproduction in any medium, provided the original work is properly cited.

There is a continual requirement to make things perform better, be more predictably reliable, cost less, and use less energy. This often leads to requirements to make components for them that are complex shapes or that have properties that vary from one location to another. These requirements are often difficult or expensive to satisfy by conventional machining and mechanical processing, but joining allows us to make complex shapes, potentially of materials with different properties. The disadvantage is that, often, joints require mass to be added to a design to carry the locally increased forces surrounding the joint. Alternatively the joint must be prepared and produced very carefully and may still have properties below those of the parent material. Extra mass or reduced properties (again requiring extra mass) increase the raw material costs and typically reduce the energy efficiency of the final product.

Friction welding offers an extremely promising way to make joints with minimal requirements for extra mass and with extremely good final product properties showing very low distortion. Particularly for metals appealing advantages are the self-cleaning nature of the process as it expels surface contamination that might ultimately lead to, for example, fatigue damage in service and the avoidance of melting at the joining interface which reduces metallurgical problems. All processes, to varying degree of course, are very reliable and repeatable, with few requirements in terms of nondestructive testing usually.

Considerable work on friction welding has been undertaken at the Universities of Birmingham, Manchester, and Cranfield, TWI (UK), Northwestern Polytechnical University

(China), Wroclaw University of Technology (Poland), University of Johannesburg (South Africa), University of Ulsan (South Korea), and Universiti Malaysia Perlis (Malaysia), among others. Inertia and rotary friction welding have been used since World War II in a wide range of applications such as shafts and valves, while linear friction welds are already being used in high performance parts in aircraft engines. The friction stir welding family of applications (friction stir welding, friction stir spot welding, friction stir processing, etc.) is used in the manufacture of structures utilising aluminium alloy plates of every grade.

The seven papers in this special edition cover a wide range of applications of the friction welding family ranging from rotary/inertia and linear to stir and stir spot welding, as well as friction stir processing. The topics of these papers are about dissimilar material joints, joint microstructure, mechanical properties, and various modelling techniques. We hope that you will find them useful in deciding how friction joining can be used in your applications.

*Wenya Li
Achilleas Vairis
R. Mark Ward*

Review Article

Friction Stir Spot Welding: A Review on Joint Macro- and Microstructure, Property, and Process Modelling

X. W. Yang,¹ T. Fu,¹ and W. Y. Li^{1,2}

¹ State Key Laboratory of Solidification Processing, Shaanxi Key Laboratory of Friction Welding Technologies, Northwestern Polytechnical University, Xi'an 710072, China

² School of Materials Science and Engineering, Northwestern Polytechnical University, Xi'an 710072, China

Correspondence should be addressed to W. Y. Li; liwy@nwpu.edu.cn

Received 7 March 2014; Accepted 23 April 2014; Published 25 June 2014

Academic Editor: Achilleas Vairis

Copyright © 2014 X. W. Yang et al. This is an open access article distributed under the Creative Commons Attribution License, which permits unrestricted use, distribution, and reproduction in any medium, provided the original work is properly cited.

Friction stir spot welding (FSSW) is a very useful variant of the conventional friction stir welding (FSW), which shows great potential to be a replacement of single-point joining processes like resistance spot welding and riveting. There have been many reports and some industrial applications about FSSW. Based on the open literatures, the process features and variants, macro- and microstructural characteristics, and mechanical properties of the resultant joints and numerical simulations of the FSSW process were summarized. In addition, some applications of FSSW in aerospace, aviation, and automobile industries were also reviewed. Finally, the current problems and issues that existed in FSSW were indicated.

1. Introduction

Recently, lightweight metals such as aluminium alloys are increasingly used, especially in aerospace and automotive industries, where weight saving is extremely important [1]. Resistance spot welding, laser spot welding, and riveting have been widely used for aluminium alloys sheet assemblies. However, the conventional resistance spot welding has disadvantages such as consumption of tool during joining, large heat distortion, and poor weld strength in joints; porosity defects cannot be avoided by laser spot welding; riveting will increase the weight of components and the drilling needed will increase the cost [2]. Hence, new spot welding processes are required for joining parts made of aluminium alloys.

Friction stir welding (FSW) was developed by TWI in 1991 [3, 4]. It offers various advantages such as small thermal deformation, sound mechanical properties, fine and uniform weld microstructure, high welding efficiency, and green welding process, which has received considerable attention in welding aluminium alloys [5–7]. As FSW is developed, studies on FSW of other advanced materials, such as magnesium alloys, copper alloys, titanium alloys, steels, and superalloys, have been reported.

As a variant of FSW, friction stir spot welding (FSSW) has been proposed to realise a spot weld. It shows great potential to be a replacement of single-point joining processes like resistance spot welding and riveting, and it has wider applications in aerospace, aviation, and automobile fields [7]. Up to now, there are many reports about FSSW, which mainly focus on the process, microstructural characteristics, mechanical properties, and numerical simulations. This review will summarise these aspects about FSSW.

2. The Processes of FSSW

Conventional FSSW was invented by Mazda Motor Corporation in 1993 [8], which is similar in concept and appearance to its predecessor FSW. As shown in Figure 1, the FSSW process consists of three stages: plunging, stirring, and retracting [9]. The process starts with the tool rotating at a high angular speed. Then the tool is forced into workpieces until the tool shoulder contacts the top surface of the upper workpiece to form a weld spot. The plunging movement of the tool causes the expelling of materials. After plunging, the stirring stage starts when the tool reaches a predetermined depth. In this stage, the tool keeps rotating in the workpieces. Frictional

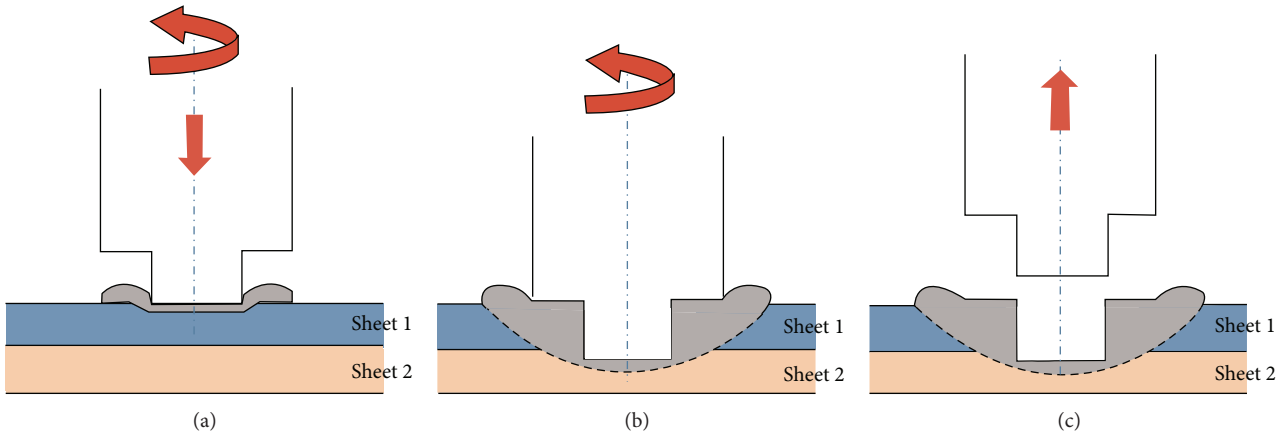


FIGURE 1: Illustration of the FSSW process: (a) plunging, (b) stirring, and (c) retracting [9].

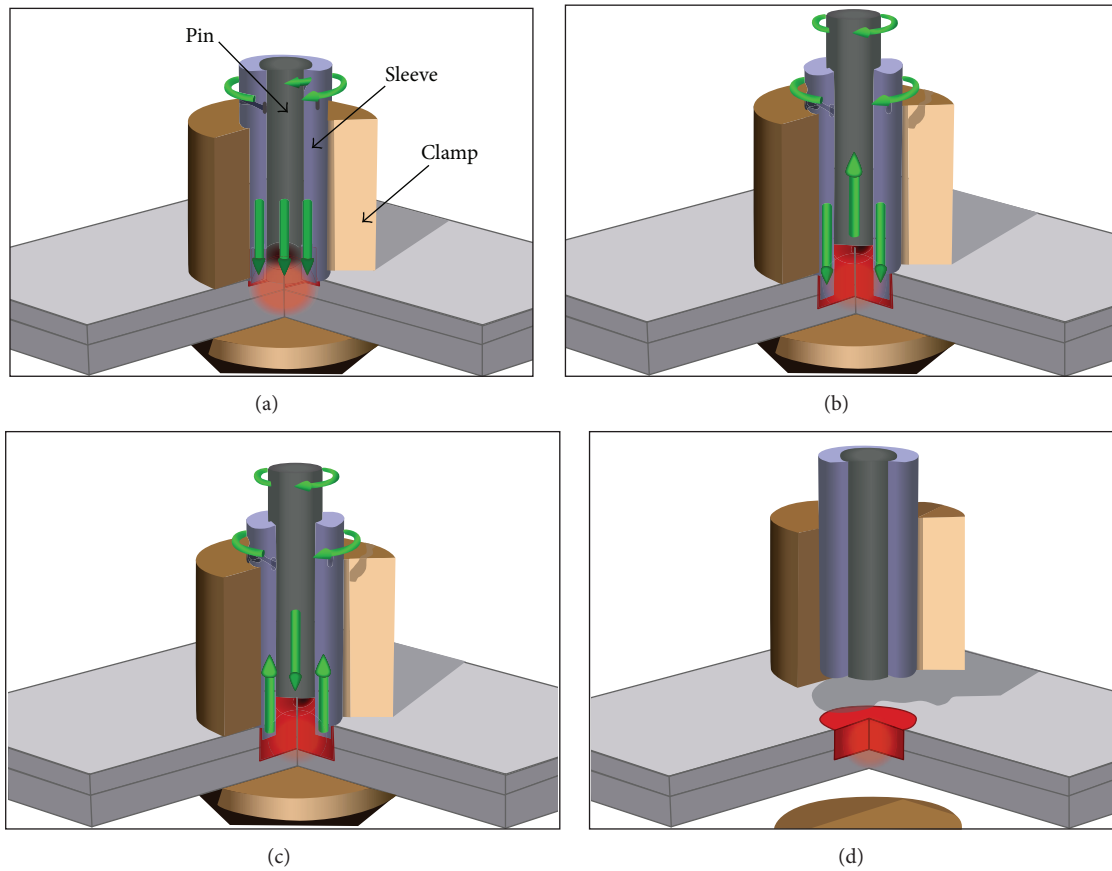


FIGURE 2: Schematic diagram of the refill FSSW process: (a) friction, (b) first extrusion, (c) second extrusion, and (d) pull-out stage [11].

heat is generated in the plunging and stirring stages, and thus the materials adjacent to the tool are heated, softened, and mixed in the stirring stage where a solid-state joint will be formed. When an acceptable bonding is obtained, the tool is retracted from the workpieces. This joint has a characteristic keyhole in the middle, which significantly decreases the mechanical properties of the joints [9].

In order to eliminate the keyhole or increase the strength of joints, several processes have been proposed, such as the refill FSSW, pinless FSSW, and swing FSSW [8].

2.1. The Refill FSSW. The refill FSSW was developed and patented by Helmholtz-Zentrum Geesthacht, Germany [10]. As shown in Figure 2, the refill FSSW process consists of four

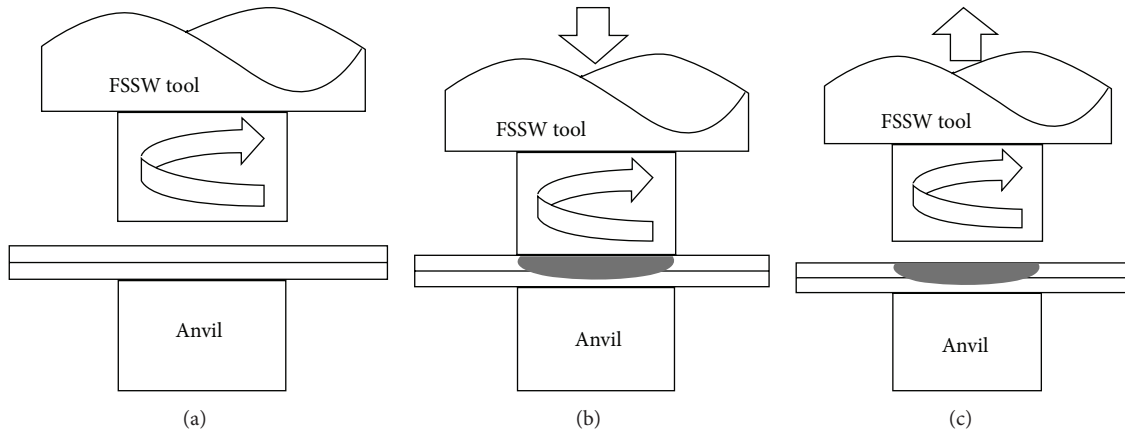


FIGURE 3: Illustration of the pinless FSSW process: (a) plunging, (b) stirring, and (c) retracting [12].

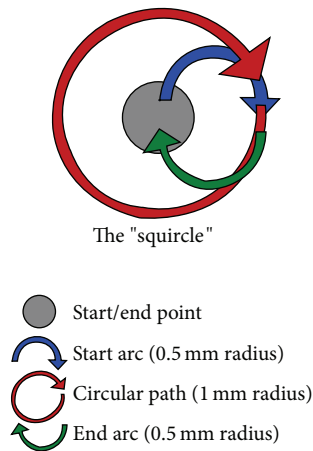


FIGURE 4: Illustration of weld path of swing FSSW [14].

phases: friction, first extrusion, second extrusion, and pull-out. In this process, the tool has three parts: pin, sleeve, and clamp. The clamp holds the plates firmly against the anvil and also constrains the material flow during the process. While the pin and sleeve begin to rotate in the same direction, they can translate independently in the axial direction. The pin and sleeve move in the opposite direction (i.e., one is plunged into the material, while the other moves upwards), creating a space where the plasticised material is accommodated. After reaching the preset plunge depth, the pin and sleeve move reversely to the surface of the plate, forcing the displaced material to completely refill the keyhole. Finally, the tool is withdrawn from the joint leaving a flat surface with minimum material loss [11].

There are fewer applications about this process, because of complicated procedures, long dwell time, and high cost. However, the keyhole could be eliminated, and the weld strength is improved.

2.2. The Pinless FSSW. The pinless FSSW was invented by Tazokai. In this process, the tool without a probe but with a scroll groove on its shoulder surface has been proposed in

2009 [1, 12]. This kind of pinless tool has many advantages, a simpler process, and a better appearance with a shallow or no keyhole retained. This process is schematically shown in Figure 3. Recently, preliminary data have shown that this approach can be used to produce high-strength welds with a short dwell time [12, 13].

2.3. The Swing FSSW. The swing FSSW was developed by TWI, UK. In this process, the tool moves along a preset path after plunging (Figure 4). This process increases the actual area of weld and the strength of joints [14], while it could not eliminate the keyhole.

2.4. The Other New FSSW Process. To obtain a weld joint without a keyhole, Sun et al. [15–17] used a new FSSW technique. This process includes two steps (Figure 5), in the first step, a specially designed backplate containing a round dent is used for conventional FSSW. After the first step, a keyhole is formed in the joint, along with a protuberance on the lower sheet due to the flow of materials into the dent. In the second step, a pinless tool and a flat backplate are employed to remove both the keyhole and the protuberance successfully. This novel process has been applied in 6061 and 5052 aluminum alloys [16].

3. Macrostructure and Microstructure of FSSW Joints

3.1. Macrostructure of FSSW Joints. Wang and Lee [18] investigated macrostructure of friction stir spot welds in aluminum 6061-T6 lap-shear specimens. In their study, keyhole was observed on the top surface of the weld. The thickness of the upper sheet material under the shoulder indentation decreased at the squeezing action of tool, consequently, resulting in an expansion of the upper sheet. However, the sheet was bent along the outer circumference of the shoulder indentation under the constraint of the neighboring material. And it was showed that squeezed out material was accumulated along the outer circumference of the shoulder

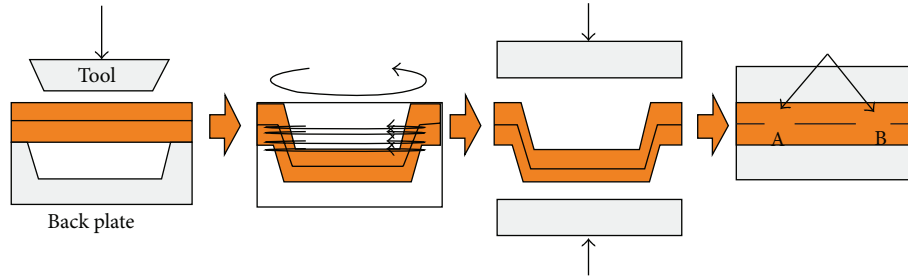


FIGURE 5: Schematic illustration of the novel FSSW [16].

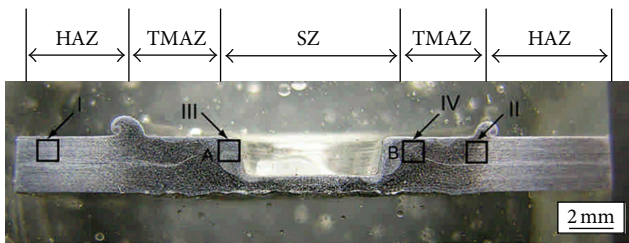


FIGURE 6: A typical micrograph of the cross-section of a friction stir spot weld [18].

indentation. Similar phenomenon was observed in the joints of friction stir spot microwelds [19].

Three distinct regions were revealed in FSSW weld joint: the stir zone (SZ), the thermomechanically affected zone (TMAZ), and heat affected zone (HAZ) [11, 18], and the gray area represented the SZ (Figure 6). For refill FSSW, Uematsu et al. [20] found that weld is classified into three zones: mixed zone (MZ), stir zone (SZ), and parent metal (PM) (Figure 7). In MZ, grains were slightly coarser than those in SZ because the material in this region was stirred more severely than SZ, and there was more heat input into MZ during the refilling process. However, for swing FSSW, Yan et al. [21] showed that weld had three regions: plastic ring region, thermomechanically affected zone, and heat affected zone and parent metal.

Cross-sectional macrostructure of the joints at different dwell time was observed by Fujimoto et al. [22]. When dwell time was 0.4 s, there was stripe pattern caused by plastic deformation in the area adjacent to the pin. At 0.8 s, it was showed that a couple of darkly etched small regions were formed. The region apparently became larger with the increase of tool dwell time. For joints of galvanized steel, white layer was found at the top sheets in all samples. Authors explained it to the phase transformation of galvanized steel or the reaction between the tool and steel sheets [23].

It is known that macroscopic appearance of FSSW joint is influenced by temperature and material plastic deformation. Moreover, welding parameters (mainly include rotation speed, dwell time, plunge depth, and plunge rate) decide the friction heat during welding. Hence, macroscopic appearance changes with the change of welding parameters. Yuan et al. [24] demonstrated that larger bonded region of AA6016-T4 weld could be gained at lower rotation speed. The reason was

that heat input increased with the increase of tool rotation speed, which in turn decreased the amount of material into the stir zone. Li et al. [25] reported that plunge depth increased with the increase of dwell time and plunge rate on the pinless friction stir spot welding of AA2024. Similarly, Baek et al. [23] showed that gap at the joint edge region decreased with increasing of tool plunge depth.

Feng et al. [26] have found that interface morphology of joining of an aluminum alloy sheet to a steel sheet changed with the change of melting temperature of the plated layer. In their study, steel sheets were plated by pure zinc (GI), zinc alloy (ZAM), Al-Si alloy (AS), and zinc alloy including Fe (GA). For ZAM and GI, bonding area was achieved in the limited area close to the periphery of the probe. There was a gap on the lapped interface under the probe (Figure 8(a)). However, the bonding area encompassed through the lapped interface under the probe for AS and GA (Figure 8(b)). The melting temperature of ZAM and GI was lower than welding temperature of the present FSSW. The plated layer would melt, so a thin liquid film of the plated layer possibly formed under the probe, which could prevent direct contact of aluminum and steel surface. The thin liquid film would solidify and form shrinkage cavity with a decrease of temperature. However, AS and GA, of which the melting temperature of plated layer was higher than welding temperature, had different phenomenon.

The common metallurgical zones on the cross-sections of FSSW weld are hooking, partial bonding, and bonding ligament (Figure 9). The hooking had a shape of an upside down V; the partial bonding was a transition region where the bonding between upper and lower sheet was not so strong, and it was a short and uneven line on the joint cross-section; the bonding ligament presented banded structure due to materials flow and the penetration force in the joint [11, 27]. Shen et al. explained banded structure to entrapment of alclad into the joint, when the lower sheet flowed upward [28]. Many persons have investigated hooking feature originating from the faying surface of the two sheets [24, 28, 29]. Yuan et al. [24] attributed it to the uncompleted break-up of aluminum oxide film. Other persons explained it to poor flowability of materials and insufficient pressure [28]. Badarinarayan et al. [29] showed that the hooking made with cylindrical pin ran gradually upward, while the hook made with triangular pin ended near SZ.

Another common defect that could be seen in weld is void. For the refill FSSW joint of 6061-T4 alloy, Shen et al. [27]

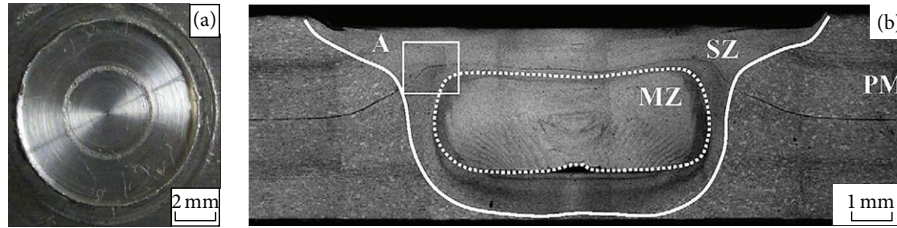


FIGURE 7: Macroscopic appearance of a FSSW joint with refilled probe hole: (a) top view of weld zone and (b) cross-section of weld zone [20].

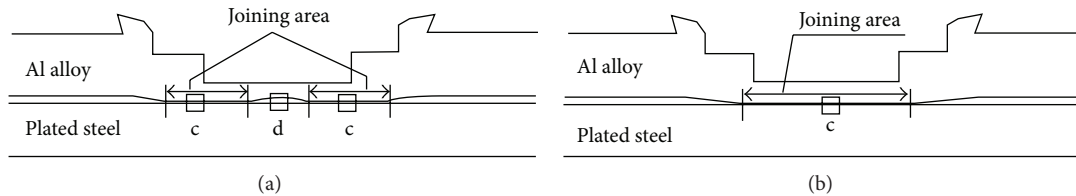


FIGURE 8: Schematic illustration of the joint interface: (a) ZAM and GI, (b) AS and GA [26].

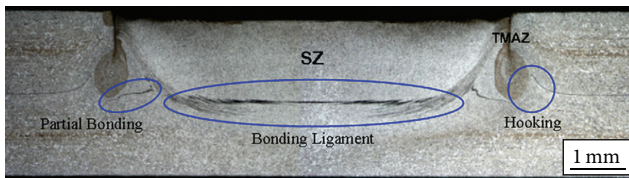


FIGURE 9: OM macrograph of a typical FSSW joint cross-section [11].

found that voids, which were owing to insufficient material flow, were formed on the hooking and the path through which the sleeve plunges into the sheet. Other persons explained it to thermal shrinkage, entrapped air, or some physical-chemical reactions [30].

3.2. Microstructure of FSSW Joints. Under friction heat and stirring, SZ presented fine equiaxed grains due to recrystallization [15, 18, 19, 31]. Sizes of grains in SZ increased with the increase of rotation speed [31]. The grains of SZ were influenced by the shape of tool. It was concluded that the triangular pin resulted in finer grain than the cylindrical pin [29, 32]. Sun et al. [15] reported that SZ had low dislocation density because of recrystallization. In the entire SZ of AZ31 and AM60 welds, Yamamoto et al. [33] observed fine equiaxed α -Mg grains which had diameters $<10 \mu\text{m}$. Shen et al. [28] investigated refill FSSW of AA7075, the hardening precipitates of SZ were dissolved and broken into particles by stirring of the tool. The grains in the boundary of the pin and sleeve were finer than those in the center because the materials in boundary were stirred more severely than other regions.

TMAZ experienced both frictional heat and deformation which resulted in highly deformed grains [31]. Recrystallization was not observed in TMAZ of AA7075 refill FSSW due to insufficient deformation strain [28]. The heating rate of FSSW was rapid, which limited the dissolution of second-phase particle in TMAZ [34]. Hence Yin et al. [34] observed

α -Mg grains for AZ31 weld. Similar phenomenon has been found in AZ91 weld [35].

The HAZ only experienced a welding thermal cycle, which caused the coarser grains [35]. For the refill FSSW joint of AA7075, HAZ had coarser strengthening precipitates than those in the BM [28].

For the new FSSW technique used by Sun et al. [15, 16], when the rotation speed was lower than 700 rpm in the first step, only one SZ and TMAZ could be found after the second step. However, when the rotation speed was higher than 700 rpm in the first step, the SZ and TMAZ that formed in first step could be overlapped by those that formed in the second step. Two kinds of SZ and TMAZ could be seen in the weld after the second step.

Yin et al. [36] reported that SZ of AZ91-AZ31 FSSW weld contained dissimilar intermingled AZ31 and AZ91 lamellae, which had similar chemical compositions with those of the AZ31 and AZ91 sheet materials prior to spot welding. Also, diffusion of aluminum at boundaries of AZ91 and AZ31 could be seen by EDS [36]. Diffusion of the solute has also been reported in weld of Al5754-Al6111 [37].

4. Property of FSSW Joints

4.1. Tensile-Shear Strength of FSSW Joints. In tensile-shear tests, shims of the same material and thickness as the sample were used when clamping the samples to induce pure shear [11]. There are usually two samples: tensile-shear and cross-tension specimens. Yuan et al. [24] indicated that the rotation speed and plunge depth were the main influence factors for tensile-shear strength. Zhang et al. [31] reported that joint strength was mainly decided by rotation speed while it was not affected significantly by dwell time. While Lin et al. [38] reported the different phenomenon, in their study, experimental results showed that the rotation speed and dwell time were dominant factors for tensile-shear strength. Strength of specimens increased as dwell time increased, which was related to growth of grains. A similar phenomenon has

been observed in polyethylene sheets [39] and 5754-O/7075-T6 joints [40]. Optimal welding parameters will improve the weld strength. The improvement in the weld strength from the initial welding parameters to the optimal welding parameters was about 47.7% for high density polypropylene [41].

For the cross-tension sample, the tensile-shear strength was affected by rotation speed, while dwell time had less influence on strength. The weld strength reached the maximum 902.1N [31]. Badarinarayan et al. [29, 32] reported that cross-tension sample had the same results with tensile-shear sample in tensile-shear tests.

Tozaki et al. [1] investigated tensile-shear sample of AA6061-T4 in pinless FSSW. It was indicated that the thickness of the upper sheet underneath the shoulder indentation (t) and the actual nugget size (d) were two significant geometrical parameters which determined the tensile-shear strength of the welds. The d size increased with increasing of tool rotation speed and dwell time. Under tensile-shear loading, the increase in the d size resulted in the increase of the tensile-shear strength because of increased effective area [42, 43]. For cross-tension sample, t dominated the weld strength. The size of t decreased with increasing of dwell time and tool rotation speed. Hence, the cross-tension strength decreased correspondingly [42]. AA6061 had similar results [43]. For alloy refill FSSW joints of AZ31 magnesium, tensile-shear strength of welds depended on the hook morphology and friction input [44].

Morphology of the tool has influence on the weld. Badarinarayan et al. [29, 32] indicated that strength of weld made with the triangular pin was twice than that of weld made with the cylindrical pin, which was attributed to the grain size as well as tensile failure mode. Choi et al. [45] compared tensile-shear strength of 5J32 Al alloy FSSW weld under three tool shapes (threaded pin tool: TPT; cylindrical tool: CT; cylindrical tool with projection: CTP). The results showed that projection of CTP retarded the vertical joint deformation; hence the tensile-shear strength rapidly increased with increasing of tool plunge depth. For TPT and CT, the tensile-shear strength of the joint did not increase because of the decrease of the upper plate thickness, which decreased with the increase of plunge depth. The maximum strength for CTP was about 4600N, which was higher than that in other two tool shapes [45]. Bilici and Yüklér [39] reported that the joint strength changed with the change of concavity angle. The maximum strength was obtained at 6° shoulder concavity angle.

For FSSW weld of dissimilar materials, the variations of weld strength depended on the material positioned on the upper side of the specimen configuration [40, 46, 47]. In the cases of dissimilar FSSW between a bulk metallic glass alloy and crystalline alloy, when the crystalline metal was positioned on the upper side, it showed a higher fracture load as compared with the opposite [46, 47].

In tensile-shear tests, there are usually three different separation modes: interfacial shear separation, nugget pull-out separation, and upper or lower sheet fracture separation. The joint with nugget fracture separation had higher strength [48]. For tensile-shear sample, cracks of interfacial shear

separation initiated preferentially at the crack tip in a weld and propagated along the bonded interface [38]. For the nugget pull-out separation, two sheets tended to get separated at the partial bonding under loading. This separation led to the formation of an annular crack surrounding the SZ, which resulted in the decrease of effective shear area of the joint. It was indicated that circumferential cracks would nucleate on just one or both sheets. On the upper sheet, the only two nucleation sites observed were the hooking tip and the welding defects, while it initiated at the interface between the partial bonding and the hooking on the lower sheet [11]. Separation modes mainly depended on the area of SZ [40]. Tozaki et al. [42] investigated the separation mode of both tensile-shear and cross-tension specimens. Results showed that final fracture modes were related to the thickness of the upper sheet at the outer circumference of the shoulder indentation (t) [42].

Prakash and Muthukumar [49] investigated refill FSSW of Al-Mg-Si aluminum, in the study, joint that had higher strength than the joint made by conversational FSSW because refilling process increased effective cross-sectional area of the nugget. Uematsu et al. [20] also reported that refilling process improved tensile strength by about 30%. Many persons demonstrated that weld made with pinless tool had higher strength than that made with conventional tool [1, 13, 50–52]. While Cox et al. [12] reported that tensile strength of welds made with a pinless tool was on average 90% of conventional FSSW, for swing FSSW, Yan et al. [21] showed that tensile strength increased by about 40% compared to conventional FSSW.

Zhang et al. [31] applied the tool to move a distance of about 5 mm along the width direction and left a complete weld about 5 mm in length, which was called walking FSSW. Compared to conversational FSSW, the strength of the joints welded by walking FSSW improved a little. In tensile-shear tests, for both tensile-shear and cross-tensile samples, nugget debonding first took place near the keyhole and then the crack propagated towards the walking side, causing the whole nugget in the walking side to pull out [31].

4.2. Fatigue Strength of FSSW Joints. The fatigue cracks were observed to propagate through the tip of hooking [53]. There are also usually two samples: lap-shear and cross-tension specimens. The fractography analysis suggested that the effective top sheet thickness, interfacial hooking, and microstructure significantly affected the fatigue behavior of the friction stir spot welds in magnesium alloys [54]. In the similar welds, fracture mode was irrelevant to load levels for lap-shear specimens, and crack took place in lower sheet under high or low load levels [55, 56]. However, the fatigue modes of FSSW in AZ31 depended on the cyclic load amplitude [53, 57]. Nugget pullout took place under high load amplitude, while crack propagated along width of samples under low load amplitude [53]. Similarly, Tran et al. [58] investigated failure modes of the 5754 and 6111 similar welds. Result showed that under quasistatic loading conditions, welds mainly failed from the nearly flat fracture surface through the nugget. Under low-cycle loading conditions,

both types of welds mainly failed through the upper sheet thickness. Under high-cycle loading conditions, both types of welds mainly failed through the upper and lower sheet thicknesses [58].

For A6061 and low carbon steel sheets dissimilar lap-shear welds, fatigue fracture modes were dependent on fatigue load level. Shear fracture through the interface occurred at high load levels, and a fatigue crack grew through the upper sheet at low load levels [55, 56]. Tran et al. [59] investigated that failure mode of the 5754-7075 welds in lap-shear specimens, under quasistatic loading conditions, crack propagated along the nugget circumference, under cyclic loading conditions, crack propagated in the width direction of the specimen, and the left part of the lower sheet was eventually separated (Figure 10). A similar phenomenon took place in AZ31B-H24 Mg alloy and 5754-O Al alloy dissimilar lap-shear welds; in the (top) Al-Mg (bottom) with an adhesive interlayer weld, nugget pull-out failure occurred at high cyclic loads. At low cyclic loads, fatigue failure occurred in the bottom Mg sheet. For (top) Mg-Al (bottom) with an adhesive interlayer weld, nugget pull-out failure modes were observed at both high and low cyclic loads [61]. The fatigue cracks between Al-steel and Mg-steel welds grew through the interface dominantly [57]. The results were similar to the results of Mg-Al in [61].

For cross-tension specimen, Lin et al. [60] investigated the failure modes in FSSW of aluminum 6061-T6 sheets. In their study, there were two different nugget pull-out failure modes (Figure 11). Under quasistatic and low-cycle loading conditions, the upper nugget was pulled out, while the lower nugget was pulled out under high-cycle loading [60]. For 5754-7075 welds in cross-tension specimens, Tran et al. [59] reported that under quasistatic loading conditions, crack propagated through the upper sheet thickness; under cyclic loading conditions, crack propagated along the interfacial surface in the downward direction toward the central hole.

Hassanifard et al. [62] introduced a new method for enhancing the life and fatigue strength of friction stir spot weld in Al alloy 7075-T6. This method had two steps, in the first step, a keyhole in the middle of joints was transferred to open hole by means of drilling; in the second step, the open hole samples were allocated for cold expansion process in order to induce compressive residual stresses. The results showed that the cold expansion could enhance the fatigue life of joints without altering their failure modes [62].

Uematsu et al. [20] reported that the fatigue strength of the refill FSSW was lower than that of the joint with probe hole at low and high applied loads. At high applied loads, the authors explained it to the difference of fracture mode between refill FSSW and conversational FSSW [20].

5. Modelling of the FSSW Process

To optimise the process parameters and develop FSSW new tools, it is important to understand the physics of this complex process that involves fatigue life, temperature gradient, and strength by numerical simulation [63]. Wang and Chen [64] developed a fatigue crack growth model based

on the Paris law and the local stress intensity factors to predict the fatigue lives of aluminum 6061-T6 lap-shear welds; the results agreed well with the experimental results. Lin et al. [60] got the similar results. Moreover, modelling conducted in AZ31 alloy lap-shear welds suggested that the size of the interfacial hook was a major influence on the fatigue life of the joint [63].

For the friction heat, Awang and Mucino [65] used Johnson-Cook material model to analyze energy generation of FSSW of 6061-T6 aluminum alloy. The results suggested that the peak temperature at the tip of the pin and frictional dissipation energy were in agreement with the experimental work done by Gerlich et al. [66]. The difference was about 5.1%. Friction heat at the interface of the tool and the work-piece generated the most energy, which was about 96.84%; rotational speed and plunge rate also had a significant effect on frictional dissipation energy [65].

In order to optimize welding parameters of FSSW and increase strength of welds, Atharifar [67] used artificial neural network to optimize welding parameters. This network was designed with three process parameters as inputs and three process variables as outputs. The outputs were selected as the weld's tensile strength, plunging load, and dwell time. Results suggested that the obtained optimums of the FSSW parameters were valid, and the welds with higher weld strength, lower plunging load, and shorter dwell time were gained by utilizing these parameters [67]. Kulekci et al. [68] compared the factorial design and neural network. Neural network was better than factorial design technique for the predicting of the tensile-shear strength in 5005 aluminum alloys. Moreover, regression analysis method was used to analyse the relation between the tensile-shear strength and FSSW welding parameters, and pin height was found to be the major factor for tensile-shear strength of FSSW joints [68]. However, Karthikeyan and Balasubramanian [69] reported that plunge rate had greater influence on tensile-shear strength. The authors also developed an empirical relationship to predict the tensile-shear strength of AA2024-T3 aluminum alloy FSSW joints and applied response surface methodology to attain maximum tensile-shear strength of welds.

Kim et al. [70] utilized two ways to develop thermomechanical simulations of AA5083-H18 and AA6022-T4. The two methods were commercial finite element method (FEM) based on Lagrangian and finite volume method (FVM) based on Eulerian formulations. The effect of pin geometry on weld strength and material flow was understood by simulation [70].

For the refill FSSW, Muci-Küchler et al. [63] presented a fully coupled thermomechanical finite element model to predict the temperature, deformation, stress, and strain distributions in the joints. The simulation results were in good agreement with experimental studies [63]. Hooking will degrade the joint properties. In order to reveal the formation mechanism of hooking during pinless FSSW, Zhang et al. [71] developed a 3D fully coupled thermomechanical FE model; the results showed that the hook formation could be mainly attributed to the difference of material flow in different weld zones.

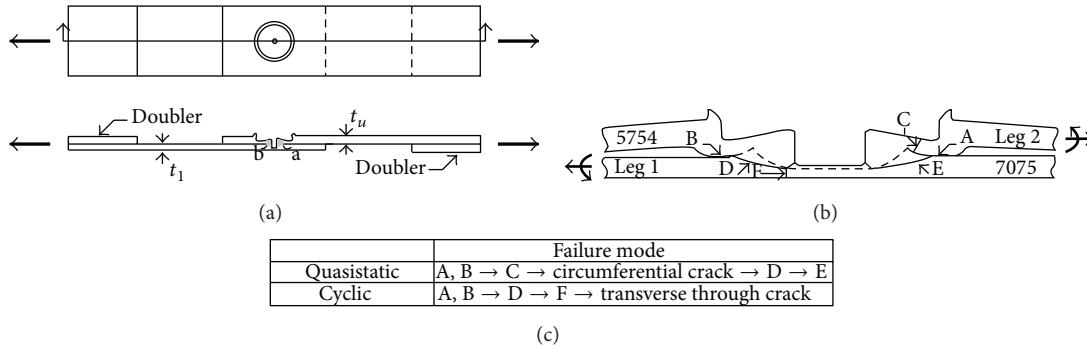


FIGURE 10: (a) Schematic plots of a spot friction weld in a lap-shear specimen under applied resultant loads (shown as the bold arrows), (b) a schematic plot of the cross-section along the symmetry plane of a 5754-7075 weld in a lap-shear specimen, and (c) failure modes of the 5754-7075 welds in lap-shear specimens under quasistatic and cyclic loading conditions [59].

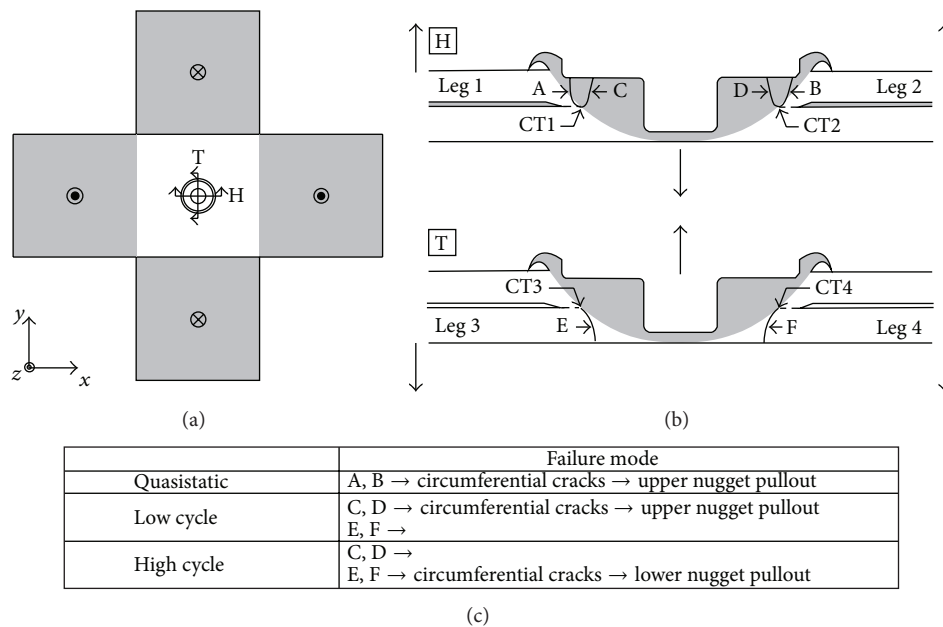


FIGURE 11: Schematics of (a) the top view of a cross-tension specimen, (b) the cross-sections along the horizontal (marked by H) and transverse (marked by T) symmetry planes of the spot friction weld, respectively, and (c) the failure modes of spot friction welds under different loading conditions [60].

6. Summary and Perspectives

At present, the FSSW process has become one of the most optimal processes in substituting the conventional resistance spot welding and riveting in joining lightweight structural metals, such as aluminum and magnesium alloys, in the automotive and aerospace industries.

FSSW could be classified into four types: conventional FSSW, refill FSSW, pinless FSSW, and swing FSSW. Normally, three distinct regions are observed in the FSSW joints: the stir zone (SZ), the thermomechanically affected zone (TMAZ), and the heat affected zone (HAZ). In tensile-shear tests, there are usually three different failure modes: interfacial shear separation, nugget pull-out separation, and upper or lower sheet fracture separation. The fatigue cracks usually propagate through the tip of hooking. However, there are still

no mature theory and abundant database for applications of FSSW. Reliability of joints has not been understood totally. To the authors' knowledge, there are still important issues that need to be revealed.

- (1) FSSW techniques without keyhole defect (refill FSSW, pinless FSSW, and other new processes) should be paid more attention.
- (2) The materials used in FSSW should be enlarged. Besides aluminum and magnesium alloys, engineering plastics and other materials also need to be introduced into the research scope.
- (3) The flexible, multipurpose, and reliable FSSW equipment should be developed for better applications in industrial production.

Conflict of Interests

The authors declare that they do not have a direct relation with any commercial identities that might lead to a conflict of interests for any of them.

Acknowledgments

The authors would like to appreciate financial supports from the Fok Ying-Tong Education Foundation for Young Teachers in the Higher Education Institutions of China (131052), the Fundamental Research Fund of NPU (JC201233), and the 111 Project (B08040).

References

- [1] Y. Tozaki, Y. Uematsu, and K. Tokaji, "A newly developed tool without probe for friction stir spot welding and its performance," *Journal of Materials Processing Technology*, vol. 210, no. 6-7, pp. 844–851, 2010.
- [2] N. Nguyen, D. Y. Kim, and H. Y. Kim, "Assessment of the failure load for an AA6061-T6 friction stir spot welding joint," *Proceedings of the Institution of Mechanical Engineers, Part B: Journal of Engineering Manufacture*, vol. 225, no. 10, pp. 1746–1756, 2011.
- [3] W. M. Thomas, E. D. Nicholas, and J. C. Needham, "Friction stir welding," International patent PCT/GB92102203 and Great Britain patent 9125978.8, 1991.
- [4] R. S. Mishra and Z. Y. Ma, "Friction stir welding and processing," *Materials Science and Engineering*, vol. 50, no. 1-2, pp. 1–78, 2005.
- [5] C. J. Dawes, "An introduction to friction stir welding and its development," *Welding and Metal Fabrication*, vol. 63, no. 1, pp. 12–16, 1995.
- [6] C. G. Rhodes, M. W. Mahoney, W. H. Bingel, R. A. Spurling, and C. C. Bampton, "Effects of friction stir welding on microstructure of 7075 aluminum," *Scripta Materialia*, vol. 36, no. 1, pp. 69–75, 1997.
- [7] C. J. Dawes and W. M. Thomas, "Friction stir process welds aluminium alloys: the process produces low-distortion, high-quality, low-cost welds on aluminium," *Welding Journal*, vol. 75, no. 3, pp. 41–45, 1996.
- [8] R. Sakano, K. Murakami, K. Yamashita et al., "Development of spot FSW robot system for automobile body members," in *Proceedings of the 3rd International Symposium of Friction Stir Welding*, Kobe, Japan, 2004.
- [9] N.-T. Nguyen, D.-Y. Kim, and H. Y. Kim, "Assessment of the failure load for an AA6061-T6 friction stir spot welding joint," *Proceedings of the Institution of Mechanical Engineers B: Journal of Engineering Manufacture*, vol. 225, no. 10, pp. 1746–1756, 2011.
- [10] C. Schilling and J. Dos Santos, "Method and device for linking at least two adjoining work pieces by friction welding," US Patent 6722556B2, 2004.
- [11] T. Rosendo, B. Parra, M. A. D. Tier et al., "Mechanical and microstructural investigation of friction spot welded AA6181-T4 aluminium alloy," *Materials and Design*, vol. 32, no. 3, pp. 1094–1100, 2011.
- [12] C. D. Cox, B. T. Gibson, A. M. Strauss, and G. E. Cook, "Effect of pin length and rotation rate on the tensile strength of a friction stir spot-welded Al alloy: A contribution to automated production," *Materials and Manufacturing Processes*, vol. 27, no. 4, pp. 472–478, 2012.
- [13] P. B. Prangnell and D. Bakavos, "Novel approaches to friction spot welding thin aluminium automotive sheet," *Materials Science Forum*, vol. 638–642, pp. 1237–1242, 2010.
- [14] Y. Fang, *The Research on the Processes and Properties of Pinless Friction Stir Spot Welding*, Jiangsu University of Science and Technology, Jiangsu, China, 2009.
- [15] Y. F. Sun, H. Fujii, N. Takaki, and Y. Okitsu, "Microstructure and mechanical properties of mild steel joints prepared by a flat friction stir spot welding technique," *Materials & Design*, vol. 37, pp. 384–392, 2012.
- [16] Y. F. Sun, H. Fujii, N. Takaki, and Y. Okitsu, "Novel spot friction stir welding of 6061 and 5052 Al alloys," *Science and Technology of Welding and Joining*, vol. 16, no. 7, pp. 605–612, 2011.
- [17] Y. F. Sun, H. Fujii, N. Takaki, and Y. Okitsu, "Microstructure and mechanical properties of dissimilar Al alloy/steel joints prepared by a flat spot friction stir welding technique," *Materials and Design*, vol. 47, pp. 350–357, 2013.
- [18] D.-A. Wang and S.-C. Lee, "Microstructures and failure mechanisms of friction stir spot welds of aluminum 6061-T6 sheets," *Journal of Materials Processing Technology*, vol. 186, no. 1–3, pp. 291–297, 2007.
- [19] D. Wang, C. Chao, P. Lin, and J. Uan, "Mechanical characterization of friction stir spot microwelds," *Journal of Materials Processing Technology*, vol. 210, no. 14, pp. 1942–1948, 2010.
- [20] Y. Uematsu, K. Tokaji, Y. Tozaki, T. Kurita, and S. Murata, "Effect of re-filling probe hole on tensile failure and fatigue behaviour of friction stir spot welded joints in Al-Mg-Si alloy," *International Journal of Fatigue*, vol. 30, no. 10-11, pp. 1956–1966, 2008.
- [21] K. Yan, Z. Y. Li, and J. Fu, "The metal flow behavior of swing friction stir spot welding joint," *Journal of Jiangsu University of Science and Technology*, vol. 22, no. 2, pp. 35–38, 2008.
- [22] M. Fujimoto, M. Inuzuka, S. Koga, and Y. Seta, "Development of friction spot joining," *Welding in the World*, vol. 49, no. 3-4, pp. 18–21, 2005.
- [23] S. Baek, D. Choi, C. Lee et al., "Microstructure and mechanical properties of friction stir spot welded galvanized steel," *Materials Transactions*, vol. 51, no. 5, pp. 1044–1050, 2010.
- [24] W. Yuan, R. S. Mishra, S. Webb et al., "Effect of tool design and process parameters on properties of Al alloy 6016 friction stir spot welds," *Journal of Materials Processing Technology*, vol. 211, no. 6, pp. 972–977, 2011.
- [25] W. Y. Li, J. F. Li, D. L. Gao et al., "Pinless friction stir spot welding of 2024 aluminum alloy: effect of welding parameters," in *Proceedings of the 7th Asia Pacific IIW International Congress*, pp. 72–77, 2013.
- [26] K. Feng, M. Watanabe, and S. Kumai, "Microstructure and joint strength of friction stir spot welded 6022 aluminum alloy sheets and plated steel sheets," *Materials Transactions*, vol. 52, no. 7, pp. 1418–1425, 2011.
- [27] Z. Shen, X. Yang, S. Yang et al., "Microstructure and mechanical properties of friction spot welded 6061-T4 aluminum alloy," *Materials and Design*, vol. 54, pp. 766–778, 2014.
- [28] Z. Shen, X. Yang, Z. Zhang, L. Cui, and T. Li, "Microstructure and failure mechanisms of refill friction stir spot welded 7075-T6 aluminum alloy joints," *Materials and Design*, vol. 44, pp. 476–486, 2013.
- [29] H. Badarinarayan, Q. Yang, and S. Zhu, "Effect of tool geometry on static strength of friction stir spot-welded aluminum alloy,"

- International Journal of Machine Tools and Manufacture*, vol. 49, no. 2, pp. 142–148, 2009.
- [30] P. H. F. Oliveira, S. T. Amancio-Filho, J. F. Dos Santos, and E. Hage Jr., “Preliminary study on the feasibility of friction spot welding in PMMA,” *Materials Letters*, vol. 64, no. 19, pp. 2098–2101, 2010.
- [31] Z. H. Zhang, X. Q. Yang, J. L. Zhang, G. Zhou, X. Xu, and B. Zou, “Effect of welding parameters on microstructure and mechanical properties of friction stir spot welded 5052 aluminum alloy,” *Materials & Design*, vol. 32, no. 8-9, pp. 4461–4470, 2011.
- [32] H. Badarinarayan, Y. Shi, X. Li, and K. Okamoto, “Effect of tool geometry on hook formation and static strength of friction stir spot welded aluminum 5754-O sheets,” *International Journal of Machine Tools and Manufacture*, vol. 49, no. 11, pp. 814–823, 2009.
- [33] M. Yamamoto, A. Gerlich, T. H. North, and K. Shinozaki, “Cracking in the stir zones of Mg-alloy friction stir spot welds,” *Journal of Materials Science*, vol. 42, no. 18, pp. 7657–7666, 2007.
- [34] Y. H. Yin, A. Ikuta, and T. H. North, “Microstructural features and mechanical properties of AM60 and AZ31 friction stir spot welds,” *Materials and Design*, vol. 31, no. 10, pp. 4764–4776, 2010.
- [35] M. Yamamoto, A. Gerlich, T. H. North, and K. Shinozaki, “Cracking in dissimilar Mg alloy friction stir spot welds,” *Science and Technology of Welding and Joining*, vol. 13, no. 7, pp. 583–592, 2008.
- [36] Y. H. Yin, N. Sun, T. H. North, and S. S. Hu, “Microstructures and mechanical properties in dissimilar AZ91/AZ31 spot welds,” *Materials Characterization*, vol. 61, no. 10, pp. 1018–1028, 2010.
- [37] P. Su, A. Gerlich, T. H. North, and G. J. Bendzsak, “Intermixing in dissimilar friction stir spot welds,” *Metallurgical and Materials Transactions A*, vol. 38, no. 3, pp. 584–595, 2007.
- [38] Y. C. Liu, J. J. Lin, B. Y. Lin, C. M. Lin, and H. L. Tsai, “Effects of process parameters on strength of Mg alloy AZ61 friction stir spot welds,” *Materials and Design*, vol. 35, pp. 350–357, 2012.
- [39] M. K. Bilici and A. I. Yüklér, “Influence of tool geometry and process parameters on macrostructure and static strength in friction stir spot welded polyethylene sheets,” *Materials and Design*, vol. 33, no. 1, pp. 145–152, 2012.
- [40] V. X. Tran, J. Pan, and T. Pan, “Effects of processing time on strengths and failure modes of dissimilar spot friction welds between aluminum 5754-O and 7075-T6 sheets,” *Journal of Materials Processing Technology*, vol. 209, no. 8, pp. 3724–3739, 2009.
- [41] M. K. Bilici, “Application of Taguchi approach to optimize friction stir spot welding parameters of polypropylene,” *Materials and Design*, vol. 35, pp. 113–119, 2012.
- [42] Y. Tozaki, Y. Uematsu, and K. Tokaji, “Effect of processing parameters on static strength of dissimilar friction stir spot welds between different aluminium alloys,” *Fatigue and Fracture of Engineering Materials and Structures*, vol. 30, no. 2, pp. 143–148, 2007.
- [43] Y. Tozaki, Y. Uematsu, and K. Tokaji, “Effect of tool geometry on microstructure and static strength in friction stir spot welded aluminium alloys,” *International Journal of Machine Tools and Manufacture*, vol. 47, no. 15, pp. 2230–2236, 2007.
- [44] L. C. Campanelli, U. F. H. Suhuddin, A. Í. S. Antonialli, J. F. dos Santos, N. G. de Alcântara, and C. Bolfarini, “Metallurgy and mechanical performance of AZ31 magnesium alloy friction spot welds,” *Journal of Materials Processing Technology*, vol. 213, no. 4, pp. 515–521, 2013.
- [45] D. H. Choi, B. W. Ahn, C. Y. Lee, Y. M. Yeon, and K. B. Song, “Effect of pin shapes on joint characteristics of friction stir spot welded AA5J32 sheet,” *Materials Transactions*, vol. 51, no. 5, pp. 1028–1032, 2010.
- [46] H. Shin and Y. Jung, “Characteristics of dissimilar friction stir spot welding of bulk metallic glass to lightweight crystalline metals,” *Intermetallics*, vol. 18, no. 10, pp. 2000–2004, 2010.
- [47] H. Shin and Y. Jung, “Characteristics of friction stir spot welding of Zr-based bulk metallic glass sheets,” *Journal of Alloys and Compounds*, vol. 504, no. 1, pp. S279–S282, 2010.
- [48] M. K. Bilici and A. I. Yüklér, “Effects of welding parameters on friction stir spot welding of high density polyethylene sheets,” *Materials and Design*, vol. 33, no. 1, pp. 545–550, 2012.
- [49] S. J. Prakash and S. Muthukumaran, “Refilling probe hole of friction spot joints by friction forming,” *Materials and Manufacturing Processes*, vol. 26, no. 12, pp. 1539–1545, 2011.
- [50] M. Simoncini and A. Forcellese, “Effect of the welding parameters and tool configuration on micro- and macro-mechanical properties of similar and dissimilar FSWed joints in AA5754 and AZ31 thin sheets,” *Materials & Design*, vol. 41, pp. 50–60, 2012.
- [51] A. Forcellese, F. Gabrielli, and M. Simoncini, “Mechanical properties and microstructure of joints in AZ31 thin sheets obtained by friction stir welding using “pin” and “pinless” tool configurations,” *Materials and Design*, vol. 34, pp. 219–229, 2012.
- [52] D. Bakavos and P. B. Prangnell, “Effect of reduced or zero pin length and anvil insulation on friction stir spot welding thin gauge 6111 automotive sheet,” *Science and Technology of Welding and Joining*, vol. 14, no. 5, pp. 443–456, 2009.
- [53] J. B. Jordon, M. F. Horstemeyer, S. R. Daniewicz, H. Badarinarayan, and J. Grantham, “Fatigue characterization and modeling of friction stir spot welds in magnesium AZ31 alloy,” *Journal of Engineering Materials and Technology, Transactions of the ASME*, vol. 132, no. 4, Article ID 041008, 2010.
- [54] H. M. Rao, J. B. Jordon, M. E. Barkey, Y. B. Guo, X. Su, and H. Badarinarayan, “Influence of structural integrity on fatigue behavior of friction stir spot welded AZ31 Mg alloy,” *Materials Science and Engineering A*, vol. 564, pp. 369–380, 2013.
- [55] Y. Uematsu, K. Tokaji, and Y. Tozaki, “Fatigue behaviour of dissimilar friction stir spot weld between A6061 and SPCC welded by a scrolled groove shoulder tool,” *Procedia Engineering*, vol. 2, no. 1, pp. 193–201, 2010.
- [56] Y. Uematsu, K. Tokaji, Y. Tozaki, Y. Nakashima, and T. Shimizu, “Fatigue behaviour of dissimilar friction stir spot welds between A6061-T6 and low carbon steel sheets welded by a scroll grooved tool without probe,” *Fatigue and Fracture of Engineering Materials and Structures*, vol. 34, no. 8, pp. 581–591, 2011.
- [57] Y. Uematsu, T. Kakiuchi, Y. Tozaki, and H. Kojin, “Comparative study of fatigue behaviour in dissimilar Al alloy/steel and Mg alloy/steel friction stir spot welds fabricated by scroll grooved tool without probe,” *Science and Technology of Welding and Joining*, vol. 17, no. 5, pp. 348–356, 2012.
- [58] V.-X. Tran, J. Pan, and T. Pan, “Fatigue behavior of aluminum 5754-O and 6111-T4 spot friction welds in lap-shear specimens,” *International Journal of Fatigue*, vol. 30, no. 12, pp. 2175–2190, 2008.
- [59] V. X. Tran, J. Pan, and T. Pan, “Fatigue behavior of spot friction welds in lap-shear and cross-tension specimens of dissimilar aluminum sheets,” *International Journal of Fatigue*, vol. 32, no. 7, pp. 1022–1041, 2010.
- [60] P. C. Lin, Z. M. Su, R. Y. He, and Z.-L. Lin, “Failure modes and fatigue life estimations of spot friction welds in cross-tension

- specimens of aluminum 6061-T6 sheets,” *International Journal of Fatigue*, vol. 38, pp. 25–35, 2012.
- [61] S. H. Chowdhury, D. L. Chen, S. D. Bhole, X. Cao, and P. Wanjara, “Lap shear strength and fatigue behavior of friction stir spot welded dissimilar magnesium-to-aluminum joints with adhesive,” *Materials Science and Engineering A*, vol. 562, pp. 53–60, 2013.
- [62] S. Hassanifard, M. Mohammadpour, and H. A. Rashid, “A novel method for improving fatigue life of friction stir spot welded joints using localized plasticity,” *Materials and Design*, vol. 53, pp. 962–971, 2014.
- [63] K. H. Muci-Küchler, S. Kalagara, and W. J. Arbegast, “Simulation of a refill friction stir spot welding process using a fully coupled thermo-mechanical FEM model,” *Journal of Manufacturing Science and Engineering, Transactions of the ASME*, vol. 132, no. 1, Article ID 0145031, 2010.
- [64] D. A. Wang and C. H. Chen, “Fatigue lives of friction stir spot welds in aluminum 6061-T6 sheets,” *Journal of Materials Processing Technology*, vol. 209, no. 1, pp. 367–375, 2009.
- [65] M. Awang and V. H. Mucino, “Energy generation during friction stir spot welding (FSSW) of Al 6061-T6 plates,” *Materials and Manufacturing Processes*, vol. 25, no. 1–3, pp. 167–174, 2010.
- [66] A. Gerlich, P. Su, and T. H. North, “Peak temperatures and microstructures in aluminium and magnesium alloy friction stir spot welds,” *Science and Technology of Welding and Joining*, vol. 10, no. 6, pp. 647–652, 2005.
- [67] H. Atharifar, “Optimum parameters design for friction stir spot welding using a genetically optimized neural network system,” *Proceedings of the Institution of Mechanical Engineers B: Journal of Engineering Manufacture*, vol. 224, no. 3, pp. 403–418, 2010.
- [68] M. K. Kulekci, U. Esme, O. Er, and Y. Kazancoglu, “Modeling and prediction of weld shear strength in friction stir spot welding using design of experiments and neural network,” *Materials Science and Engineering Technology*, vol. 42, no. 11, pp. 990–995, 2011.
- [69] R. Karthikeyan and V. Balasubramanian, “Predictions of the optimized friction stir spot welding process parameters for joining AA2024 aluminum alloy using RSM,” *The International Journal of Advanced Manufacturing Technology*, vol. 51, no. 1–4, pp. 173–183, 2010.
- [70] D. Kim, H. Badarinarayan, I. Ryu et al., “Numerical simulation of friction stir spot welding process for aluminum alloys,” *Metals and Materials International*, vol. 16, no. 2, pp. 323–332, 2010.
- [71] Z. H. Zhang, W. Y. Li, J. F. Li et al., “Numerical analysis on formation mechanism of hook during pinless friction stir spot welding,” in *Proceedings of the 7th Asia Pacific IIW International Congress*, Singapore, 2013.

Research Article

Processing Parameters Influence on Wear Resistance Behaviour of Friction Stir Processed Al-TiC Composites

E. T. Akinlabi,¹ R. M. Mahamood,^{1,2} S. A. Akinlabi,³ and E. Ogunmuyiwa¹

¹ Department of Mechanical Engineering Science, University of Johannesburg, Auckland Park Kingsway Campus, Johannesburg 2006, South Africa

² Department of Mechanical Engineering, University of Ilorin, Ilorin, Nigeria

³ School of Mechanical, Industrial and Aeronautical Engineering, University of the Witwatersrand, Johannesburg 2050, South Africa

Correspondence should be addressed to E. T. Akinlabi; etakinlabi@uj.ac.za

Received 23 December 2013; Revised 20 March 2014; Accepted 24 March 2014; Published 15 June 2014

Academic Editor: Achilles Vairis

Copyright © 2014 E. T. Akinlabi et al. This is an open access article distributed under the Creative Commons Attribution License, which permits unrestricted use, distribution, and reproduction in any medium, provided the original work is properly cited.

Friction stir processing (FSP) being a novel process is employed for the improvement of the mechanical properties of a material and the production of surface layer composites. The vital role of the integrity of surface characteristics in the mechanical properties of materials has made the research studies into surface modification important in order to improve the performance in practical applications. This study investigates the effect of processing parameters on the wear resistance behavior of friction stir processed Al-TiC composites. This was achieved through microstructural characterization by using both the optical and scanning electron microscope (SEM), microhardness profiling, and tribological characterization by means of the wear. The microhardness profiling of the processed samples revealed an increased hardness value, which was a function of the TiC particles incorporated when compared to the parent material. The wear resistance property was also found to increase as a result of the TiC powder addition. The right combination of processing parameters was found to improve the wear resistance property of the composites produced.

1. Introduction

Friction stir welding (FSW) is a novel solid-state joining technique which was invented and patented by The Welding Institute in 1991. The technique was designed and initially utilized for butt and lap welding of ferrous and nonferrous metals and plastics [1]. However, over the last two decades, the technique has been extensively modified and improved with a significant growth at both technology implementation and scientific exploration leading to commercialization. This has consequently led to the scope of its application being broadened [2] and has evolved to create several new processes, among which is the friction stir processing. The schematic of the FSW process is shown in Figure 1.

The process involves clamping the workpieces together on the machine bed along the butting faces of the joint. A nonconsumable rotating tool, with a specially designed pin and shoulder, is plunged between the abutting faces of the joint and traversed along the joint line.

The friction between the tool and the workpiece generates localized heating in the vicinity of the immersed rotating pin, causing the plastic deformation of the material. In addition, the generated heat softens the material and creates a plasticized region around the plunged rotating pin, while the shoulder of the tool prevents the egress of the plasticized material from the weld. The tool meanwhile moves linearly along the joint line, causing the plasticized material to flow from the front to the back of the pin, at which point, it coalesces and forms a solid-state welded joint [3].

Friction stir welding enjoys numerous advantages over the previous conventional welding methods. These advantages are classified into two distinct categories, which are the metallurgical benefits and the environmental benefits. The metallurgical benefits include low distortion, greater weld strength, good dimensional stability and repeatability, no loss of alloying elements, excellent metallurgical properties in the joint area, good corrosion resistance, fine microstructure, and absence of cracks [4]. Some of the environmental

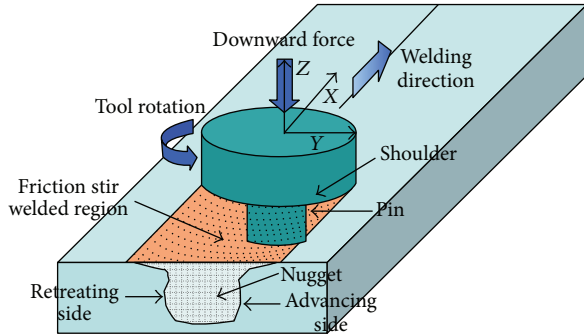


FIGURE 1: Schematic of friction stir welding process [1].

benefits include lower energy consumption compared to the conventional welding, surface cleaning, degreasing solvents, and negating harmful welding fumes and gasses and waste material [5].

FSW has been touted as being the most significant development in metal joining in a decade [1], and FSP is expected to be the evolutionary successor. It employs the same basic processing technique and tooling design as found in FSW. However, it differs in that FSW deals with joining two materials either similar or dissimilar, whereas FSP is employed to strengthen (not necessarily join) some areas of a material. Furthermore, FSP being a continuous process also employs a rotating tool comprising a pin and shoulder plunged into the area of interest.

Heat is generated by the frictional forces between the rotating tool and the substrate, with additional adiabatic heating generated from the metal deformation. The tool then traverses relatively over the substrate, causing it to coalesce. The processed zone cools without solidification (as there is no liquid), creating a defect-free recrystallized and fine grain microstructure. The advantages of friction stir processing are mainly metallurgical in nature and, as such, it is a process that can change and modify the local properties of a workpiece, without influencing the properties in the remaining part of the workpiece. Casting defects can be locally eliminated, and the microstructure thereby refined, thus improving the strength and ductility, enhancing formability, and substantially increasing corrosion resistance and fatigue life of the processed material [6, 7]. FSP is also able to produce fine-grained microstructures through the thickness to impart super plasticity.

In FSP, there are a number of parameters, which affect the overall process. Varying these parameters can have a significant effect on the mechanical properties such as the microhardness and strength and fatigue life of the final product [1, 2]. Aluminium and its alloys enjoy widespread applications due to many positive characteristics, among which are the favorable strength to weight ratio, corrosion resistance, and appearance. The integrity of the joint is dependent on an array of factors such as the geometry, material composition, type of joint, number of joints, and the environmental service conditions [8]. On the other hand, friction stir welding has successfully been utilized to weld all wrought aluminium alloys, across the 2xxx, 5xxx, 6xxx, and 7xxx series of alloys, some of which are bordering on being classed as virtually

nonweldable by fusion welding techniques. The friction stir welding process is also able to weld dissimilar aluminium alloys, whereas fusion welding may result in the alloying elements from the different alloys interacting to form deleterious intermetallics through precipitation during solidification from the molten weld pool [9].

FSP, being cutting edge and new, is an emerging technology, which has generated an enormous amount of interest in the industry, specifically in the aerospace, marine, and the automotive sector, and so forth. Mega companies which are known to be researching and utilizing FSP technology include Boeing, Phantom Works, Bombardier, Cummins, EADS Airbus, General Motors Research, Gulfstream, Hawker Beechcraft, JFE Steel, Kaiser Aluminium, Kawasaki, Lockheed Martin Corp, NASA Johnson Space Centre, NASA Langley Research Centre, Space X, and the Swedish Nuclear Fuel and Waste Management Company [1]. This growing list of companies confirms the claim of the relevance of this new technology to various applications. In addition, it predicts the imminent surge in the popularity and prevalence of FSP.

Friction stir processing is most commonly employed on aluminum and its alloys [10, 11]; friction stir processing is often used to create aluminium matrix composites (AMC) which uses aluminium as the parent material. However, most of the research work on FSP of aluminium and its alloys reported in the literature ranged between the 1xxx, 2xxx, 5xxx, 6xxx, and 7xxx series of alloys; these are the same series which have proven successful in the FSW experiments. Typical FSP of aluminium and its alloys found in the literature include AA1050 [6, 12, 13], AA2024 [14–16], AA2095 [17], AA5083 [18–20], AA5086 [21], AA6061 [22, 23], and AA7075 [24]. It is shown that FSP technology is very effective in microstructure modification of reinforced metal matrix composite materials [11]. FSW and FSP have many advantages such as elimination of the defects such as cracks and porosity often associated with fusion welding processes and reduced distortion. In addition, it can be carried out in various positions and can join conventionally nonfusion weldable alloys and improve mechanical properties of weldable alloys. FSP has also been used to refine the grains of casting alloys [25] and to homogenize the microstructure of reinforced metal matrix composite materials [26].

Many of the processing techniques have been developed for the manufacture of particles or short fibre reinforced composites. Metal-matrix composites particularly aluminium reinforced with ceramic phases make them promising structural materials for the aerospace and automobile industries [6]. The major draw backs of such composites processed through these routes are inhomogeneous distribution (known as clustering) and improper wetting of particles which lead to poor mechanical properties [27]. An alternative approach to overcome this limitation is to produce the reinforcement in situ during processing. In the in situ process, there is no need to add the reinforcements separately; instead, the desirable reinforcement(s) and the interfaces are formed during processing itself [28–30]. Metal matrix composite (MMC) technology is one such method which can effectively increase the strength of the Al matrix with ceramic reinforcements like SiC, Al₂O₃, AlN, B₄C, and TiC [31]. The

metal matrix composite almost always offers an improvement in the microstructure and hardness compared to the base metal. It should also be noted, especially in reference to this particular study, those FSP parameters such as the tool rotation and traverse speeds can have a significant effect on the material properties of the AMC [32]. This is due to the fact that these parameters have a strong influence on the grain size and dissolution of precipitates in heat treatable alloys, and these microstructural features are responsible for the material properties of the processed Al alloys.

There have been numerous studies on the application of the FSP process to fabricate an MMC directly on the surface of a plate in situ by processing a groove or channel on the plate which is filled with reinforcing particles [33]. However, it remains a challenge to prevent the particles from being ejected out of the groove during the FSP, and the distribution of particles is typically nonuniform unless multiple FSP passes are applied to homogenize the microstructure [34]. During FSP of composites, the parameters further influence the distribution, morphology, and break-up of the reinforcing particles [35, 36]. The resultant composites generally exhibit better microstructure and properties because of improved wettability of particles, a clean particle-matrix interface, and strong bonds between the reinforcement and the metallic matrix [37].

Thangarasu et al. [6] investigated the microstructure and microhardness of TiC particulate ($\sim 2 \mu\text{m}$) reinforced aluminium matrix composite (AMC) using FSP. It was established that the fabricated AA1050/TiC composite layer was well bonded to the aluminium substrate. Furthermore, the TiC particles were distributed homogeneously in the FSP zone and the hardness of the FSW zone increased by 45% higher than that of the matrix alloy; however, this was a preliminary study as only very few processing parameters were considered. Similar investigation of Bauri et al. [8] concluded that FSP could be used effectively to homogenise the particle distribution in Al-TiC in situ composites. A single pass of FSP was enough to break the particle segregation from the grain boundaries and improve the distribution. Two passes of FSP resulted in complete homogenization and elimination of casting defects. The grain size was also refined substantially after each FSP pass and finer after the second pass. Consequently, the mechanical properties improved significantly after the FSP due to the refinement in the microstructure [10]. Raafat et al. [38] concluded that the microstructure of the A390/ Al_2O_3 surface composites depends significantly on both the tool rotational and traverse speeds. Increasing the tool rotational and/or reducing the traverse speeds improves the distribution of the ceramic particulates inside the A390 matrix [39].

Aluminium matrix composites (AMCs) reinforced with ceramic phases exhibit higher strength and stiffness, improved tribological characteristics, and increased resistance to creep and fatigue. However, if the particulate is prepared by incorporating ex situ ceramic nanoparticles composites with large ceramic particles, they are prone to cracking during mechanical loading, leading to premature failure and low ductility of the composites. The mechanical properties of metal matrix composites (MMCs) can be further enhanced

by decreasing the sizes of the ceramic particulates and/or matrix grains from the SiC or TiC nanoparticles [8].

The tribological properties such as wear and corrosion have been the subject of much research in the last years and the overwhelming majority of researchers suggest that corrosion resistance is better in the MMCs than the unreinforced parent material [19, 24, 40–42]. On the other hand, it is important to know that the wear resistance is usually better for the MMC than that of the base metal for all process parameters. This is due to the fact that the composite surface layer provides wear resistance and is harder than the base material. However, as this layer wears out, the wear resistance decreases dramatically and the erosive wear volume rate spikes. The processing speed is directly proportional to the wear rate of the surface layer. Hence, the best wear resistance is achieved at the slower end of the rotation and traverse speed combinations [43]. Jerome et al. [44] also conducted a preliminary study on the influence of the microstructure and experimental parameters on the mechanical and wear properties of Al-TiC surface composites; they found that the microhardness increases as the rotational speed increases which subsequently improved the wear resistance.

It is therefore believed that, with new technologies, the utilization, optimization, and expansion of FSP are limited by the lack of established process windows leading to conclusive scientific research. Detailed characterization and statistical analysis of the wear behavior of FSP of Al-TiC which can be employed to predict process windows has not been published. This paper will therefore further research by investigating the tribological properties of Al-TiC material samples produced at a range of process parameter combinations, with the aim of contributing to the global knowledge and bringing the subject of FSP a step closer to global utilization. It will also significantly broaden the aforementioned research studies in this field of study by determining the optimum parameter combination.

2. Materials and Methods

The FSP was employed for the development of the surface composite of aluminium alloy (AA 1050) reinforced with TiC powder of particle size range below $60 \mu\text{m}$. The test samples are rectangular elements of dimension $200 \times 160 \times 3 \text{ mm}^3$. A V-groove of about 1.5 mm was engraved along the length of the sheet. In this application, the area of interest is the V-groove, which has been machined into the workpiece and filled with the TiC powder.

The V-groove was machined into an area of the base plate, with the aim of strengthening the material. The powder is compressed into the groove using a pinless tool across the surface of the material. Some of the common powders often used in the literature include titanium carbide (TiC) and silicon carbide (SiC). Once the powder is compressed, a second tool, comprising a pin and shoulder, was plunged into the workpiece. The schematic of the V-groove and compaction process is shown in Figure 2.

The selected substrate metal is AA1050; the chemical composition of the alloy is presented in Table 1.

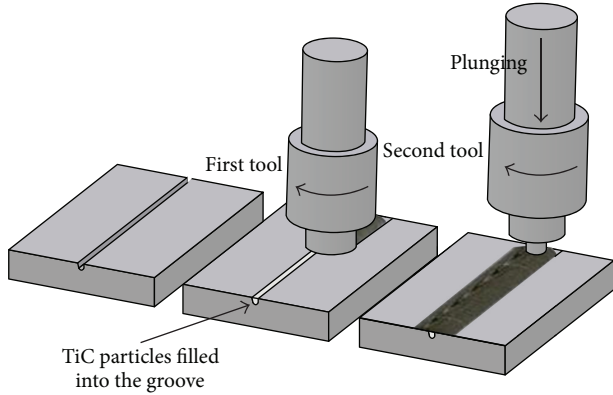


FIGURE 2: (a) A V-groove is machined into the base metal; (b) the substrate power is compressed using a pinless tool and (c) the composite is produced via FSP [6].

TABLE 1: Chemical composition of AA1050.

	Al	Si	Fe	Cu	Mn	Mg	Zn	V
AA1050	99.5	0.25	0.4	0.05	0.05	0.05	0.05	0.05

The tools used are presented in Figure 3 and the dimensions of the tool profile are shown in Figure 4. The friction stir processing was conducted on an Intelligent Stir Welding for Industry and Research (I-STIR) Process Development System (PDS) at the Nelson Mandela Metropolitan University, Port Elizabeth, South Africa.

The workpiece was securely clamped on a rigid, smooth, and mild steel backing plate, which was able to withstand the significant perpendicular and lateral forces developed during the friction stir process. The clamping system on the I-STIR PDS system was employed to effectively clamp the aluminium alloy (AA1050) plate into position during the FSP procedure. The dimensions of the backing plate used were $650 \times 265 \times 25 \text{ mm}^3$ made from mild steel plate bolted to the weld bed. The experimental setup showing the clamping fixture and the backing plate system is as presented in Figure 5.

The weld matrix employed consists of nine (9) welds with the parameters selected according to the limit of the welding platform. A full factorial design of experiment was employed in selecting the process parameters and is presented in Table 2. The rotational speeds employed were 800, 1200, and 1600 rpm and the feed rates were 100, 200, and 300 mm/min both representing the low, medium, and high settings, respectively. The Design-Expert 8, statistical software, was employed to analyze the results obtained.

All the nine processed samples and the as-received materials were cut into the required sample sizes for material characterization such as microstructural evaluation, microhardness measurement, and the wear testing. The water jet cutting technique was employed in order to ensure that additional heat that may influence and alter the properties of the processed samples is not generated and also to ensure good result integrity. The microhardness measurement was conducted using Vickers microhardness tester of diamond indenter using 300 g load and a dwell time of 15 seconds.

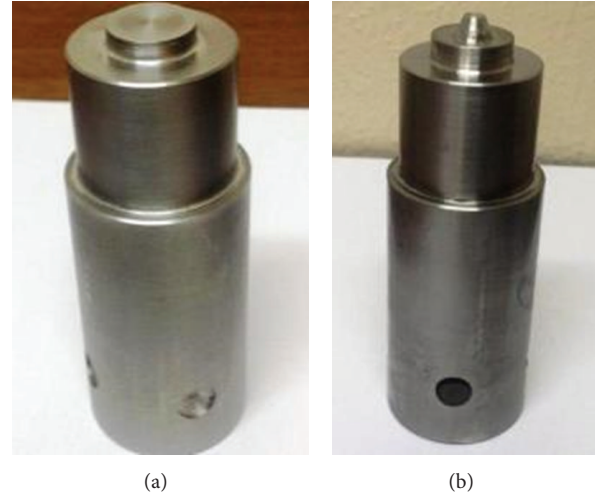


FIGURE 3: Schematic of the tool types, (a) pinless tool and (b) tool with a pin.

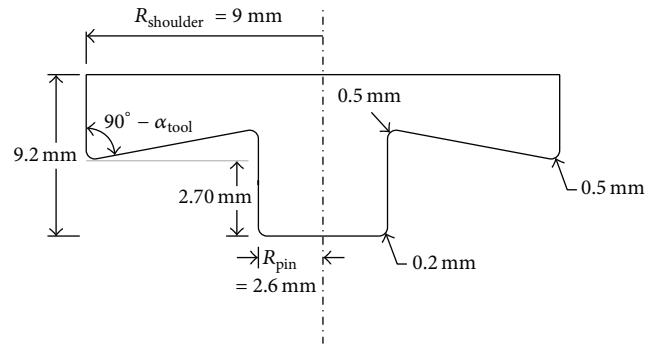


FIGURE 4: Tool dimensional drawing showing the pin and shoulder.

TABLE 2: Process parameter matrix of the FSP.

Weld designation	Rotational speed (rpm)	Feed rate (mm/min)
A	800	100
B	800	200
C	800	300
D	1200	100
E	1200	200
F	1200	300
G	1600	100
H	1600	200
I	1600	300

The wear tests were evaluated on both the as-received and processed samples using a tribometer (CETRUMT200). The wear resistance test was performed under dry condition using a ball on disk arrangement. The material of the ball is a tungsten carbide of 10 mm diameter and at a load of 25 N with a reciprocating frequency of 20 Hz and at a 2000 m sliding distance. The wear tracks were studied under the scanning electron microscope (SEM).

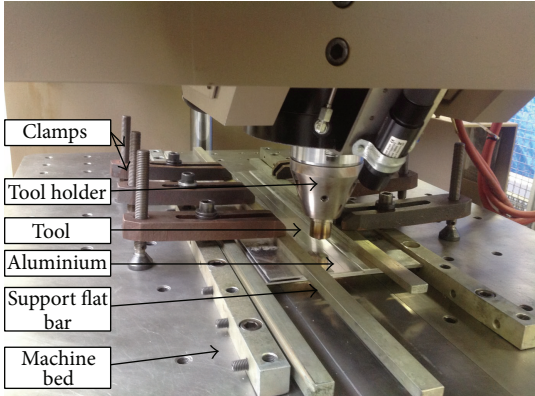


FIGURE 5: Experimental setup.

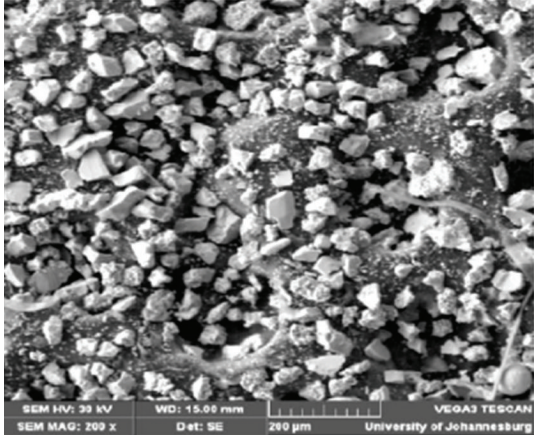


FIGURE 6: SEM micrograph of the TiC powder [45].



FIGURE 7: Photographs of samples A, B, and C.

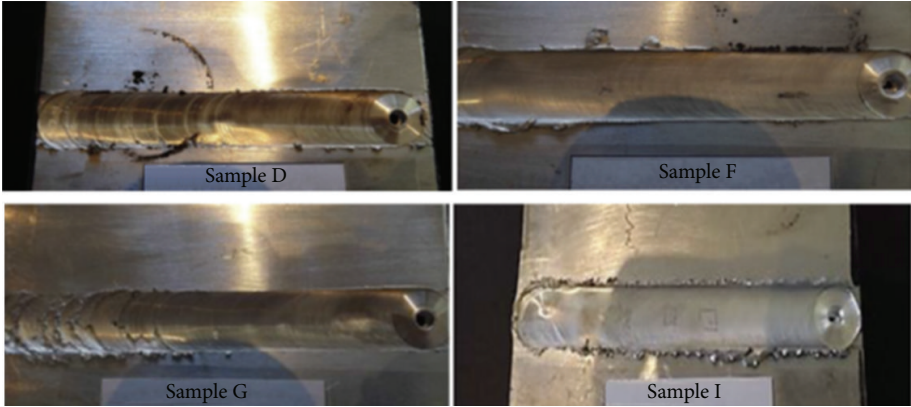


FIGURE 8: Photographs of samples D, F, G, and I.

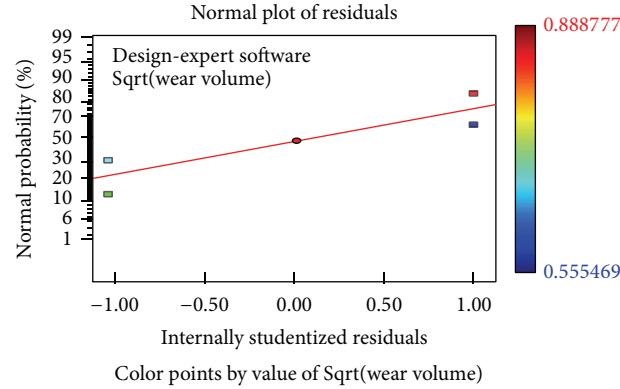


FIGURE 9: Graph of normal residual plot.

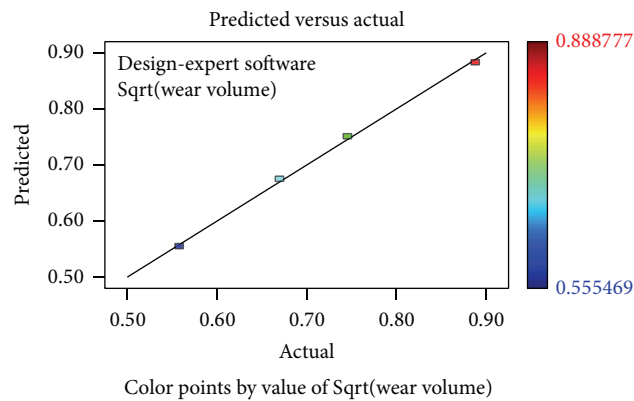


FIGURE 10: Graph of predicted versus actual experimental data.

3. Results and Discussions

The micrograph of the TiC powder used is shown in Figure 6. The TiC powder is a ball milled powder with irregular shape. The photographs of some of the processed samples are shown in Figure 7. The samples A, B, and C are characterized by visual defects as shown in Figure 7 even on repeated welds, and as such, further characterizations were not performed on them. A wormhole defect that resulted from insufficient metal flow of the advancing side above the swirl zone was seen in sample A. It was created by the unsuitable combination of the processing parameters employed in this regard. Surface galling was seen in samples B and C, which resulted from the parameters used as well. It was visually noticeable by the galling of the metal on the top surface of the weld beneath the pin tool. Hence, the process parameters employed to produce these welds were considered inappropriate in this case. The remaining samples showed good surface appearances. Some of the photographs of the other samples are shown in Figure 8.

The results of the wear test and the average Vickers microhardness of the processed samples and the parent material are presented in Table 3.

Table 3 represents the full factorial design of experiment and the results were analyzed using Design-Expert 8, statistical software.

The analysis of variance (ANOVA) for the selected factorial model is presented in Table 4.

Further analysis of variance is shown in Table 5. The “predicted R -squared” of 0.9729 is in reasonable agreement with the “adjusted R -squared” of 0.9949. The “adequate precision” measures the signal to noise ratio. A ratio greater than 4 is desirable. The ratio of 38.429 indicates an adequate signal and this model can be used to navigate the design space. The coefficient of the model terms is presented in Table 6 and the final model equation is shown in (1).

The model F -value of 294.61 implies that the model is significant. There is only a 4.12% chance that a “model F value” this large could occur due to noise. Values of “Prob > F ” which are less than 0.0500 indicate that the model terms are significant. In this case, A (rotational speed) and B (feed rate) are significant model terms.

The final equation in terms of actual factors is hereby presented:

$$\begin{aligned} \text{Sqrt (Wear Volume)} = & -0.13820 + 5.22006E - 004 \\ & * \text{Rotational speed} \\ & + 6.22528E - 004 * \text{Feed Rate.} \end{aligned} \quad (1)$$

TABLE 3: Wear volume and microhardness results.

Sample designation	Rotational speed (rpm)	Feed rate (mm/min)	Wear volume (mm ³)	Vickers microhardness (HV)
D	1200	100	0.308546	39.9
E	1200	200	0.381606	41.1
F	1200	300	0.448846	43.5
G	1600	100	0.568903	46.8
H	1600	200	0.761349	48.1
I	1600	300	0.789925	51.5
PM	—	—	0.907572	28.9

TABLE 4: Analysis of variance (ANOVA) for the selected factorial model.

Source	Sum of squares	df	Mean square	F value	P value	Prob > F
Model	0.059	2	0.030	294.61	0.0412	significant
A—Rotational speed	0.044	1	0.044	434.67	0.0305	
B—Feed rate	0.016	1	0.016	154.55	0.04911	
Residual	1.003E – 004	1	1.003E – 004			
Cor total	0.059	3				

TABLE 5: Model analysis.

Std. Dev.	0.010	R-squared	0.9983
Mean	0.72	Adj. R-squared	0.9949
C.V. %	1.40	Pred. R-squared	0.9729
PRESS	1.605E – 003	Adeq. precision	38.429

The graph of normal residual plot is shown in Figure 9 and the graph of predicted versus actual experimental data is shown in Figure 10. The residual is randomly distributed and it can also be seen that the model is in good agreement with the experimental data as shown in Figure 10.

The main effect plots of the effect of processing parameters on the wear volume loss are shown in Figure 11. The wear volume was found to increase as the rotational speed was increased as shown in Figure 11(a). Too high rotational speed for a relatively soft material such as pure aluminium tends to generate high amounts of heat that resulted in lots of mixing of the substrate and the powder. However, dilution needs to be minimized in order to improve the wear resistance of the surface; hence the advantage of using FSP as melting does not occur during the process.

The wear volume loss was also found to increase with the increase in the feed rate as shown in Figure 11(b). This can be attributed to improper melting of the TiC powder at high feed rate which would aggravate the wear action.

The surface plot showing the interaction between the rotational speed and the feed rate effect on wear volume is shown in Figure 12. It can be seen that the highest wear occurs at the highest rotational speed and the lowest feed rate. This is because of excessive heat generated at this combination of processing parameters which resulted in high dilution rate and softening of the composite. This would reduce the wear resistance property of the surface.

The microhardness results were also analyzed in a similar way and the equation of the model is presented as

$$\begin{aligned} \text{Sqrt (Microhardness)} = & + 4.47777 + 1.39125E - 003 \\ & * \text{Rotational speed} \\ & + 1.52838E - 003 * \text{Feed Rate.} \end{aligned} \quad (2)$$

The main effect plots of the microhardness against processing parameter are shown in Figure 13.

Figure 13(a) shows that the microhardness increases as the rotational speed increases. This can be attributed to the fact that at high feed rate, and low rotational speed, too large unmelted TiC powder is produced which aggravated the wear action. But as the rotational speed was increased, the volume of unmelted powder was reduced and the microhardness was improved which also improved the wear resistance property. The microhardness was found to increase as the feed rate was increased at high rotational speed as shown in Figure 13(b). This is because increasing the feed rate at high rotational speed would reduce the high heat generated and improve the microhardness property. However, the higher microhardness observed at high feed rate did not translate to high wear resistance property because, at high feed rate, the amount of unmelted TiC powder was increased which would increase the microhardness value but would aggravate the wear action.

The analysis of the wear tracks further confirms the effect of the processing parameters on the wear resistance behavior of the samples. Figure 14(a) shows the SEM micrograph of the wear track of sample D.

The SEM images are characterized predominantly by abrasive wear. There was moderate quantity of unmelted carbide which during the sliding wear action was rubbing against the surface of the substrate. This unmelted carbide later forms

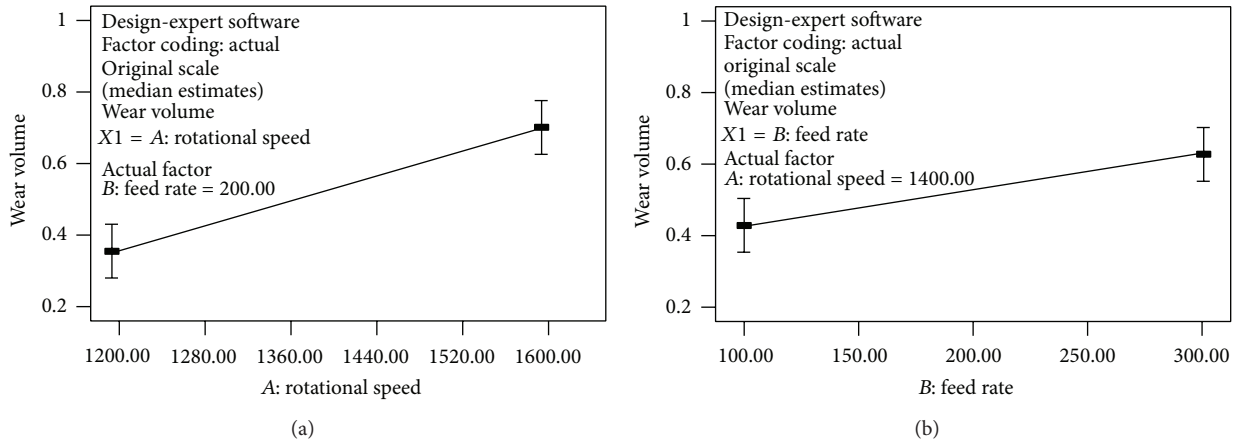


FIGURE 11: Main effect plot of (a) wear volume against rotational speed and (b) wear volume against feed rate.

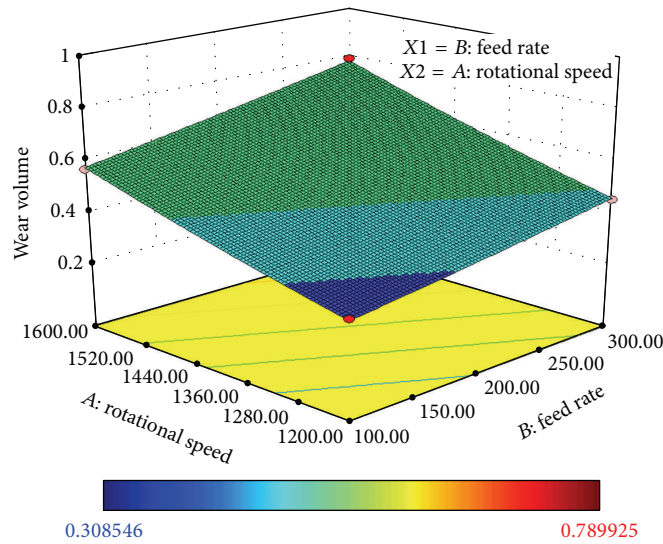


FIGURE 12: The surface plot of wear volume against rotational speed and feed rate.

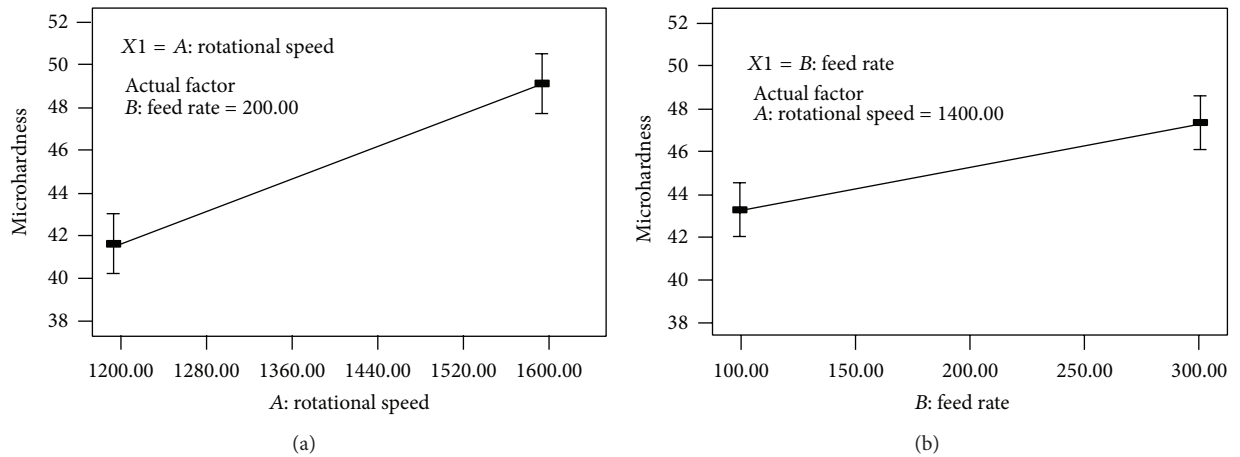


FIGURE 13: Main effect plot of (a) microhardness against rotational speed and (b) wear volume against feed rate.

TABLE 6: The coefficient of the model terms.

Factor	Coefficient estimate	df	Standard error	95% CI low	95% CI high	VIF
Intercept	0.72	1	$5.008E - 003$	0.65	0.78	
A—Rotational speed	0.10	1	$5.008E - 003$	0.041	0.17	1.00
B—Feed rate	0.062	1	$5.008E - 003$	$-1.374E - 003$	0.13	1.00

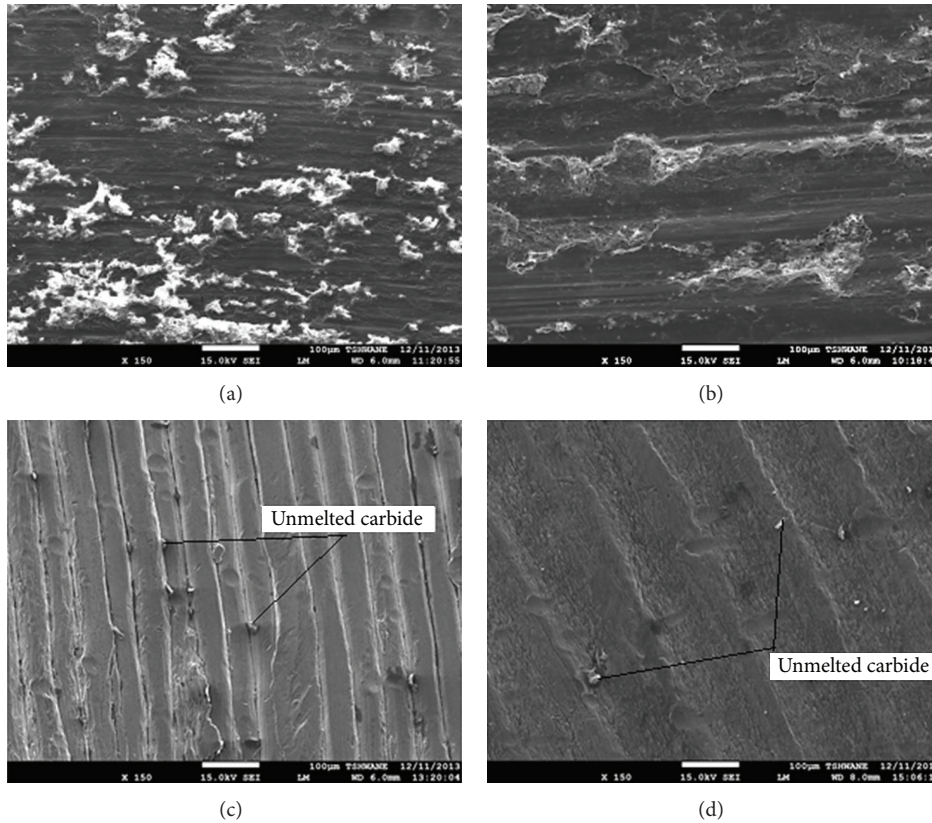


FIGURE 14: SEM micrograph of wear track of (a) sample D, (b) sample F, (c) sample G, and (d) sample I.

powder that reduces the wear action by forming a powder lubricant. As the feed rate was increased, the unmelted carbide (UMC) was also increased which aggravated the wear action by scratching deep into the substrate and forming ridges as shown in Figure 14(b). Increasing the rotational speed resulted in high heat generation which causes much of the TiC powder to be completely melted. This makes the composite become softer and the few remaining unmelted carbide scratches deep into the substrate and aggravated the wear action as shown in Figure 14(c). The size of the unmelted carbide increases as the feed rate was increased as shown in Figure 14(d); this makes the wear action become more severe as the sliding wear was progressing thereby producing deeper cut on the sliding surfaces.

In order to validate the developed models to demonstrate the robustness of the models, a set of experiments were performed with settings outside the ones used in the model building. The results are presented in the next section.

4. Model Validation

To validate models, a set of experiments were performed at the processing parameters different from the processing parameters used in the building of the model. The results are presented in Table 7. The graph of the predicted versus the experimental data is also shown in Figure 15. The graph of actual values versus actual experimental data of wear volume is shown in Figure 15(a) and that of the microhardness is shown in Figure 15(b). The graphs show that there is a good agreement between the model and the experimental data. Therefore, the models can be used to predict the wear resistance performance as well as the microhardness properties of friction stir processed Al-TiC composites.

5. Conclusion

This study revealed that the friction stir processing (FSP) can be used to improve the mechanical properties of a material

TABLE 7: Validation results.

Sample number	Rotational speed (rpm)	Feed rate (mm/min)	Predicted wear volume (mm ³)	Actual wear volume (mm ³)	Predicted Vickers microhardness (HV)	Actual Vickers microhardness (HV)
1	1400	150	0.470682	0.481104	44.29	44.84
2	1300	180	0.425811	0.412951	43.05	42.55
3	1000	300	0.325646	0.330403	40.04	40.62
4	1500	100	0.500039	0.490671	45.13	45.03
5	1500	150	0.545025	0.552107	46.16	46.55
6	1700	100	0.658575	0.662192	48.94	49.59

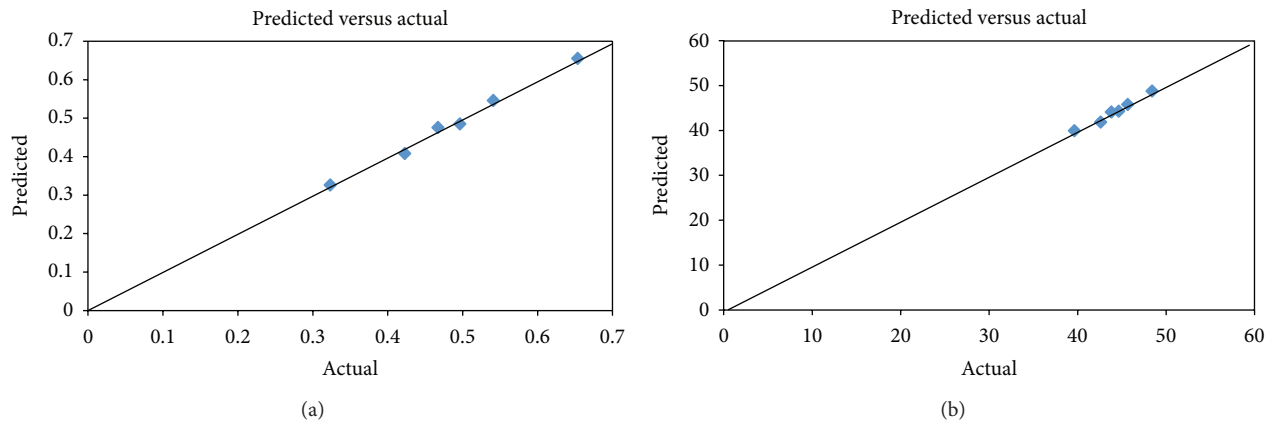


FIGURE 15: The graph of predicted versus actual experimental data of (a) wear volume and (b) Vickers microhardness.

and the production of surface layer composites. The effect of processing parameters on the wear resistance behavior of friction stir processed Al-TiC composites was investigated in this research. The rotational speed and the feed rate effect on the wear resistance property of Al-TiC composite produced through FSP were statistically analyzed in design expert and models were developed to predict the wear volume and microhardness properties of the Al-TiC processed samples. The models were validated through additional experiments performed at processing parameters outside the processing parameters used in building the models. The model was found to be in good agreement with the experimental data. It was shown that the right combination of these processing parameters was necessary to really improve the wear resistance property of the composite produced. At low rotational speed, there was insufficient melting of the TiC powder which resulted in surface defect. Also, too high rotational speed generated too high heat that resulted in lots of dilution of the TiC and Al which reduces the wear resistance property. A moderately high rotational speed of 1200 rpm and low speed rate of 100 mm/min produced the surface composited layer with the best wear resistance property based on the set of processing parameters considered in this study and can be considered as the optimum parameter window.

Conflict of Interests

The authors declare that there is no conflict of interests regarding the publication of this paper.

Acknowledgments

The authors would like to acknowledge the Tertiary Education Support Program funding of ESKOM South Africa and the eNtsa Research Group of Nelson Mandela Metropolitan University (NMMU), Port Elizabeth, South Africa, for allowing us to use their facility to produce the welds.

References

- [1] R. S. Mishra and M. W. Mahoney, "Friction stir processing: a new grain refinement technique to achieve high strain rate superplasticity in commercial alloys," *Materials Science Forum*, vol. 357, no. 3, pp. 507–512, 2001.
- [2] R. S. Mishra and Z. Y. Ma, "Friction stir welding and processing," *Materials Science and Engineering R: Reports*, vol. 50, no. 1-2, pp. 1–78, 2005.
- [3] W. M. Thomas and E. D. Nicholas, "Friction stir welding for the transportation industries," *Materials and Design*, vol. 18, no. 4–6, pp. 269–273, 1997.
- [4] Z. Y. Ma, "Friction stir processing technology: a review," *Metallurgical and Materials Transactions A: Physical Metallurgy and Materials Science*, vol. 39, no. 3, pp. 642–658, 2008.
- [5] C. J. Dawes and W. Thomas, "Development of improved tool designs for friction stir welding of aluminium," in *Proceedings of the International Symposium of Friction Stir Welding*, Los Angeles, Calif, USA, June 1999.
- [6] A. Thangarasu, N. Murugan, I. Dinaharan, and S. J. Vijay, "Microstructure and microhardness of AA1050/TiC surface

- composite fabricated using friction stir processing,” *Sadhana*, vol. 37, no. 5, pp. 579–586, 2012.
- [7] R. Mishra, Z. Ma, and J. Spowart, *Friction Stir Welding and Processing II*, TMS, 2003.
- [8] R. Bauri, D. Yadav, and G. Suhas, “Effect of friction stir processing (FSP) on microstructure and properties of Al-TiC in situ composite,” *Materials Science and Engineering A*, vol. 528, no. 13–14, pp. 4732–4739, 2011.
- [9] E. Akinlabi, *Characterisation of Dissimilar Friction Stir Welds Between 5754 Aluminium Alloy and C11000 Copper*, Port Elizabeth, 2010.
- [10] R. Johnson and S. Kallee, “Friction stir welding technology,” *Materials World*, vol. 7, no. 12, pp. 751–753, 1999.
- [11] Y. X. Gan, D. Solomon, and M. Reinbolt, “Friction stir processing of particle reinforced composite materials,” *Materials*, vol. 3, no. 1, pp. 329–350, 2010.
- [12] M. Jariyaboon, P. Møller, R. E. Dunin-Borkowski, S.-I. In, I. Chorkendorff, and R. Ambat, “The effect of atmospheric corona treatment on AA1050 aluminium,” *Corrosion Science*, vol. 52, no. 6, pp. 2155–2163, 2010.
- [13] I. Topic, H. W. Höppel, and M. Göken, “Friction stir welding of accumulative roll-bonded commercial-purity aluminium AA1050 and aluminium alloy AA6016,” *Materials Science and Engineering A*, vol. 503, no. 1–2, pp. 163–166, 2009.
- [14] H. N. B. Schmidt, T. L. Dickerson, and J. H. Hattel, “Material flow in butt friction stir welds in AA2024-T3,” *Acta Materialia*, vol. 54, no. 4, pp. 1199–1209, 2006.
- [15] M. Jariyaboon, A. J. Davenport, R. Ambat, B. J. Connolly, S. W. Williams, and D. A. Price, “The effect of welding parameters on the corrosion behaviour of friction stir welded AA2024-T351,” *Corrosion Science*, vol. 49, no. 2, pp. 877–909, 2007.
- [16] H. Li, D. MacKenzie, and R. Hamilton, “Parametric finite-element studies on the effect of tool shape in friction stir welding,” *Proceedings of the Institution of Mechanical Engineers B: Journal of Engineering Manufacture*, vol. 224, no. 8, pp. 1161–1173, 2010.
- [17] M. M. Attallah and H. G. Salem, “Friction stir welding parameters: a tool for controlling abnormal grain growth during subsequent heat treatment,” *Materials Science and Engineering A*, vol. 391, no. 1–2, pp. 51–59, 2005.
- [18] E. A. El-Danaf, M. M. El-Rayes, and M. S. Soliman, “Low temperature enhanced ductility of friction stir processed 5083 aluminum alloy,” *Bulletin of Materials Science*, vol. 34, no. 7, pp. 1447–1453, 2011.
- [19] S. P. Vaze, J. Xu, R. J. Ritter, K. J. Colligan, J. J. Fisher Jr., and J. R. Pickens, “Friction stir processing of aluminum alloy 5083 plate for cold bending,” *Materials Science Forum*, vol. 426–432, no. 4, pp. 2979–2986, 2003.
- [20] M. Reis, R. Louro, P. J. Morais, L. Santos, and H. Gouveia, “Microstructural characterisation of 5083 Al alloy joints friction stir welded,” *Materials Science Forum*, vol. 514–516, no. 1, pp. 510–515, 2006.
- [21] G. Çam, S. Güçlüer, A. Çakan, and H. T. Serinda, “Mechanical properties of friction stir butt-welded Al-5086 H32 plate,” *Materialwissenschaft und Werkstofftechnik*, vol. 30, no. 2, pp. 151–156, 2008.
- [22] M. Merzoug, M. Mazari, L. Berrahal, and A. Imad, “Parametric studies of the process of friction spot stir welding of aluminium 6060-T5 alloys,” *Materials and Design*, vol. 31, no. 6, pp. 3023–3028, 2010.
- [23] V. Fahimpour, S. K. Sadrnezhaad, and F. Karimzadeh, “Corrosion behavior of aluminum 6061 alloy joined by friction stir welding and gas tungsten arc welding methods,” *Materials and Design*, vol. 39, pp. 329–333, 2012.
- [24] P. A. Colegrove and H. R. Shercliff, “Development of Trivex friction stir welding tool part 1—two-dimensional flow modelling and experimental validation,” *Science and Technology of Welding and Joining*, vol. 9, no. 4, pp. 345–351, 2004.
- [25] M. L. Santella, T. Engstrom, D. Storjohann, and T.-Y. Pan, “Effects of friction stir processing on mechanical properties of the cast aluminum alloys A319 and A356,” *Scripta Materialia*, vol. 53, no. 2, pp. 201–206, 2005.
- [26] C. J. Hsu, P. W. Kao, and N. J. Ho, “Ultrafine-grained Al-Al₂Cu composite produced in situ by friction stir processing,” *Scripta Materialia*, vol. 53, no. 3, pp. 341–345, 2005.
- [27] E. R. I. Mahmoud, M. Takahashi, T. Shibayanagi, and K. Ikeuchi, “Wear characteristics of surface-hybrid-MMCs layer fabricated on aluminum plate by friction stir processing,” *Wear*, vol. 268, no. 9–10, pp. 1111–1121, 2010.
- [28] A. Emamian, S. F. Corbin, and A. Khajepour, “In-situ deposition of metal matrix composite in Fe-Ti-C system using laser cladding process,” in *Metal, Ceramic and Polymeric Composites for Various Uses*, J. Cuppoletti, Ed., InTech, 2011.
- [29] J. Zhang, Z. Fan, Y. Q. Wang, and B. L. Zhou, “Microstructural development of Al-15wt.%Mg₂Si in situ composite with mischmetal addition,” *Materials Science and Engineering A*, vol. 281, no. 1–2, pp. 104–112, 2000.
- [30] Y. Chen and D. D. L. Chung, “In situ Al-TiB composite obtained by stir casting,” *Journal of Materials Science*, vol. 31, no. 2, pp. 311–315, 1996.
- [31] D. Yadav and R. Bauri, “Fabrication of metal particles embedded aluminum matrix composite by friction stir processing (FSP),” *AIP Conference Proceedings*, vol. 1315, pp. 51–57, 2011.
- [32] A. Kurt, I. Uygur, and E. Cete, “Surface modification of aluminium by friction stir processing,” *Journal of Materials Processing Technology*, vol. 211, no. 3, pp. 313–317, 2011.
- [33] Z. Y. Ma, “Friction stir processing technology: a review,” *Metallurgical and Materials Transactions A: Physical Metallurgy and Materials Science*, vol. 39, no. 3, pp. 642–658, 2008.
- [34] K. J. Hodder, H. Izadi, A. G. McDonald, and A. P. Gerlich, “Fabrication of aluminum-alumina metal matrix composites via cold gas dynamic spraying at low pressure followed by friction stir processing,” *Materials Science and Engineering A*, vol. 556, pp. 114–121, 2012.
- [35] A. Pirondi and L. Collini, “Analysis of crack propagation resistance of Al-Al₂O₃ particulate-reinforced composite friction stir welded butt joints,” *International Journal of Fatigue*, vol. 31, no. 1, pp. 111–121, 2009.
- [36] A. H. Feng, B. L. Xiao, and Z. Y. Ma, “Effect of microstructural evolution on mechanical properties of friction stir welded AA2009/SiCp composite,” *Composites Science and Technology*, vol. 68, no. 9, pp. 2141–2148, 2008.
- [37] Z. Fan, A. P. Miodownik, L. Chandrasekaran, and M. Ward-Close, “The Young’s moduli of in situ Ti/TiB composites obtained by rapid solidification processing,” *Journal of Materials Science*, vol. 29, no. 4, pp. 1127–1134, 1994.
- [38] M. Raafi, T. S. Mahmoud, H. M. Zakaria, and T. A. Khalifa, “Microstructural, mechanical and wear behavior of A390/graphite and A390/Al₂O₃ surface composites fabricated using FSP,” *Materials Science and Engineering A*, vol. 528, no. 18, pp. 5741–5746, 2011.
- [39] K. Surekha, B. S. Murty, and K. Prasad Rao, “Comparison of corrosion behaviour of friction stir processed and laser melted AA

- 2219 aluminium alloy,” *Materials and Design*, vol. 32, no. 8-9, pp. 4502–4508, 2011.
- [40] W. Xu and J. Liu, “Microstructure and pitting corrosion of friction stir welded joints in 2219-O aluminum alloy thick plate,” *Corrosion Science*, vol. 51, no. 11, pp. 2743–2751, 2009.
- [41] E. Bousquet, A. Poulon-Quintin, M. Puiggali, O. Devos, and M. Touzet, “Relationship between microstructure, microhardness and corrosion sensitivity of an AA 2024-T3 friction stir welded joint,” *Corrosion Science*, vol. 53, no. 9, pp. 3026–3034, 2011.
- [42] X. Li and M. J. Starink, “Analysis of precipitation and dissolution in overaged 7xxx aluminium alloys using DSC,” *Materials Science Forum*, vol. 331–337, pp. 1071–1076, 2000.
- [43] B. Zahmatkesh, M. H. Enayati, and F. Karimzadeh, “Tribological and microstructural evaluation of friction stir processed Al2024 alloy,” *Materials and Design*, vol. 31, no. 10, pp. 4891–4896, 2010.
- [44] S. Jerome, S. Bhalchandra, S. Babu, and B. Ravisankar, “Influence of microstructure and experimental parameters on mechanical and wear properties of Al-TiC surface composite by FSP route,” *Journal of Minerals and Materials Characterization and Engineering*, vol. 11, no. 5, pp. 493–507, 2012.
- [45] R. M. Mahamood, E. T. Akinlabi, M. Shukla, and S. Pityana, “Characterization of laser deposited Ti6A4V/TiC composite,” *Journal of Lasers in Engineering*. In press.

Research Article

Advantages of the Green Solid State FSW over the Conventional GMAW Process

Hasan I. Dawood,^{1,2} Kahtan S. Mohammed,¹ and Mumtaz Y. Rajab³

¹ School of Materials Engineering, Universiti Malaysia Perlis, Taman Muhibah-Jejawi, 02600 Arau, Perlis, Malaysia

² Chemical Engineering Department, AL-Qadisiyah University, Iraq

³ Mechanical Engineering Department, AL-Qadisiyah University, Iraq

Correspondence should be addressed to Hasan I. Dawood; hassanissa1972@gmail.com

Received 10 January 2014; Revised 15 March 2014; Accepted 17 March 2014; Published 28 May 2014

Academic Editor: Achilles Vairis

Copyright © 2014 Hasan I. Dawood et al. This is an open access article distributed under the Creative Commons Attribution License, which permits unrestricted use, distribution, and reproduction in any medium, provided the original work is properly cited.

The present work is an experimental comparison between the friction stir welding (FSW) and the conventional gas metal arc welding (GMAW) in joining of Al alloys. Two sets of 3 mm thick aluminum strip pairs were friction stir welded in a regular butting joint configuration. Two rotational speeds of 1750 rpm and 2720 rpm were utilized to perform the FSW process. The axial force and the transverse speed were kept constant at 6.5 KN and 45 mm/min, respectively. Cylindrical tool shoulder and pin geometry were selected. Strip pairs of other similar sets were butt jointed using the conventional GMAW. The welding quality, power input, and macrostructure and microstructure of the butted joints were examined. The types of the fumes and the amount of the released gases were measured and compared. The results showed that the solid state FSW is green, environment-friendly, and of superior welding properties compared to the conventional GMAW.

1. Introduction

FSW is a solid state welding process which can afford a high quality of welds even for materials that are unmanageable with conventional welding such as aluminum. It is a clean, environment-friendly, and nonharmful process as it is accompanied by neither an arc formation and radiation nor toxic gas emission. It has low heat input and almost no welds finishing costs [1, 2]. FSW gives several advantages over other welding techniques for joining various alloys, especially light alloys [3]. Owing to certain properties such as light weight, high strength to weight ratio, and good corrosion resistance, aluminum alloys are used in wide applications, including aerospace, automobile industries, shipbuilding, and train and tram wagons. They are also used in offshore structures and bridge construction. So far FSW has been widely applied to welding of low melting alloys which are difficult to be joined by any other conventional fusion welding such as Al-Li 2195 alloy [4]. The process and terminology of FSW are schematically represented in Figure 1.

During FSW, heat input for welding is provisioned by the rubbing action of the tool shoulder with the top surface of the

welded piece and by the plastic dissipation of the mechanical energy generated by the tool pin [5]. However, Roy et al. [6] and Hirata et al. [7] reported that the heat flow from the pin is relatively small compared to flow from the shoulder and thus it can be ignored. The heat input creates a softened plasticized metal around the tool and facilitates its transverse movement along the joint line. The plasticized metal is mixed, sheared, and extruded around the rotating tool pin in the vertical direction under the applied axial force. Eventually, the plasticized metal is forged by the contact of the tool shoulder and the pin resulting in a solid phase bond between the two pieces. During the welding process, advancing side is the side which the velocity vector of rotational speed is in the same direction with the welding speed and the other side which represent the retreating side. The FSW process leads to the appearance of thermomechanically affected zone (TMAZ), a heat affected zone (HAZ), and a nugget zone (NZ) which is of a vase-like shape in the central part of the TMAZ. The main FSW parameters that determine the quality of the welded joint are the tool plunge force, the tool rotation speed, and the travel or traverse speed [8].

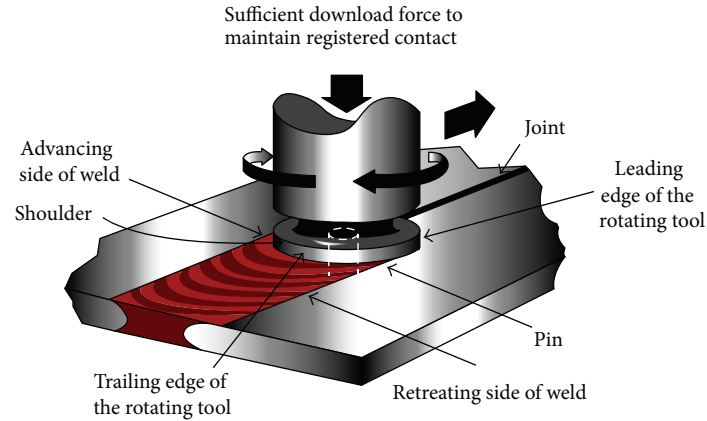


FIGURE 1: The schematic representation of FSW process.

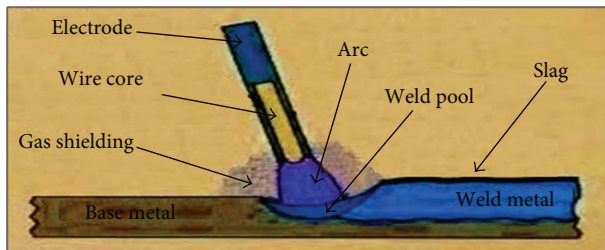


FIGURE 2: The schematic diagram of the welding process by GMAW.



FIGURE 3: Photograph of the clamped Al strips.

GMAW is a conventional arc welding process [9]. Schematic representation of this process is shown in Figure 2 [9]. Throughout welding, heat input is an important characteristic; it influences the cooling rate and consequently the mechanical properties and the metallurgical structure of both the WZ and the HAZ [10]. GMAW welding process is performed at temperatures above the melting temperature of the workpiece. The higher temperature process needs higher power and can induce lots of defects in the welded piece such as distortion, cracking, and higher residual stresses which result in inferior mechanical properties [8].

In this study, two sets of 3 mm thick aluminum strip pairs were friction stir welded together at rotational speeds of 1750 rpm and 2720 rpm. Welding process for another similar set of pairs was repeated using the conventional GMAW. Several papers are found comparing FSW with different conventional fusion arc welding processes; few of them are on welding of Al alloy [1, 11, 12]. The aim of this paper is to study the influence of FSW and GMAW on microstructure evolution and the quality of the Al-Al weld joints and to assess their impact on the environment.

2. Materials and Experimental Procedures

3 mm thick 1030 Al strips with a nominal chemical composition of 0.114% Si, 0.405% Fe, 0.084% Cu, 0.011% Mn, 0.032% Mg, 0.017% Ti and Al balance were used in this investigation. The FSW and the GMAW joints were of butt type. They were performed on a milling machine. Prior to welding, the metal

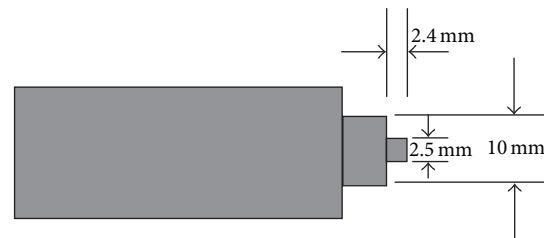


FIGURE 4: The tool shoulder and pin configuration diagram [8].

pairs were cleaned using acetone to remove any grease and stains that may affect the quality of welding. The metal pair was fixed by clamps to prevent any movement during the welding process as shown in Figure 3.

The horizontalness of the clamped pair on the milling machine was assured by horizontal level indicator for all Al-Al weld joints. Figure 4 shows that the utilized tool dimensions (shoulder and pin) were made of medium carbon steel (0.424% C, 0.727% Mn, 0.013% P, and 0.17% Si, and Fe balance). The tool was heat-treated and quenched to RC 56. The vertical milling machine used in this work was about 3 horsepower (2237 watts).

In GMAW, the type of the welding current was a DC electropositive current and the shielding gas used was pure argon. The diameter of the aluminum filler wire was 1.0 mm. It had chemical composition of Mn (0.05–0.20%), Si (0.25%), Fe (0.40%), and Cr (0.05–0.20%) and Al balance with the code

reference of ER5356. The heat input was calculated as the ratio of the power (voltage \times current) to the velocity of the heat source (the arc) as follows [10]:

$$H = \frac{60EIL}{1000S}, \quad (1)$$

where H , E , and I are the heat input in KJ, the arc voltage in volts, and the current in amps, respectively. S is the travel speed in mm/min. L is the length of weldments in millimeters. The welding current and the welding voltage were measured to be 120 A and 20 V, respectively.

In this investigation, it was found that the travel speed of 45 mm/min for FSW and GMAW is almost similar. The results showed that for FSW sound defect free welds were obtained as opposed to GMAW, where a weld defect was detected.

The heat input per unit length of FSW process was calculated according to the following formula [6]:

$$H = f\sigma_yAL, \quad (2)$$

where f is the ratio in which the heat generated at the tool shoulder/workpiece interface was transported between the tool and the workpiece, σ_y is the yield stress of the metal at $0.8T_s$, T_s is the solidus temperature, and A is the cross-sectional area of the tool shoulder. L is the length of the weldment. The value of f for FSW of aluminum alloy with steel tool is found to be $>90\%$. [6]. Accordingly, the heat input to weld the entire joint of 5 cm in length was calculated for both GMAW and FSW and it was found for GMAW to be four times that of FSW.

Sample preparation for metallography test was performed according to the ASTM E3 (Standard Guide of Metallographic Specimens) [13]. All samples (except for tensile test) were ground, polished, and etched for macrostructure, microstructure, and microhardness test according to the ASTM E407 (Standard Practice for Microetching Metals and Alloys) [14]. The etchant used for aluminum alloys was Keller's reagent which is a mixture of 3 mL hydrochloric acid, 5 mL nitric acid, 2 mL hydrofluoric acid, and 190 mL distilled water.

The tensile test was conducted according to the standard test method for metallic materials (ASTM E8) [15]. The Vickers microhardness test (Hv) was conducted according to the standard test for microhardness of metallic materials (ASTM E384) [16]. The hardness applied load was 1 kg and the dwell time was 8 seconds.

3. Results and Discussion

3.1. Characterization of the Surface and Root Joints. Figure 5 shows the profile of the Al-Al friction stir welded joints at a rotational speed of 1750 rpm and traverse speed of 45 mm/min. Figure 5(a) reveals the weld profile at the top of the plate to be rough and spattered. The partially delaminated onion ring pattern is evident. This occurs due to insufficient heat generation in the shoulder rubbing action with the top surface of the plate [17]. In Figure 5(b) the lack of root penetration defect and the incomplete filled groove are

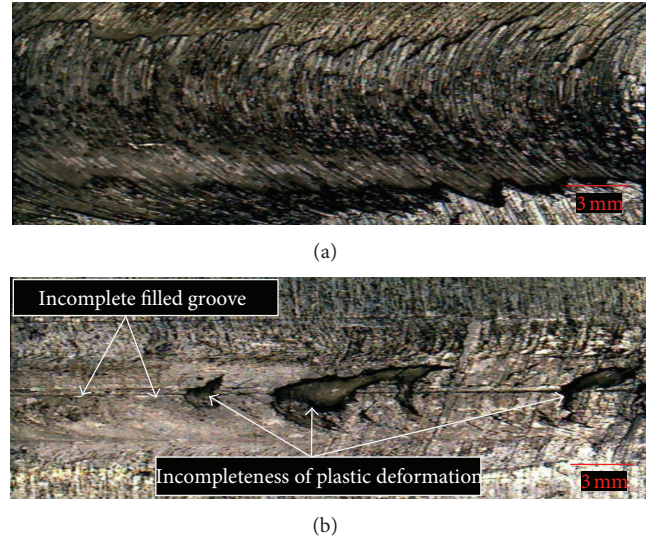


FIGURE 5: The weld profile of the Al-Al friction stir welded joints at a rotational speed of 1750 rpm and traverse speed of 45 mm/min at (a) the top side and (b) the bottom side.

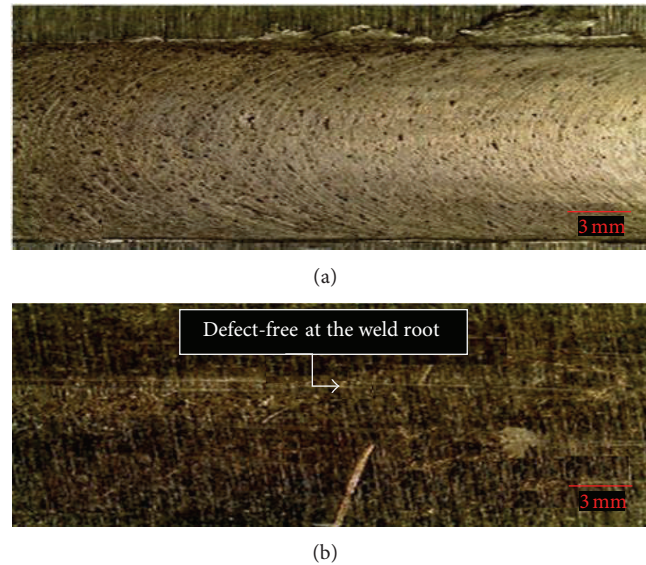


FIGURE 6: The weld profile of friction stir welded Al-Al joint at rotational speed of 2720 rpm and traverse speed of 45 mm/min at (a) top side and (b) bottom side.

eminent. This might be attributed to the shortness of the pin which resulted in poor penetration down to the bottom of the welded piece which in turn resulted in an insufficient heat flow, one that is necessary to deform, plasticize, and join the bottom sides together. The pin plunging depth is a critical factor and difficult to be controlled. The depth of sinking must be constant during the welding process. However, that is very difficult to achieve without assuring a horizontal surface leveling particularly for joining long workpieces [18].

Figure 6 shows the profile of the Al-Al friction stir welded joints at a rotational speed of 2720 rpm. Figure 6(a) depicts

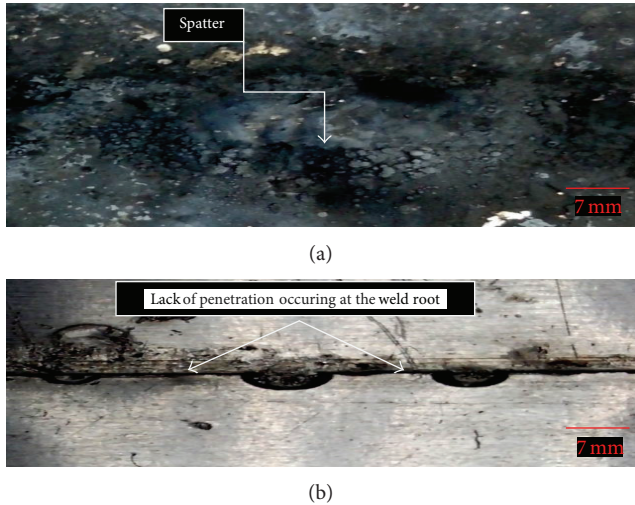


FIGURE 7: The weld profile of the Al-Al GMAW welded joint at (a) the top side and (b) the bottom side.

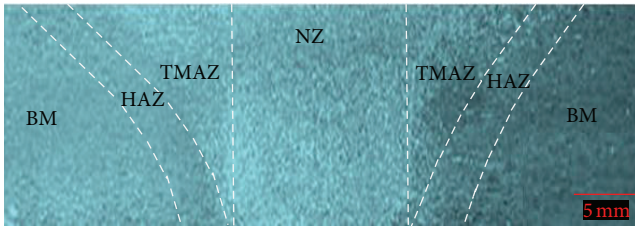


FIGURE 8: Optical image showing the macroscopic features in a cross section of the FSW butt joint.

much smoother tightly striated weldment profile compared to that joint conducted at a rotational speed of 1750 rpm. Figure 6(b) shows the bottom side of the plate; it reflects a defect-free surface. This was due to sufficient heat received on both top and bottom sides of the plate which enhanced the plasticizing of the aluminium piece during welding. Higher rotational speeds can afford better weld profile even though both the traverse speed and the applied load are kept constant [17].

Figure 7(a) shows the weld profile of the Al-Al GMAW joint at its top side. Spatters around the welded metals are evident. This might be caused by an excessive current, arc blow, damp electrode, contamination, and/or incorrect wire feed speed during the welding process. Figure 7(b) clearly shows that there is a significance of the lack of penetration occurring at the weld root of the plate. This is probably caused by the high welding speed which results in insufficient heat provisioning and is not enough to melt the bottom of the plate [19].

3.2. Microstructures Analysis. The optical low magnification image in Figure 8 shows the main features of the FSW process at the NZ. The NZ reflects a basin-like nugget zone shape. The formation of this shape on FSW is attributed to the maximal deformation and plasticization in the material of the upper

part of the NZ as opposed to that of its lower parts. The NZ in the pin shoulder side receives the uttermost amount of the frictional heat generated by the intimate contact of its surface with the cylindrical-tool shoulder. Hence it yields, flows, and flattens under the pin swirling action more than its lower part on the anvil side does and results in this basin-like nugget shape. However, so far various shapes of NZ have been observed. The evolution of the NZ shape depends on the processing parameter, tool geometry, and thermal gradient in the workpiece. Mahoney et al. [20] reported elliptical nugget zone shape in the weld of the 7075-T651 aluminum alloy rather than a basin-like shape.

Figure 9 shows the microstructure at different welding regions of the Al-Al FSW joints at a rotational speed of 1750 rpm. Figure 10 shows the microstructure at different welding regions of the Al-Al FSW joints with a rotational speed of 2720 rpm. Figures 9(a) and 10(a) show the microstructure of the original as-received base metal. The randomly distributed second phase particles appeared as small black particles. Elongation of the Al grains along the rolling direction is evident. During FSW, the base metal experiences no metallurgical changes and maintains its original cold-worked microstructure. Figures 9(b) and 10(b) show that the two NZs of the weld joints resulted from the two different rotational speeds. NZ produced at 2720 rpm has a smaller grain size as opposed to that conducted at a speed of 1750 rpm. These variations result from excess heat exposure and the intensive stirring action induced at higher rotational speeds.

Figures 9(c) and 10(c) show the NZ and the TMAZ at the two rotational speeds. It is prominent that the grain size at TMAZ is larger than the grain size at NZ. Regarding the grain size phylogeny at the NZ and the TMAZ, there are two conflicting factors acting together and affecting this process. During welding, the grains at these two regions undergo plastic deformations, mechanical shearing, and thermal exposure. Hence, they get plasticized, extruded, and rotated according to the strain levels to which they are subjected [21]. The mechanical actions of deformation, shearing, and extrusion result in smaller grain size, while the thermal exposure acts as grain size promoter. In the NZ, the mechanical actions are more severe and the outcome of these conflicting actions work in favor of dynamic recrystallization resulting in small grain size, smaller than that at the BM, TMAZ, and HAZ. This mechanical action is augmented at higher speeds and results in even smaller grain size. The TMAZ is located slightly further away from the direct effect of the rotating pin action. It is characterized by a highly deformed structure. Although the TMAZ undergoes plastic deformation, but dynamic crystallization does not occur in this zone due to insufficient deformation and strain. Consequently the thermal and mechanical interactions work in favor of thermal effect and result in grain growth. Higher rotational speed favors larger grain size. The grain size decreases as the input heat decreases.

Figures 9(d) and 10(d) show the TMAZ and the HAZ of the Al-Al welded joints. The grains at the HAZ are coarser as opposed to those at the TMAZ. The thermal exposure causes

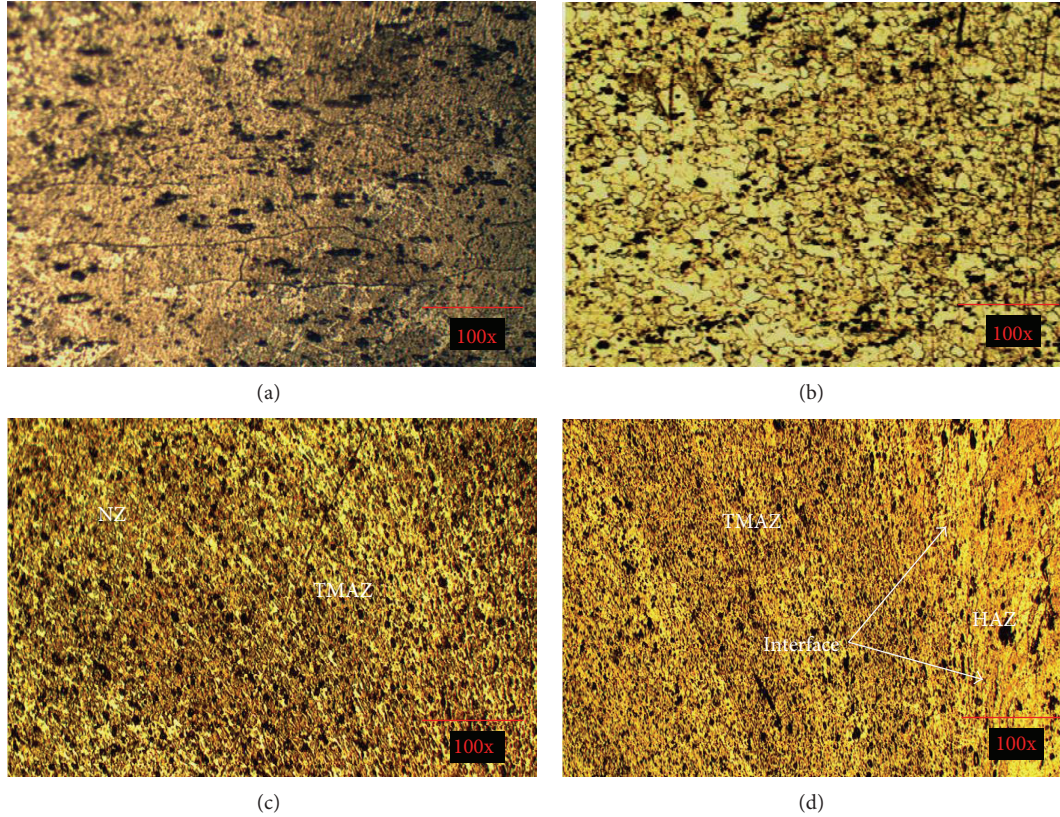


FIGURE 9: Optical images reveal the microstructures of different welding zones on Al-Al butt welded joint performed by the FSW technique at a rotational speed of 1750 rpm. (a) BM, (b) NZ, (c) NZ and TMAZ, and (d) TMAZ and HAZ 100x magnification.

TABLE 1: Grain size at different welding zones for FSW and GMAW for Al-Al joints.

Items	Range of grain size in μm of the weld regions			
	NZ/WZ	TMAZ	HAZ	BM
FSW				
Rotational speed				
1750 rpm	3.5–10	3–11	8–18	5–16
2720 rpm	2–8	3.5–13	8–19	5–16
GMAW	7–12	—	10–22	5–16

the grains to grow. The grains become coarser as they are located further away from the center of the NZ.

The grain size at different welding regions for the two FSW Al-Al joints conducted at 1750 and 2720 rpm is shown in Table 1. The relation between grain size and mechanical properties can be expressed by the following Hall-Petch equation [22]:

$$\sigma = \sigma_0 + K_h d^{-1/2}, \quad (3)$$

where σ is the strength of the material, d is the grain size diameter, σ_0 and K_h are experimental constants and are different for each metal. Equation (3) shows that smaller grain size diameter results in higher microhardness and UTS of the material. Besides, the mechanical properties not only

depend on the degree of grain refinement. And in addition, secondary phase formation, microstructure homogeneity, and microstructure defects play a vital role in deciding the mechanical properties of the weld joint.

For GMAW, the solidified weld pool and the corresponding heat affected base metal are called the welding zone (WZ) and the heat affected zone (HAZ), respectively. Partially melted zone (PMZ) in the interface of WZ and HAZ is also found in the case of some specific nonferrous alloys. The width of these zones is a direct function of the input heat and material's thermal conductivity. The cooling rate and peak temperature primarily dictate the solidification mode and phase content of the weld microstructure. The initial grain morphology is found to be columnar dendrites and develop with a different inclination to equiaxed dendritic [23].

Figure 11 shows the microstructures of (a) BM and (b) WZ and HAZ of a weld joint produced by GMAW similar to that produced by FSW. Evolution of dendritic structure in WZ is attributed to the fast heating of the weld zone up to the melting temperature and the subsequent fast cooling of the molten pool [24]. However, FSW requires much lower heat input and welding power compared to the arc welding process. Less heat input helps improve the joint mechanical properties and decreases both distortion and residual stresses [19].

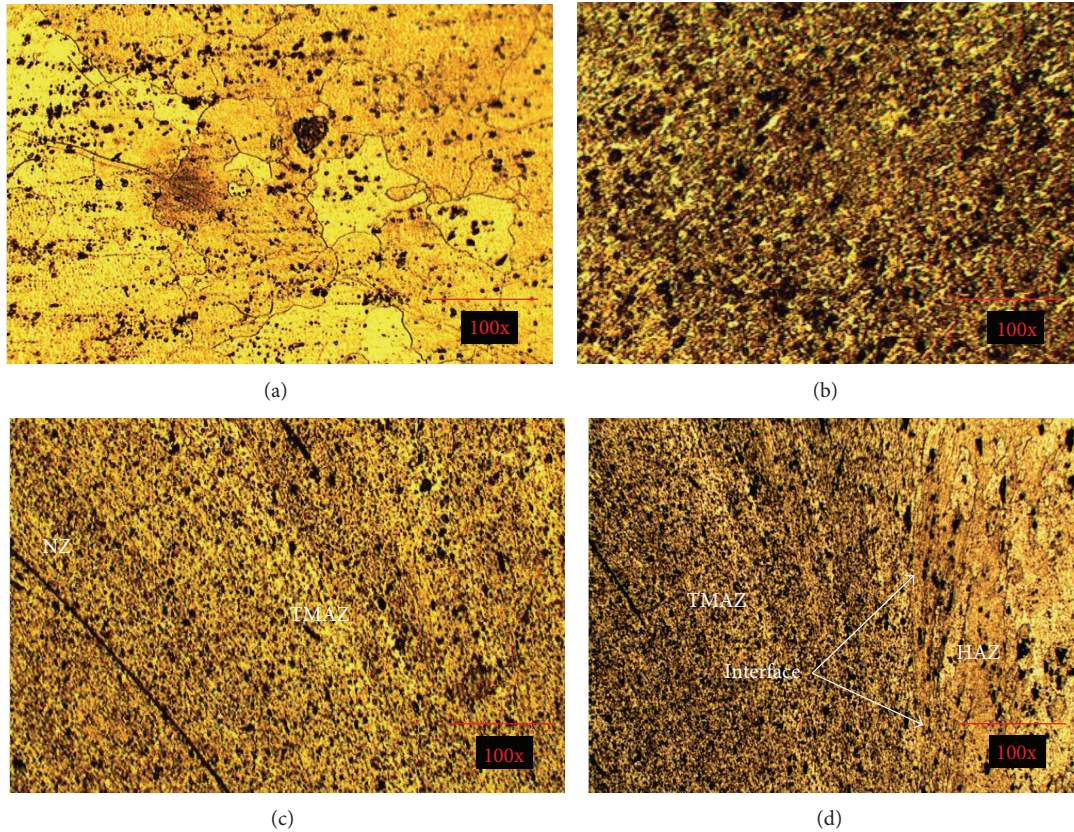


FIGURE 10: Optical images reveal the microstructures of different welding zones on Al-Al butt welded joint performed by FSW at a rotational speed of 2720 rpm. (a) BM, (b) NZ, (c) NZ and TMAZ, and (d) TMAZ and HAZ 100x magnification.

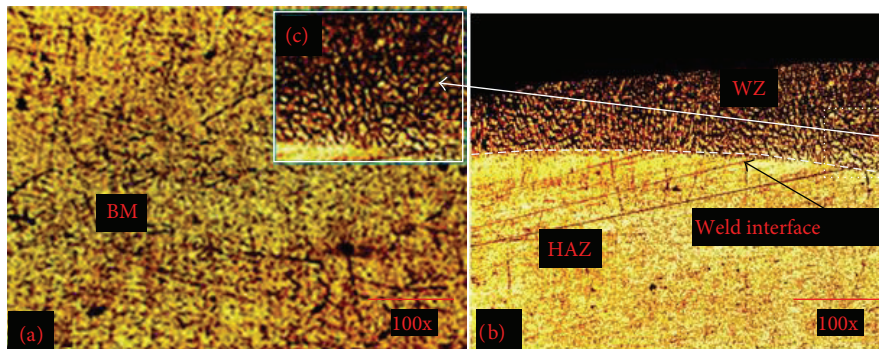


FIGURE 11: The welding morphology of the Al-Al GMAW joint depicts the microstructure of the (a) BM and (b) WZ and HAZ. The transition of grain structure from columnar dendritic to equiaxed dendritic is illustrated in the enlarged region of WZ in (c).

3.3. Environmental Effects of FSW and GMAW Techniques. Indoor Air Quality Pro device was used to detect and analyze the amount of emitted gases during the welding process. The amounts of the detected gases for both FSW and GMAW processes were compared to determine which welding technique results in the release of more harmful gases to the surroundings. The measured amount of carbon dioxide and carbon monoxide gases prior to welding and after welding is shown in Table 2. To assure reliable results, the measurements were conducted in a closed confined volume of 7.2 m^3 welding stalls.

3.4. Scanning Electron Microscopy (SEM) Analysis. Figure 12 shows an SEM image coupled with EDX scan analysis of the NZ of Al-Al FSW joint produced at a rotational speed of 2720 rpm. Weak peaks of carbon and oxygen can be seen in the EDX plot analysis; oxidization of the Al-Al welded joints at the NZ is expectable. High frictional heat generation and atmosphere humidity of 75% enhance oxidation of aluminum during the welding process. Existence of carbon in the NZ may be attributed to the contamination from the medium carbon steel tool during the welding process. Surprisingly Fe was not detected by the EDX analysis. However, its existence

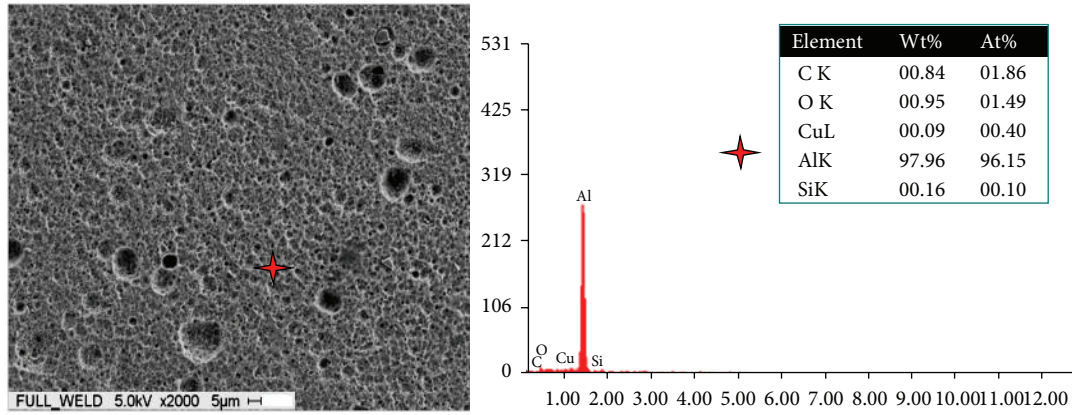


FIGURE 12: SEM image and EDX analysis of the NZ of Al-Al FSW joint performed at a rotational speed of 2720 rpm.

TABLE 2: The amounts of the released gases in the welding area prior to and after welding.

Number of tests	Atmosphere		GMAW		FSW	
	Carbon monoxide [ppm]	Carbon dioxide [ppm]	Carbon monoxide [ppm]	Carbon dioxide [ppm]	Carbon monoxide [ppm]	Carbon dioxide [ppm]
1	0.4	121	2.8	361	0.5	197
2	0.3	118	2.0	354	0.3	241
3	0.5	122	2.2	344	0.6	196
4	0.7	119	2.7	338	0.7	201
5	0.9	117	3.9	333	1.0	223

within the NZ is confirmed by the X-ray diffraction (XRD) analysis.

3.5. X-Ray Diffraction (XRD) Analysis. XRD analysis was performed on the base metal and the NZ for the two rotating speeds. The resulting superimposed diffraction patterns are displayed in Figure 13. Besides, α Al existence of different intermetallic phases at the NZ of the two rotating speeds is evident. These intermetallic phases often have complex lattice structures and microhardness values. The Al-Fe-Si ternary system is the key for Al alloy family phase formation. The formation of different Al-Fe and Al-Fe-Si intermetallic phases at different rotating speeds is attributed to the amount of heat input and the Fe content in the nugget zone. Stirring action at different rotating speeds leads to transferring of different Fe amounts from the steel tool to the welded piece and eventually results in the formation of different intermetallic phases at various temperatures. Despite the high hardness of these intermetallic phases, they have some negative effects, especially that of Al-Fe intermetallic such as $Al_{13}Fe_4$ and $AlFe_3$. The large electrochemical potential of 1.22 volts between iron and aluminum results in higher susceptibility to intercrystalline and galvanic corrosion [25].

X-ray diffraction analysis was performed also to identify the phases of the Al-Al GMAW joints. According to the XRD analysis the usage of the filler wire does not affect on the phase transformation. This may be attributed to the difference in phase formation mechanisms between FSW and GMAW processes. The XRD pattern in Figure 14 reveals that mainly pure Al phase is present.

3.6. Tensile Test. Figure 15 clearly illustrates the inferior strength of all weld joints as opposed to the UTS of the base metal. Among the three fabricated weld joint sets, the Al-Al FSW joints conducted at a speed of 2720 rpm gave the highest tensile strength. This was due to the grain refinement; homogeneous and defect-free microstructure of the joint resulted from the very intense stirring action at high rotational speed. The Al-Al FSW joints conducted at a speed of 1750 rpm have slightly inferior tensile strength as compared to that conducted at 2720 rpm speed. The tensile tests demonstrated that fractures mainly occurred at the boundary between the nugget and the TMAZ rather than along interface within the nugget itself.

The Al-Al GMAW joint possesses the low tensile strength as compared to the other fabricated weld joints. The reduction in the UTS of this weld was about 85.7%. It only possessed about 19.7% and 17.7% of the UTS of the welded joints fabricated by the FSW technique at the two rotation speeds of 1750 rpm and 2720 rpm, respectively. This high reduction in the tensile strength experienced by the GMAW joints thought to be due to the evolution of many defects during the melting and solidification process such as impurities, cracks, and pores adversely affects mechanical properties.

3.7. Microhardness Test. Figure 16 depicted that the microhardness at the NZ, TMAZ, and HAZ for the FSW Al-Al joints is lower than the microhardness of the BM. This is attributed to the effects of thermal exposure and mechanical action which lead to different levels of dynamic recrystallization, grain growth, and phase transformation at the different

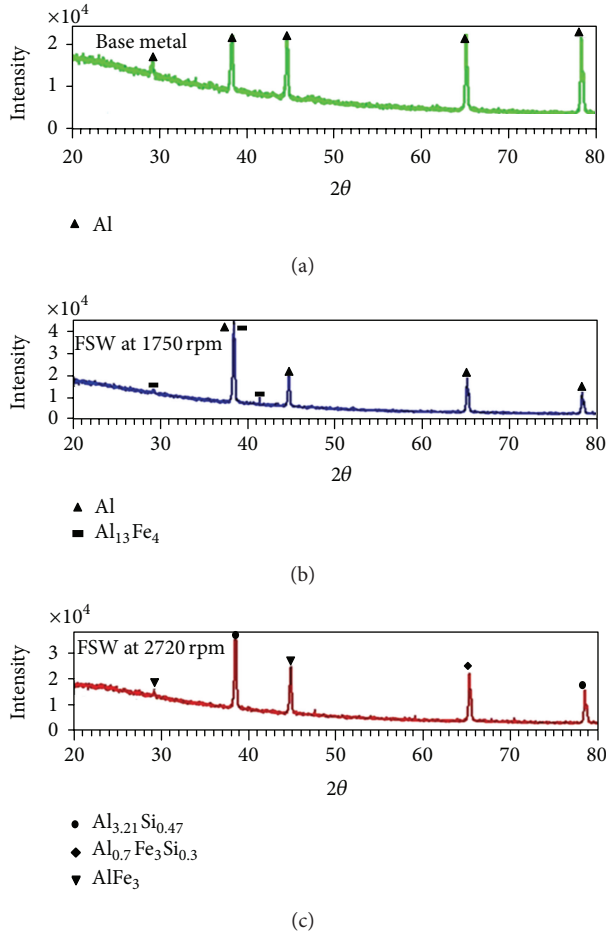


FIGURE 13: X-ray superimposed diffraction patterns of the Al-Al FSW joint. (a) BM and (b) NZ at rotating speed of 1750 rpm and (c) NZ at rotating speed of 2720 rpm.

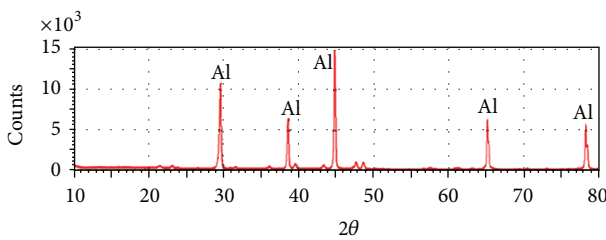


FIGURE 14: X-ray diffraction pattern of the Al-Al GMAW joint. Mainly peaks of pure α Al are eminent.

welding zones. Recrystallization occurs when new grains form and consume the original cold-worked grains. The higher microhardness and strength of the BM are ascribed to the cold working gained during the production stages of casting, rolling, and forming. Cold working enhances microhardness and strength. It causes dislocations to be entangled with one another and hinders their motion [26].

The NZ showed the highest microhardness values as compared to other weld zones. HAZ showed the lowest hardness values. In fact, this is understandable. The HAZ is

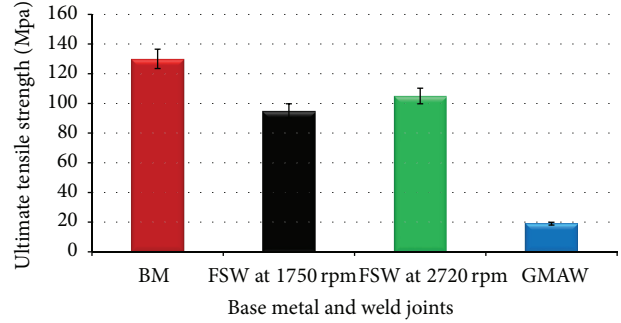


FIGURE 15: The UTS of the base metal and the weld joints produced by the FSW and the GMAW techniques.

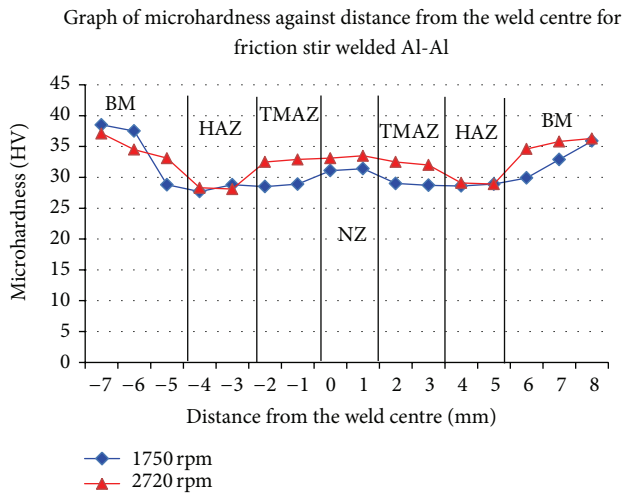


FIGURE 16: The microhardness profiles of Al-Al joints fabricated by FSW.

far away from the stirring action influence. This justifies why the microhardness values of the HAZ at the two rotational speeds were almost identical.

Figure 17 exhibits the microhardness profile for the Al-Al GMAW joints. Again the microhardness values of the weld zones are much lower than that of the BM. The elongated dendritic and the equiaxed grain structure with the WZ result in the fast heating and subsequent fast cooling of the molten pool. The bulk volume of the workpiece acts as an efficient sink for the heat generated during welding and results in different cooling rates at the HAZ and the WZ [27]. The heat flow gradient affects the mechanical properties of the joint. The HAZ demonstrated lower hardness than that of the WZ specifically near the weld interface. The weld interface is a narrow boundary that separates the WZ and the HAZ. It consists of a thin band of the BM that has melted or partially melted during the welding process but has immediately solidified before any mixing could take place.

4. Conclusions

(1) In this study FSW technique showed outstanding advantages over the GMAW process in joining 1030 Al alloys. It gave

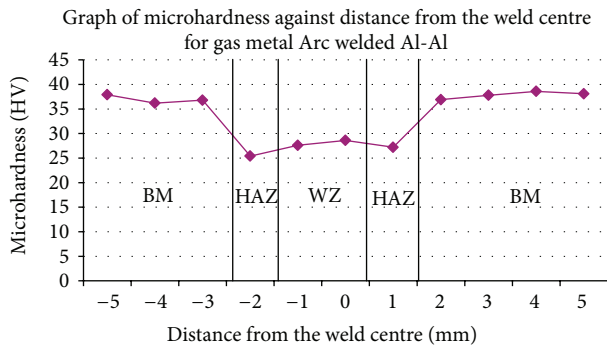


FIGURE 17: The microhardness profiles of Al-Al joint fabricated by GMAW.

clean, defect-free, and better weldment microstructure which in turn resulted in superior mechanical properties.

(2) FSW showed a substantial saving in power consumption. The power consumed in GMAW was fourfold that of FSW for execution of similar joints. This resulted in a reduction in the area where microhardness changes. The HAZ in FSW was narrower than that in GMAW process.

(3) GMAW process released higher amounts of harmful gases such as carbon monoxide and carbon dioxide to the surroundings (2.7 ppm and 346 ppm, resp.) as opposed to 0.6 ppm and 211.6 ppm, respectively, for FSW.

(4) The joints welded by GMAW process exhibited substantial reduction in their UTS and microhardness values, 80% and 12%, respectively, as opposed to FSW joints executed at rotation speed of 2720 rpm, 78% and 9.5%, respectively, as opposed to FSW joints executed at 1750 rpm.

Conflict of Interests

The authors declare that there is no conflict of interests regarding the publication of this paper.

Acknowledgments

This work is supported under the Grant no. 9001-00338 of the Universiti Malaysia Perlis (UniMAP). The authors gratefully acknowledge the outstanding support provided by the technicians of the workshop in the Materials Engineering School, UniMAP.

References

- [1] R. K. Shukla and P. K. Shah, "Comparative study of friction stir welding and tungsten inert gas welding process," *Indian Journal of Science and Technology*, vol. 3, no. 6, pp. 667–671, 2010.
- [2] E. D. Nicholas, "Friction stir welding—a decade on," in *Proceedings of the IIW Asian Pacific International Congress*, Sydney, Australia, October–November 2000.
- [3] O. Vladvoj, S. Margarita, F. D. S. Jorge, and V. Pedro, "Microstructure and properties of friction stir welded aluminium alloys," in *Paper Presented at Metal*, Hradec nad Moravicí, Czech Republic, 2005.

- [4] A. V. Kumar and K. Balachandar, "Effect of welding parameters on metallurgical properties of friction stir welded aluminium alloy 6063-O," *Journal of Applied Sciences*, vol. 12, no. 12, pp. 1255–1264, 2012.
- [5] W. H. Jiang and R. Kovacevic, "Feasibility study of friction stir welding of 6061-T6 aluminium alloy with AISI 1018 steel," *Proceedings of the Institution of Mechanical Engineers B: Journal of Engineering Manufacture*, vol. 218, no. 10, pp. 1323–1331, 2004.
- [6] G. G. Roy, R. Nandan, and T. DebRoy, "Dimensionless correlation to estimate peak temperature during friction stir welding," *Science and Technology of Welding & Joining*, vol. 11, no. 5, pp. 606–608, 2006.
- [7] T. Hirata, T. Oguri, H. Hagino et al., "Influence of friction stir welding parameters on grain size and formability in 5083 aluminum alloy," *Materials Science and Engineering A*, vol. 456, no. 1, pp. 344–349, 2007.
- [8] J. N. Pires, A. Loureiro, and G. Bölmsjö, *Welding Robots*, Springer, London, UK, 2006.
- [9] R. W. Messler, *Principles of Welding: Processes, Physics, Chemistry, and Metallurgy*, John Wiley & Sons, New York, NY, USA, 2008.
- [10] S. Kou, *Welding Metallurgy*, Wiley-Interscience, Hoboken, NJ, USA, 2nd edition, 2003.
- [11] M. Esmaily, S. N. Mortazavi, P. Todehfalah, and M. Rashidi, "Microstructural characterization and formation of α martensite phase in Ti-6Al-4V alloy butt joints produced by friction stir and gas tungsten arc welding processes," *Materials and Design*, vol. 47, pp. 143–150, 2013.
- [12] P. B. Anjaneya and P. Prasanna, "Experimental comparison of the MIG and friction stir welding processes for AA 6061(Al Mg Si Cu) aluminium alloy," *International Journal of Mining, Metallurgy & Mechanical Engineering*, vol. 1, no. 2, pp. 137–140, 2013.
- [13] ASTM Standard E3, "Standard Guide for Preparation of Metallographic Specimens".
- [14] ASTM Standard E407, "Standard Practice for Microetching Metals and Alloys".
- [15] ASTM Standard E8, "Standard Test Methods for Tension Testing of Metallic Materials".
- [16] ASTM Standard E384, "Standard Test Method for Knoop and Vickers Hardness of Materials".
- [17] P. Bahemmat, A. Rahbari, M. Haghpanahi, and M. K. Besharati, "Experimental study on the effect of rotational speed and tool pin profile on AA2024 aluminum friction stir welded butt joints," pp. 1.1–1.7, Proceedings of the ASME Early Career Technical Conference (ECTC '08), Miami, Fla, USA, October 2008.
- [18] C. Meran, "The joint properties of brass plates by friction stir welding," *Materials & Design*, vol. 27, no. 9, pp. 719–726, 2006.
- [19] S. R. McLaughlin, C. J. Bayley, and N. M. Aucoin, "Assessment of microstructural heterogeneities in multipass pulsed gas metal arc welds," *Canadian Metallurgical Quarterly*, vol. 51, no. 3, pp. 294–301, 2012.
- [20] M. W. Mahoney, C. G. Rhodes, J. G. Flintoff, W. H. Bingel, and R. A. Spurling, "Properties of friction-stir-welded 7075 T651 aluminum," *Metallurgical and Materials Transactions A*, vol. 29, no. 7, pp. 1955–1964, 1998.
- [21] G. Liu, L. E. Murr, C.-S. Niou, J. C. McClure, and F. R. Vega, "Microstructural aspects of the friction-stir welding of 6061-T6 aluminum," *Scripta Materialia*, vol. 37, no. 3, pp. 355–361, 1997.

- [22] J. W. Dini, *Electrodeposition: The Materials Science of Coatings and Substrates*, Noyes Publications, Park Ridge, NJ, USA, 1993.
- [23] P. Kamal and K. P. Surjya, "Effect of pulse parameters on weld quality in pulsed gas metal arc welding: a review," *Journal of Materials Engineering and Performance*, vol. 20, no. 6, pp. 918–931, 2011.
- [24] Y. Liu, W. Wang, J. Xie et al., "Microstructure and mechanical properties of aluminum 5083 weldments by gas tungsten arc and gas metal arc welding," *Materials Science and Engineering A*, vol. 549, pp. 7–13, 2012.
- [25] P. B. Srinivasan, K. S. Arora, W. Dietzel, S. Pandey, and M. K. Schaper, "Characterisation of microstructure, mechanical properties and corrosion behaviour of an AA2219 friction stir weldment," *Journal of Alloys and Compounds*, vol. 492, no. 1-2, pp. 631–637, 2010.
- [26] H. J. McQueen, "Recovery and recrystallization during high temperature deformation," *Treatise on Materials Science & Technology*, vol. 6, pp. 393–493, 1975.
- [27] A. K. Lakshminarayanan, V. Balasubramanian, and K. Elangovan, "Effect of welding processes on tensile properties of AA6061 aluminium alloy joints," *The International Journal of Advanced Manufacturing Technology*, vol. 40, no. 3-4, pp. 286–296, 2009.

Review Article

Friction Welding of Aluminium and Aluminium Alloys with Steel

Andrzej Ambroziak, Marcin Korzeniowski, Paweł Kustroń, Marcin Winnicki, Paweł Sokołowski, and Ewa Harapińska

Welding Technology Department, Institute of Production Engineering and Automation, Wrocław University of Technology, 50-370 Wrocław, Poland

Correspondence should be addressed to Andrzej Ambroziak; andrzej.ambroziak@pwr.wroc.pl

Received 10 December 2013; Revised 12 February 2014; Accepted 11 March 2014; Published 28 April 2014

Academic Editor: Achilles Vairis

Copyright © 2014 Andrzej Ambroziak et al. This is an open access article distributed under the Creative Commons Attribution License, which permits unrestricted use, distribution, and reproduction in any medium, provided the original work is properly cited.

The paper presents our actual knowledge and experience in joining dissimilar materials with the use of friction welding method. The joints of aluminium and aluminium alloys with the different types of steel were studied. The structural effects occurring during the welding process were described. The mechanical properties using, for example, (i) microhardness measurements, (ii) tensile tests, (iii) bending tests, and (iv) shearing tests were determined. In order to obtain high-quality joints the influence of different configurations of the process such as (i) changing the geometry of bonding surface, (ii) using the interlayer, or (iii) heat treatment was analyzed. Finally, the issues related to the selection of optimal parameters of friction welding process were also investigated.

1. Introduction

The family of friction welding processes includes several methods, such as rotary friction welding (RFW), linear friction welding (LFW), and the newest one, friction stir welding (FSW). However, the main principle is always the same—to obtain the joint it is necessary to heat the materials to the plastic-state and with the use of “upsetting force” plastically displace the materials and create the weld. The heat is generated by the friction between two welded components (RFW and LFW) or between components and specially designed tool (FSW). Welding processes are classified as solid-state joining methods because the melting of joined materials does not occur these processes [1–3].

A big attractiveness of these joining methods results from many technical and economic advantages, such as high efficiency and stability of the process or better conditions of occupational safety and health than in the case of traditional welding technologies. However, recently, the most important seems to be the possibility of joining materials with different properties. Due to the fact that in the fusion zone between the two different materials the intermetallic compounds are formed and the joining process of dissimilar materials is

often very difficult. To obtain high-quality joint it is necessary to know and analyze phase diagram of the two welded materials. Furthermore, the microstructure and different properties of intermetallic phases, such as crack sensitivity, ductility, and corrosion resistance, are also very important. There are some additional factors, for example, coefficients of thermal expansion of welded materials and their melting temperatures, the knowledge of which is also necessary in the case of joining dissimilar materials [3–6].

The presented review summarizes our actual knowledge about the friction welding of aluminium and aluminium alloys with different types of steel. This paper describes both authors' research as well as many other studies of scientists dealing with the presented subject.

2. Results and Discussion

2.1. Aluminium-Steel. Joining with the welding methods of the pairs of materials, such as aluminium alloys-steel, still brings many problems. Even the analysis of the aluminium-iron dual system leads to the conclusion that sufficiently long time and high temperatures of the process can cause

the formation of intermetallic phases and can be the reason for brittleness of joints (Figure 1). In the case of welding steel to aluminium, the excessively fragile intermetallic compounds lead to the joint degradation. In the Al-Fe equilibrium system, there is no solubility in a solid phase. Therefore, when using the friction welding the intermetallic phases are formed, despite joining in the solid state. The main component of intermetallic phases, which were created at the border of the steel-aluminium joint, is an Al_3Fe [7]. When joining pure aluminium with stainless steel, Sundaresan and Murti have reported that the compounds of Fe_2Al_5 and FeAl_3 had been formed on the joint's surface [8]. Fukumoto et al. [9] have observed that not only compounds of Fe_2Al_5 and FeAl_3 had been formed on the welding surface, but also the FeAl phase. Seli and coauthors [10] have tried to model the heat distribution during the friction welding of aluminium and structural steel and connect it with the formation of intermetallic phases.

Jessop et al. [11] have shown that in the aluminium-austenitic steel joints, the intermetallic phases were formed on the joints' boundary. The intermetallic phases had width of $3.0\ \mu\text{m}$ and were unevenly distributed over the diameter of the friction surface. Jessop has observed that the highest thickness of the intermetallic phases was present on the surface, in the distance of about half radius from the axis of the sample. The researches on the shear energy of the joints have determined its dependence on the thickness of the intermetallic phases. Therefore, when the thickness of the intermetallic phases was $0.2\text{--}1.0\ \mu\text{m}$, the shear energy was the highest (about 600 J). When the thickness was lower than $0.2\ \mu\text{m}$ or was higher than $2\ \mu\text{m}$, the shear energy decreased to about 400 J. The author stated that lack of the intermetallic phases probably indicated the unstable joining process, and too high thickness of the fragile intermetallic phases caused the reduction of the shear energy value.

Elliott and Wallach [16] and authors of the elaboration [7, 17] have come to similar conclusions. Their researches confirmed that the thickness of the intermetallic phases depends on the friction time and rotational speed, and the highest tensile strength was obtained for a layer's thickness of $1\text{--}2\ \mu\text{m}$.

Yilbaş et al. [17] have carried out the researches that concern the friction welding of aluminium and steel. For testing, they have used nonalloy carbon steel with a five times higher tensile strength than the tensile strength of aluminium. They have used three different rotational speeds: 2000, 2500, and $2800\ \text{min}^{-1}$, at various parameters of the friction pressure and friction time (4, 7, and 10 s), similarly as in the research on steel-copper joints. The occurrence of intermetallic phases on the joint's bound has been observed. The researchers concluded that for a good joint, an intermetallic layer, which was generally in the half radius length, with the thickness of $0.1\text{--}1\ \mu\text{m}$ was acceptable. On the edges, this layer has occurred in minor amounts, while in the middle of the joint it did not occur at all, which was related to the lowest rotational speed in this area. In the joint at the steel side, the hardness has been reduced to 50 HV, in the heat affected zone, at a length of 1.5 mm from the welding surface. The width of the heat affected zone was very small, compared to welding of other

materials. The highest stated value of the tensile strength for rotational speed was $2800\ \text{min}^{-1}$ (Figure 2).

The author's own investigations [18], concerning the direct friction welding of aluminium and X10CrNiTi189 steel at process parameters in accordance with Table 1 (parameter no. 1), have shown some satisfactory strength and plastic properties of the investigated joints (Figure 3). The tensile strength has reached 107 MPa, and the breaking has occurred at the aluminium side, at high distance from the bonding zone. During the bending test, the bending angles of over 120° have been obtained. Simultaneously, the entire deformation has occurred at the aluminium side (Figure 3(b)). The achieved results have been repeatable, even at two times' lower rotational speed (Table 1). To prevent the formation of intermetallic phases, shorter friction time (0.5 s) and high pressure during the upsetting phase (134–259 MPa) have been used. However, they have resulted in significant length reduction of the welded elements (28.7 mm).

2.2. Aluminium Alloys-Austenitic Steel. The results, discussed in the previous chapter, showed that joining of pure aluminium and steel, by friction welding, was possible. In the technique, especially in marine, aviation, and refrigeration industries, the joints of aluminium alloys and chromium-nickel austenitic steel are applicable. The aluminium alloys with magnesium, especially the AlMg3 alloy, are commonly used in industries, where the higher strength properties (comparing to aluminium) are necessary. The alloying additions, which are present in aluminium alloys (especially magnesium), usually aggravate the metallurgical conditions of aluminium bonding [19]. They cause acceleration of the formation of the intermetallic phases at the joint's bound [20], because of the increase of the diffusion coefficient. Compared to aluminium, magnesium is characterized by a higher diffusion coefficient and has significantly lower solubility in iron. For these reasons, on the welding surface of aluminium alloys that include magnesium, the intensive heterodiffusion and reaction-diffusion processes take place and cause the formation of the intermetallic phases.

In the elaboration [21] it was stated that the Fe_2Al_5 phase leached while bonding the A6061 aluminium alloy with AISI 304 stainless steel, during the friction welding process, at the contact surface. However, at the surface of bonding pure aluminium and carbon steel, the compounds of $\text{Fe}_4\text{Al}_{13}$ and Fe_2Al_5 [9, 22] have been observed.

Fukumoto et al. in [23, 24], when analysing with a transmission microscope (TEM) the intermetallic phases that occurred at the boundary of austenitic steel (type 304)-aluminium alloy series 5052 joints, have reported a formation of amorphous layers in the solid state at high temperatures.

In the dissertation [25], the weldability of various aluminium alloys (series 1050, 2011, 5052, 5056, and 6061 i 7075) and S25C unalloyed carbon steel (0.26% C) have been investigated. For this purpose different process parameters have been used: friction time of 1–4 s, friction phase pressure of 10–30 MPa, and upsetting phase pressure of 10–80 MPa. An identification of phases, which had been formed on the contact surface of the materials, has been carried out,

TABLE 1: The parameters of friction welding and strength properties of joints of dissimilar materials (aluminium and aluminium alloys with steel or titanium).

No. Welded materials	Rotational speed [min ⁻¹]	Friction pressure (shortening speed) P_{f1}/P_{f2} [MPa] ($v_{R1}, \text{mm s}^{-1}$)	Friction time t_{f1}/t_{f2} [s]	Upsetting pressure P_s [MPa]	Shortening s_1/s_2 [mm]	Tensile strength R_m [MPa]	Bending angle (toughness) $[\text{°}]$ (J cm^{-2})	Comments	Literature
1 Austenitic steel-aluminium	1300	4	1.5	23	3.4				[11]
	1500	75	0.5	134/259	4.5/28.7	107		MR (Al)	incl.
	710	26/77	1.5/0.2	235	3.8/39	78	Over 120	MR (Al)	incl.
2 Austenitic steel-Al 0.5 Si 0.5 Mg alloy	1500	52/94	1.5/0.2	235	7.2/25.1	210	75		incl.
	1300	9.0	1.0	25	4.0			Tapered surface of steel	[11]
	1500	(1.0)	4.3	100	14.6	160	52		[12]
3 Austenitic steel-AlMg3 alloy	1500	(1.0)	4.8	85	8.1	113	1.5		[12]
	1500	69/92	2/0.2	120	13.0	197	1.3		[12]
	710	85/96	1/0.3	300	1.6/20.5	207	7		[13]
4 Austenitic steel/aluminium-AlMg3 alloy*	1500	43/120	4/0.5	239	1.2/13.7	207	11		[13]
	710	83	2.4/1.2	256	15/23	197	13		[13]
	710	38	2.4/60	256	0.8/17	9	9		[13]
5 AlCuMgNi-42CrMo4	1500	24/28	3/0.3	81	1.6/14.1	185	0		[13]
	720	104/121	1.0/0.2	300	0.6/4	98		Al-35 mm	[14]
	1500	107/124	1.0/0.2	200	0.5/2.9	102		Al-25 mm	[14]
6 42CrMo4-nickel	720	41/96	4.0/0.9	160	3.5/4.2	114		Al-8 mm	[14]
	1500	41/96	4.0/0.85	160	5.6/7.4	54		Al-3 mm	[14]
	720	41/96	4.0/0.85	160	5.6/7.4	54		Scratches on the surface	[14]
7 AlCuMgNi*	720 (D1)	41/93	4.0/0.9	161	3.2/4.1	198			[14]
	720 (D2)	41/90	4.0/0.85	161	3.4/4.6	0			[14]
	1500	24/55	2.0/18.35	81	1.1/2.0	0			[14]
8 AlMg3-titanium	1500	41/92	4.0/0.9	161	4.4/5.1	211			[14]
	1500	41/103	4.0/0.85	200	6.8/9.8	235			[14]
	1500	41/122	4.0/0.9	242	9.7/13.6	265			[14]
9 Al-AlMg3	1500	41/114	4.0/0.9	223	5.9/9.5	272			[14]
	1500	69/91	2.4/0.2	200	3.2/11.6	205.4	120		[13]
	1500	24	3.03	80	2.4/18.1	72	120	MR Al	[13]
10 AlMgSi0.5-AlMg3	1500	52/94	1.5/0.2	235	7.2/25.1	210	75		incl.
	1500	35/40	3/0.3	120/134	3.2/17.6	210	120		incl.
	1500	35/40	3/0.3	120/134	3.2/17.6	210	120		incl.

Upsetting time (t_{s1}, t_{s2}) = 10 s

D—joints additionally subjected to diffusion welding at parameters: 1—5000°C, 2 min, and pressure 5 MPa; 2—550°C, 40 min, and pressure 5 MPa; R—nickel surface with high roughness parameters; W—joint subjected to heat treatment (680°C, 1 h, vacuum oven); incl.—own investigations; MR (Al)—during the tensile test the breaking of the specimen has occurred at the aluminium side; *—3-I welding, where “/” means first welded material and “-” means second welded material.

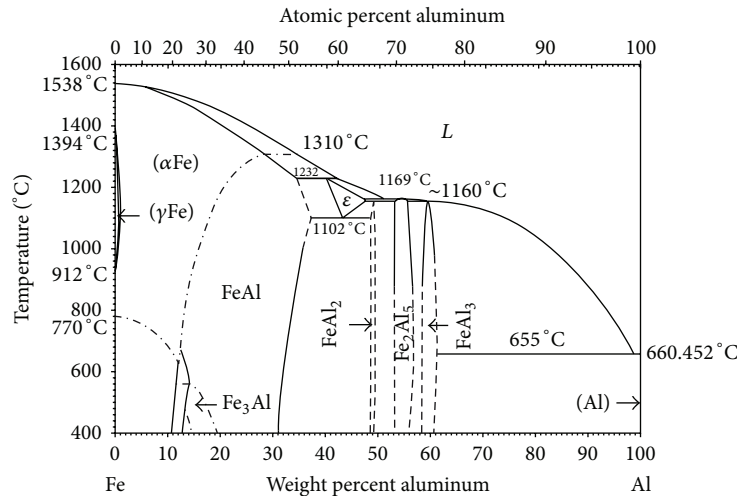


FIGURE 1: Equilibrium diagram for the aluminium-iron system (according to [15]).

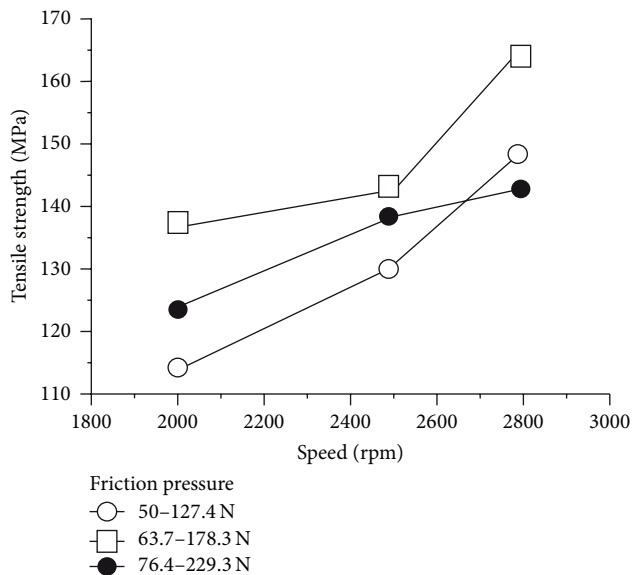


FIGURE 2: Strength properties of the steel-aluminium joint, welded at various parameters (according to [17]).

and the quality of joints has been evaluated on the base of the static tensile test. It has been stated that the joint was characterized by efficient tensile strength, if the width of the diffusion zone (with intermetallic phases) was $0.2\text{--}1\ \mu\text{m}$. For certain joints, a strength of more than 90% of the strength of the aluminium alloy (for the following alloys: 1052, 6061, and 6063), 50% (for 5056 alloys) to 26% for 2011 alloys, and 24% for 2024 alloys has been achieved. Higher strength values have been stated for the joints of bars, in comparison to tubular joints.

Extensive researches on the friction welding of the A 6061-T6 aluminium alloy with six types of steel, for example, unalloyed steel, toughening steel, and austenitic steel, have been presented by Ochi et al. [7]. The quality of the joints

has been evaluated on the base of static tensile test and microhardness measurements. An increase of the joints' strength, together with an increase of the pressure in the friction phase and the shortening (welding time had been controlled with the shortening length), has been stated. The highest strength parameters have reached 280 MPa, when the friction pressure has reached 240 MPa, and the shortening has been about 16 mm.

The friction welding of aluminium alloys with austenitic steel has been a subject of many elaborations, including the author's one. In most of the publications concerning the welding of steel and aluminium, and its alloys, the test on joints' ductility was usually omitted. The ductility may be evaluated using the technological bending test. Only NA [12] noted the results for the joints investigated in his PhD dissertation (Table 1).

The issue of plastic properties of friction welded joints of austenitic steel and aluminium alloys, illustrated with an example of AlMgSi0.5 and AlMg3, has been considered in the author's dissertations [13, 14, 26].

2.2.1. AlMgSi0.5-Austenitic Steel. The friction welded AlMgSi0.5-X10CrNiTi189 austenitic steel joint, in comparison to the steel-pure aluminium joint, was characterized by higher parameters of tensile strength (about 210 MPa), but in technological bending test the achieved bending angle has reached about 75° (Figure 4).

Thanks to the microscopic observation it has been possible to find a very narrow diffusion layer on the joint's surface, with a thickness of about $1\ \mu\text{m}$ (Figure 5). Other authors have also shown similar results of the tests of joints' strength [18]. However, their values have been lower, probably due to the lower pressure used during the upsetting phase (Table 1).

2.2.2. AlMg3-Austenitic Steel. Until now, it has not been possible to obtain any welded joints of chromium-nickel austenitic steel with AlMg3 aluminium alloy, with sufficient plastic properties for direct joining. The author has been

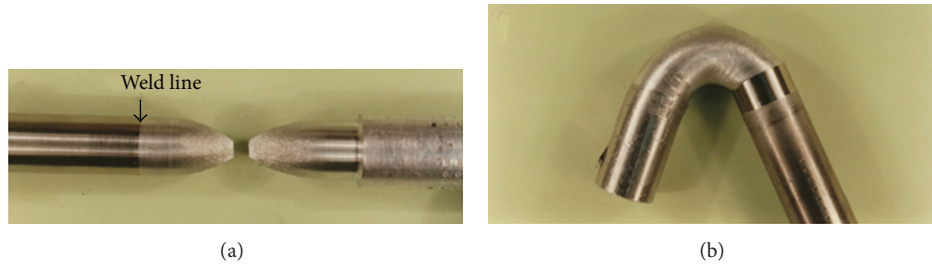


FIGURE 3: View of friction welded joints of 99.8 aluminium-X10CrNiTi189 austenitic steel, after the static tensile test (a) and the technological bending test (b).

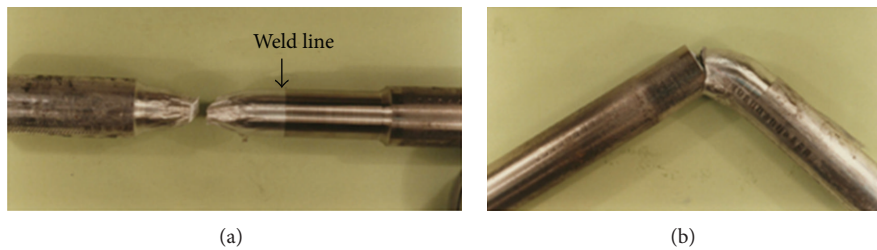


FIGURE 4: View of friction welded joints of AlMgSi0.5 aluminium alloy-X10CrNiTi189 austenitic steel, after the static tensile test (a) and the technological bending test (b).

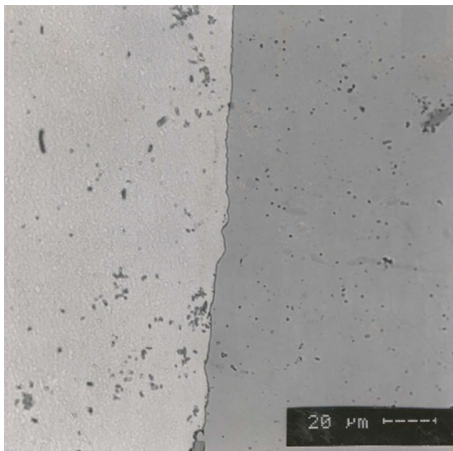


FIGURE 5: The microstructure in the bonding zone of the friction welded AlMgSi0.5 aluminium alloy-X10CrNiTi189 austenitic steel joint (according to [13]).

conducting some intensive researches on the friction welding of such joints, partly presented in [13].

The friction welded joints of AlMg3-X10CrNiTi189 steel with diameter of 30 mm had high tensile strength (about 207 MPa), and the fracture occurred in the base material of AlMg3 alloy (Figure 6(a)). However, in the technological bending tests, bending angles within few degrees have been achieved, with a small dependence on the diameter of the bending mandrel.

The metallographic researches have shown the appearance of the diffusion zone with diameter of 1–6 μm , depending on the welding parameters. Despite the short time

of the welding process and the high pressure during the upsetting (sample no. 3; Table 1), it has not been possible to fully remove the intermetallic phases from the joint's surface. For the research purposes, a friction welding for a pair of AlMg3 aluminium alloy-X10CrNiTi189 austenitic steel has been conducted, at high welding time (about 62 s). In such joint a wide (about 8 μm) diffusion zone, with microhardness reaching up to 1800 HV 0.005, has appeared (Figure 7(a)). On the steel side, the microhardness has been equal to 83 HV 0.005, and at the intermetallic phases layer it has reached 348 HV 0.005. Therefore, at the aluminium alloy side, in a zone adjacent to the intermetallic phases, the increase of microhardness (up to 65 HV 0.005) has been reported (microhardness of base material is 58 HV 0.005). The technological bending test of such joint has ended with an immediate crack which has passed the intermetallic layers (Figure 7(b)).

At short welding time ($t_t = 3.6\text{ s}$) the width of the intermetallic phases has reached 1–2 μm , but the bending angle has been about 10°. Several attempts to eliminate the intermetallic phases by changing the geometry of bond's surface have been taken (Figure 8).

Figure 9 presents the microstructure of the bonding zone of the friction welded AlMg3 aluminium alloy-X10CrNiTi189 austenitic steel joint, together with a microhardness measurement. The front surface of the steel sample has been prepared with a rough turning (roughness of $R_z = 150\ \mu\text{m}$). In Figure 9(a), on the aluminium alloy side, there was a zone with a diameter of 500 μm , without any microinclusions, and with an increased microhardness, up to 74 HV 0.015 (base material: 64 HV 0.015). On the boundary of the joint, there was a narrow (about 1 μm) diffusion zone. The static tensile test has caused a fracture of a sample, on the contact surface,

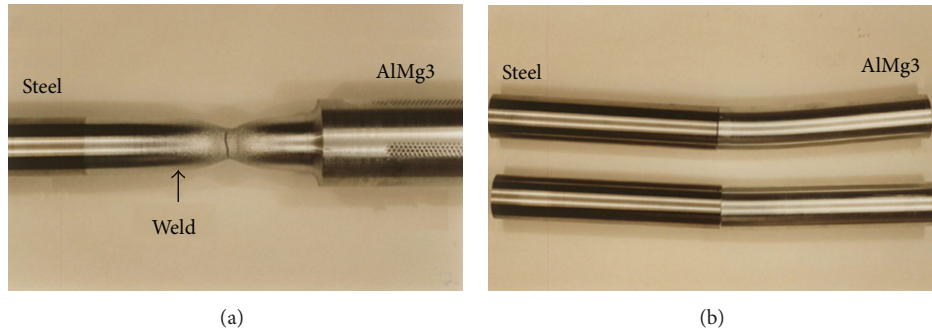


FIGURE 6: View of friction welded joints of AlMg3 aluminium alloy-X10CrNiTi189 austenitic steel, after the static tensile test (a) and the technological bending test with a bending mandrel with diameter of 20 mm and 100 mm (b).

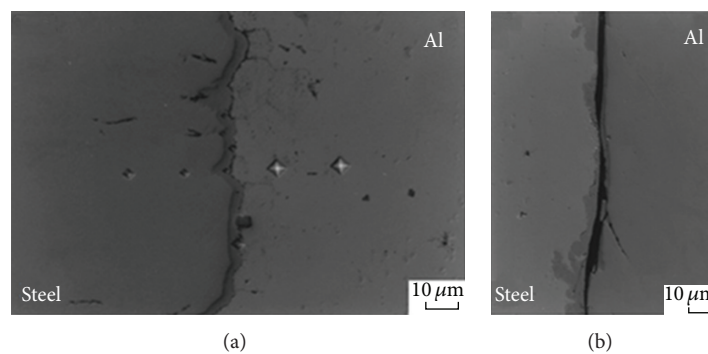


FIGURE 7: The microstructure in the bonding zone of the friction welded AlMg3 aluminium alloy-X10CrNiTi189 austenitic steel, together with a measurement of microhardness (a) and a bending test (b).

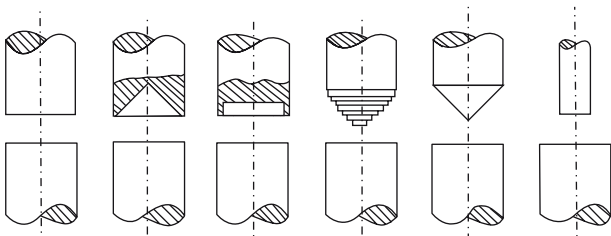


FIGURE 8: The scheme of the shapes of the friction welded AlMg3 aluminium alloy-X10CrNiTi189 austenitic steel joints' surfaces, used in the investigations [13].

with strength of 197 MPa, and the bending angle has been equal to 13° .

Further attempts, including those with the tapered surface of the steel sample (Figure 10), have not caused the elimination of the zones with intermetallic phases on the joint's bound. Maximum bending angles have reached 35° for a conical shape of the joint.

In Figure 11, a macrostructure and microstructure of the friction welded AlMg3 aluminium alloy, with a diameter of 60 mm, and X10CrNiTi189 austenitic steel, with a diameter of 30 mm and a substantial roughness of the contact surface on the steel side, are shown. There was a visible flow disruption

of AlMg3 material alloy, as a result of macroroughness (Figure 11(a)).

Many attempts have been taken, to form the top surface of steel in the pipe joints with a diameter of 50 mm. Their forming has influenced the various forms of the flash but has not caused an elimination of the intermetallic phases, on the surface of the materials being bonded (Figure 12).

To investigate the influence of the parameters of the friction welding process on the shearing work some researches have been conducted [26]. The joints of AlMg3 aluminium alloy-X10CrNiTi189 austenitic steel (in a shape of bars with 30 mm diameter) have been formed using three different friction welding parameters carefully selected to ensure various mechanical properties of the joints. It means that there have been attempts to form the joints with various intermetallic phases' thicknesses. So well, the friction time and methods of preparing the steel samples' surfaces have been differentiated. The joints, analysed in the researches, have been formed with friction times of 1.3 s and 4.5 s (sample no. 3; Table 1). Due to that, various thicknesses of the layers with intermetallic phases have been obtained, as it can be seen in Figure 13. The top surface of the steel samples has been formed with accurate (sample no. 3: $t_f = 1.3$ s; $R_z = 24 \mu\text{m}$) and rough turning (sample no. 3: $t_f = 4.5$ s; $R_z = 152 \mu\text{m}$).

While for joints, which have been friction welded with low friction time, there was a continuous narrow diffusion

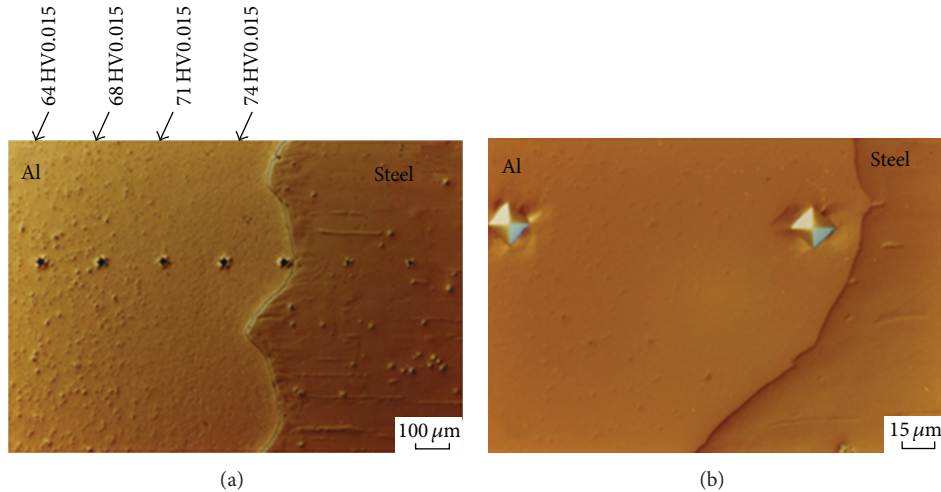


FIGURE 9: The microstructure in the bonding zone of the friction welded AlMg3 aluminium alloy-X10CrNiTi189 austenitic steel (steel sample with a rough surface of $R_z = 150 \mu\text{m}$) (a) and an enlarged fragment of the microstructure from Figure 9(a) (b).

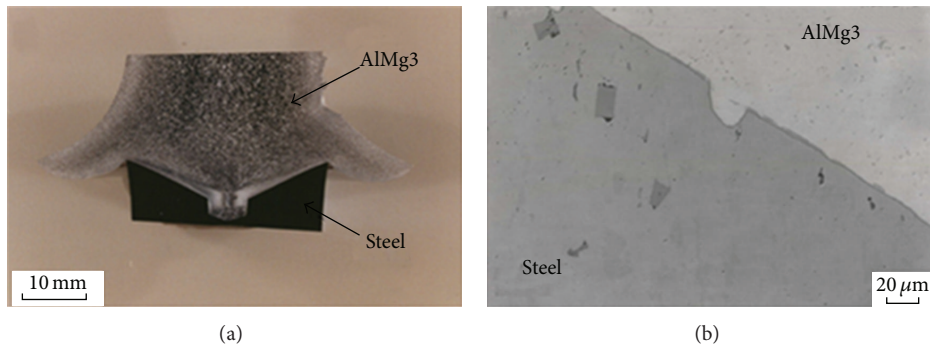


FIGURE 10: The macrostructure of the friction welded AlMg3 aluminium alloy-X10CrNiTi189 austenitic steel joint, with a diameter of 30 mm and a conical shape of the joint (a) and the microstructure of such joint (b).

zone with a diameter of few micrometers (Figure 13(a)); the joints formed at longer friction time were characterized by local thickening of the diffusion layer and discontinuities on the aluminium side (Figures 13(b) and 13(c)).

The results of the maximum loading force, obtained in the shearing test for the investigated joints, are shown in Figure 14, whereas, in Figure 15, the results of shearing work, calculated for two variants of shearing patterns, $F_{t\max}$ and F_1 , are shown. The samples after the shearing test are presented in Figure 16. In the cross-section, depending on the welding parameters, a precipitate of aluminium on the steel side with the amount from 0 to 100% of the sample's surface, depending on the welding parameters, was visible.

From the previous researches [27, 28] it was known that during the friction welding of steel, including austenitic steel with aluminium alloys (with over 2% of magnesium), the formation of hard and fragile intermetallic phases of $\text{Al}_{13}\text{Fe}_4$ type has occurred. Their formation has depended on the diffusion processes that were accelerated by magnesium and their thickness has depended on the welding parameters (especially on the friction time). The joints, analysed in the researches, have been formed with two different friction

time parameters, so various thicknesses of the layers with intermetallic phases have occurred. So, for joints that have been friction welded with low friction time, there was a continuous narrow diffusion zone with a diameter of few micrometers (Figure 13(a)) and the joints formed at longer friction time were characterized by local thickening of the diffusion layer and discontinuities on the aluminium side (Figures 13(b) and 13(c)). However, the shearing test has proven a difference of about 5%, for the maximum shearing force between the joints formed with the investigated welding parameters (Figure 14). Wherein, the highest values (average of 107.8 kN) have been stated for the samples welded at low friction phase time, and the lowest (102.2 kN) values have been obtained for the samples welded at high friction phase time. Therefore, the measurements of the shearing work, carried out for various stages of the test, have shown that there were huge shearing work differences for the analysed joints, and they have depended on the process parameters. If the period to the highest shearing force value $F_{t\max}$ was analysed, then the shearing work was, respectively, for the welding parameters 402 J; 245 J; and 132 J (Figure 15). When considering the period for the force F_1 , that is, for a force

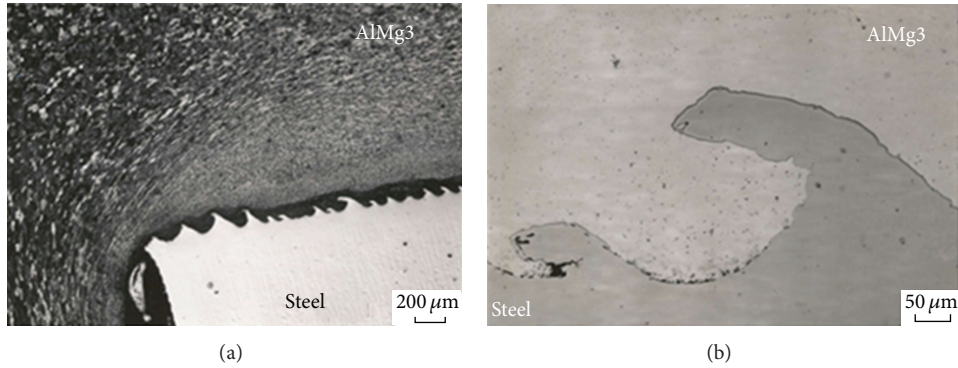


FIGURE 11: The microstructure of the friction welded AlMg3 aluminium alloy-X10CrNiTi189 austenitic steel joint, with a diameter of 30 mm and substantial roughness of the contact surface (a) and the microstructure of such joint (b).

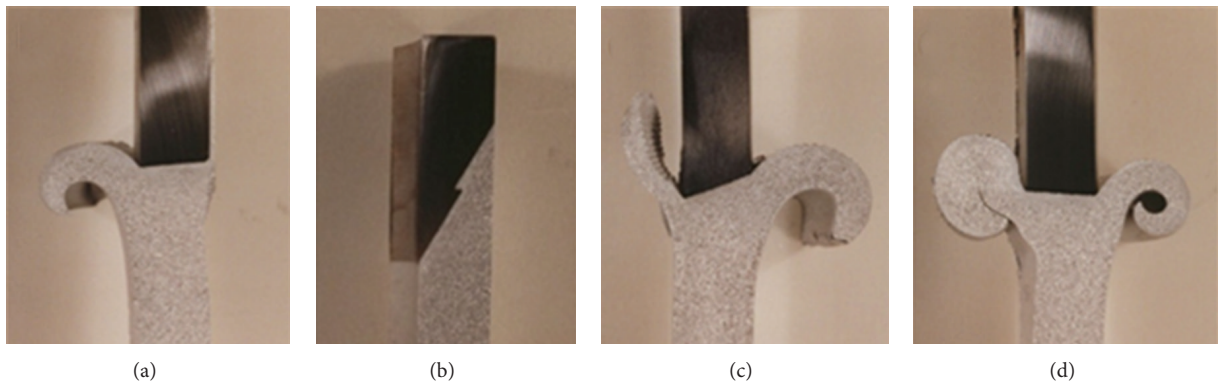


FIGURE 12: The view of a macrostructure of the pipe walls with a diameter of 50 mm, thickness of the wall of 10 mm, from the friction welded AlMg3 aluminium alloy-X10CrNiTi189 austenitic steel joints, at various methods of forming the joints, with a mandrel, limiting the flash inside the pipe. The beven angle of the steel sample -10° , rough turned surface (a), with 45° beven angle and with a lock (b), beven angle of the steel sample -30° , rough turned surface (c), beven angle of the steel sample -10° , but to the inside of the pipe, rough turned surface (d).

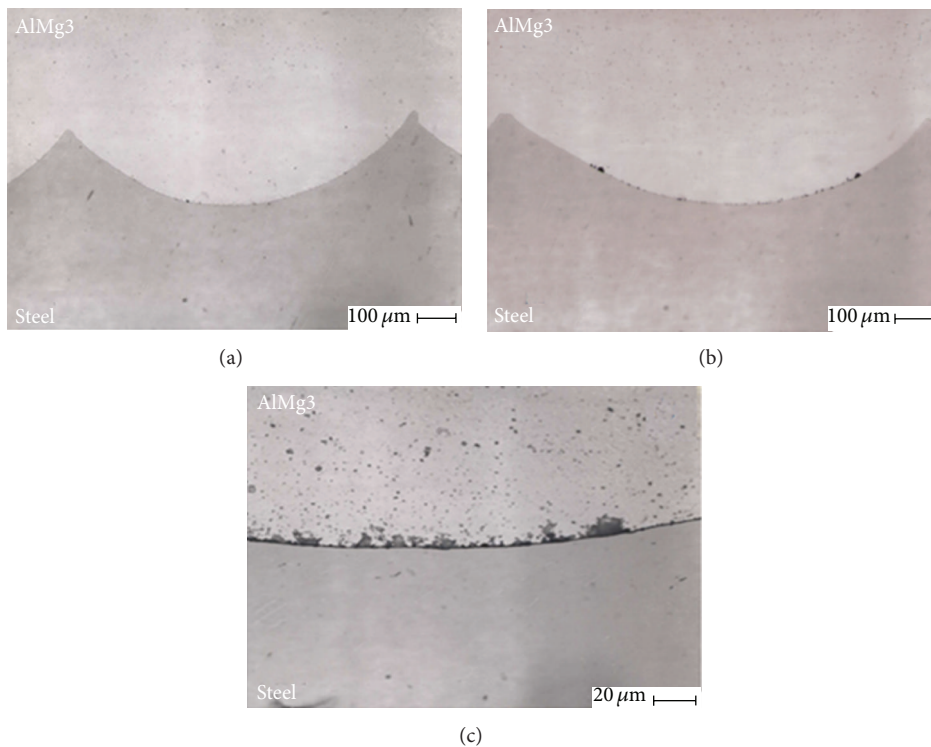


FIGURE 13: The view of a bond zone of friction welded AlMg3 aluminium alloy-austenitic steel joints (light microscope, nonetched specimen, sample no. 2 (a), sample no. 3 (b), and an enlarged fragment of the b (c) (according to [26])).

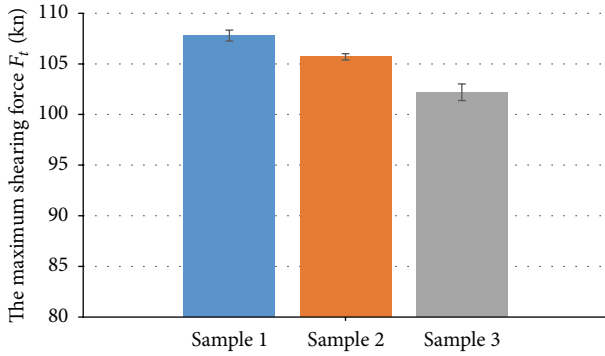


FIGURE 14: The maximum shearing force of the AlMg3 aluminium alloy-X10CrNiTi189 austenitic steel joint (according to [26]).

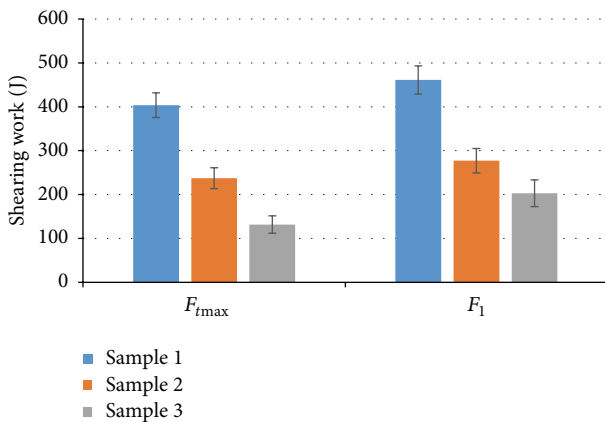


FIGURE 15: The results of shearing work of the investigated AlMg3 aluminium alloy-X10CrNiTi189, austenitic steel joints, determined for two variants of shearing pattern (according to [26]).

lower of 8 kN from the F_{tmax} , then the shearing work has average values, respectively, for 461 J; 270 J; and 198 J (Figure 15).

Comparing the shearing work and the calculated surface area of the aluminium deposition on steel (after the shearing test) has allowed to observe the dependence for increasing the shearing, together with increasing the surface covered with aluminium (Figure 17).

The performed shearing tests of AlMg3 aluminium alloy-austenitic steel joints have allowed stating that the differences in the maximum shearing force of joints formed with various welding parameters were only slight, but the shearing work was different for the joints formed with investigated diversified technological parameters, and could be an important indicator of the joints' quality.

However, it should be noted that the thickness of the intermetallic phases in the friction welded AlMg3 aluminium alloy-X10CrNiTi189 austenitic steel joints was significantly lower (about 1–3 μm) than the one occurring in the diffusion welding (6–8 μm) [29, 30]. For this reason, the friction welded AlMg3 aluminium alloy-X10CrNiTi189 austenitic steel joint can successfully replace the joints formed with diffusion welding.

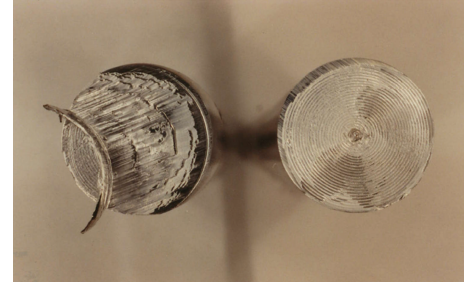


FIGURE 16: The surface of the AlMg3 aluminium alloy-X10CrNiTi189 austenitic steel joint, after the shearing test (parameter no. 1) (according to [26]).

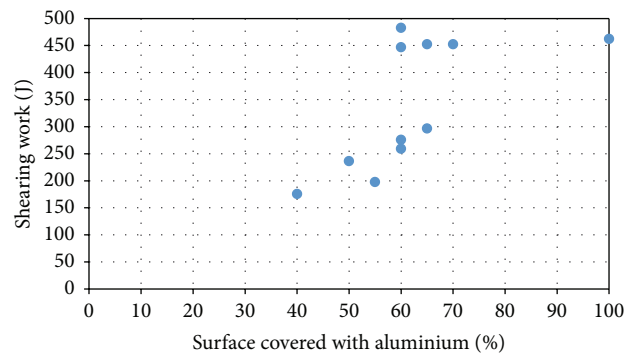


FIGURE 17: The comparison of shearing work of the friction welded AlMg3 aluminium alloy-austenitic steel joints and the surface area of the aluminium sediment on steel (according to [26]).

Towards failures in obtaining the joints with good plastic properties, by direct friction welding of AlMg3 alloy and X10CrNiTi189 steel, further attempts to improve the joint's plastic properties by using the interlayers, formed also with the friction welding method, which is what has been presented in Figure 18, have been conducted.

In the author's first research [13], an Al99.8 pure aluminium interlayer has been used. The obtained joints have been characterized by a tensile strength of 90–185 MPa, depending on the thickness of the interlayer, which has been studied in a range of 3–35 mm (sample no. 4; Table 1).

The technological bending test has caused a strong deformation in the pure aluminium interlayer (Figures 19(b) and 19(c)).

Another material, which has been tested as an interlayer for the joints of AlMg3 alloy-X10CrNiTi189 steel, was titanium. As it was presented in chapter 2.2, in the zone of the friction welded titanium-AlMg3 joint, there was a diffusion layer, whose thickness (up to about 10 μm) has depended on the process parameters. It has been stated that the maximum hardness in the diffusion layer was 222 HV 0.005 and was only slightly higher than the microhardness of titanium (171 HV 0.025).

Since the earlier literature data said that it is not possible to get the joints of titanium-steel, without a layer of brittle intermetallic phases [27, 31], it has been decided to combine AlMg3 alloy with X10CrNiTi189 steel and apply a second

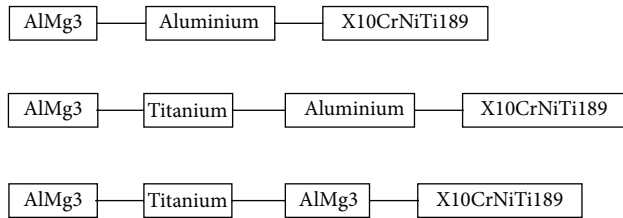


FIGURE 18: The scheme of forming the AlMg3 aluminium alloy-X10CrNiTi189 austenitic steel joint, with interlayers.

interlayer, that is, the layer between the steel and the titanium (Figure 18). For the material of this layer the pure Al99.8 aluminium or the AlMg3 alloy has been used. When forming the joints with pure aluminium, the tensile strength has been equal to 185 MPa, and the fracture has occurred at the bound of the aluminium-steel bond. The technological bending test has proved the strong deformation at the aluminium layer.

Using the AlMg3 alloy, as a second layer, has allowed to obtain joints with a strength of 346 MPa (the fracture at the AlMg3-steel bound) and to achieve the bending angle of more than 120° in the technological bending test. Such behaviour may be caused that despite forming the intermetallic phases on the bound of AlMg3 alloy-X10CrNiTi189 steel, the low thickness of the whole additional interlayer allowed stress transfer occurring in the joint during bending. The deformation was observed behind the titanium layer on the AlMg3 side (Figure 20(c)).

Thus, using the titanium and AlMg3 interlayer in the AlMg3 alloy-X10CrNiTi189 austenitic steel joints has enabled to achieve a joint characterized by high strength and relatively high bending angle.

2.2.3. CrMo4 Steel-AlCuMgNi Aluminium Alloy. In the dissertation [14], the author has presented part of the investigations on the friction welding of the AlCuMgNi aluminium alloy (according to ASTM B247), under the trade name of AN40 as forgings in a T6 supply state (supersaturated and then artificially aged), with steel for quenching and tempering, grade 42CrMo4 in the form of round bars with a diameter of 45 mm. Using of such high diameters of the samples has been determined by the desire to achieve the most accurate approximation of the research for their utilitarian purpose. Such joint was supposed to replace the previous mechanical bonding of the shaft and rotor, produced from these materials and used in some types of turbo boost in large turbo diesel engines.

Toughening steel (42CrMo4), whose chemical compound has been presented in Table 2, after the austenitization in the temperature of about 850°C , depending on the cooling rate, might be characterized by various microstructures, with a hardness of 175 HV–640 HV. The drawing temperature for steel was $480\text{--}650^\circ\text{C}$ and the soft annealing temperature was $680\text{--}720^\circ\text{C}$.

The surfaces of the samples for friction welding have been prepared with turning and washed in ethyl alcohol, directly before welding. The samples of aluminium alloy have been

additionally etched and then washed in ethyl alcohol again. The front surfaces of the steel samples have been joined at an angle of inclination of 2° to the axis, in order to reduce the initial friction moment.

In the first stage of the researches on the AN40-steel 42CrMo4 joints, the researchers have decided to perform the friction welding on the joints, using the parameters presented in Table 1 (sample no. 5). To differentiate the amount of supplied heat various parameters including two rotational speed values have been selected (720 and 1500 min^{-1}).

The results of the metallographic examinations have proved that supplying higher amount of energy in the welding process has caused an occurrence of a cracked diffusion layer with a microhardness of 516 HV (Figure 21), which resulted in the destruction of joints in a tensile test at very low load. The use of a shorter welding time, but higher pressure, has led to disappearance of the diffusion layer, but the joint's strength has been still slight (about 100 MPa). The researchers' conduct in this stage has shown that a little higher strength was a feature of joints that have been formed at lower rotational speed.

There have been attempts of increasing the diffusion interaction on the surface of the AN40-42CrMo4 steel joint, by additional annealing of the joint in the diffusion welder. The researches have shown that for a wide range of welding parameters, it was possible to obtain an increase of the joints' strength, but also the achieved results were unsatisfactory.

Thus, as a result of the conducted researches, it has been stated that by the direct friction welding of 42CrMo4 steel and AN40 aluminium alloy, the mechanical properties of the joints were low (tensile strength up to 100 MPa). An occurrence of a narrow diffusion layer at the joining bound has been stated too. The use of various friction welding parameters, resulting in supplying into the joint a lower amount of heat, has caused not only a disappearance of the diffusion zone, but also a decrease of the joint's strength.

Further attempts have been taken to obtain better properties of the 42CrMo4 steel-AN40 aluminium alloy joint, by using some interlayers, formed with friction welding too.

At this stage, the researchers have decided to use an interlayer, produced from metal, that would have a greater range of forming the solid solution of aluminium, and thus the intermetallic phases' zone should not be formed so quickly in the bonding zone, as it was for direct bonding of 42CrMo4 steel and AN40 alloy. The analysis, of the dual systems from aluminium, has allowed the assumption that none of metals have not formed concentration of the solid solution without intermetallic phases in the whole range. On the base of the previous researches on the diffusion welding process [29, 30], the nickel has been selected.

Thus, the round bars made of 42CrMo4 steel have been friction welded with the nickel plates with dimensions of $2 \times 50 \times 50$ mm, (sample no. 6; Table 1), and then the front surface and nickel/steel joint's side surface have been turned. Such prepared intermediate products were subsequently welded with an AN40 aluminium alloy (sample no. 7; Table 1). The first attempts have allowed obtaining the joints with the strength of 211–235 MPa.

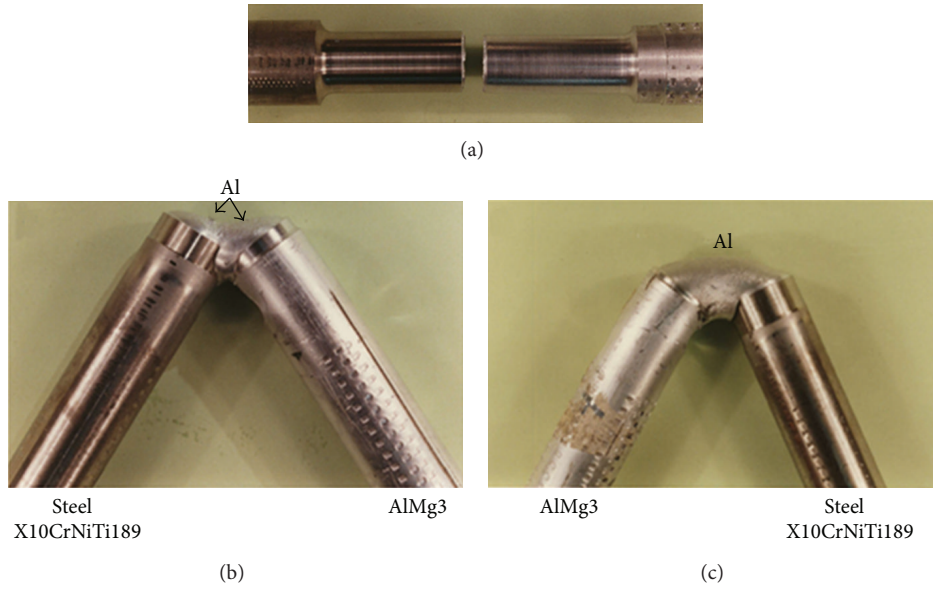


FIGURE 19: The view of a AlMg3 aluminium alloy-X10CrNiTi189 steel joint with an interlayer, with an addition of Al199,8 aluminium (thickness 8 mm) after the static tensile test (a), after the technological bending test (b), and after the technological bending test at the aluminium interlayer with a thickness of 18 mm (c) (according to [13]).

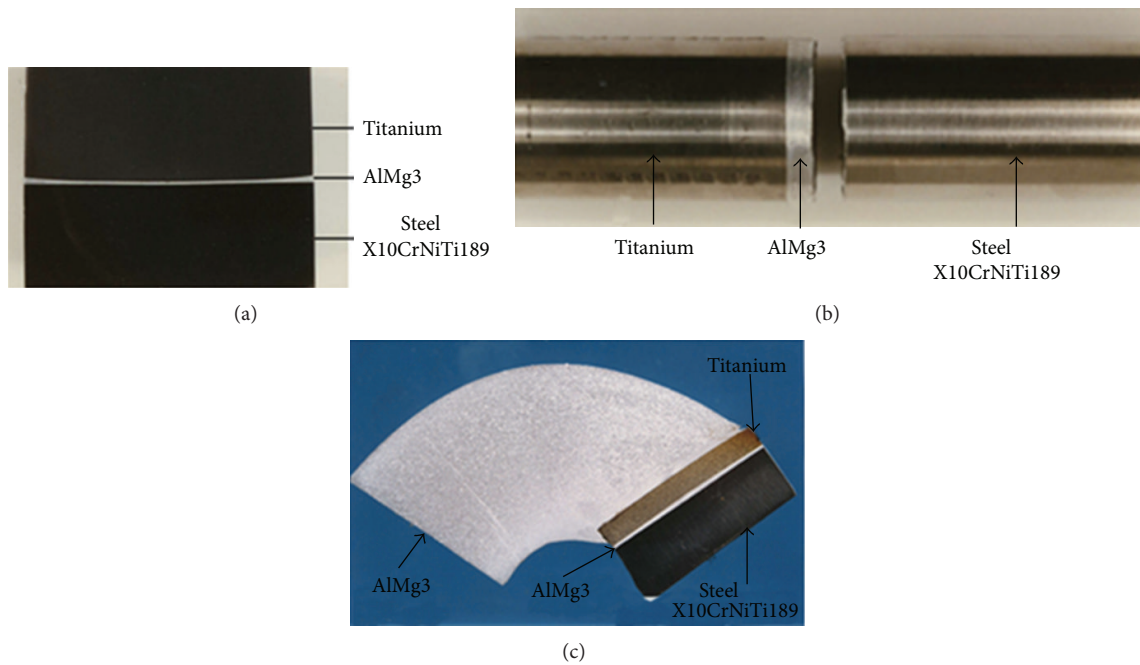


FIGURE 20: The view of a macrostructure of a friction welded titanium-AlMg3-X10CrNiTi189 joint (a), a joint after the tensile test (b), and an AlMg3-titanium-AlMg3-X10CrNiTi189 joint after the technological bending test (c) (according to [13]).

TABLE 2: The chemical compound of the tested materials (according to [14]).

Material	Content, wt%											Others	
	C	Cu	Mo	Si	Mn	Mg	Cr	Ni	Ti	Zn			
AlCuMgNi (acc. to ASTM B247)	min.	0.9	2.3	—	0.2	—	1.4	—	0.9	—	—	0.05	Al—the rest
	max.	1.2	2.7	—	0.25	0.10	1.8	0.05	1.2	0.06	0.1	0.15	
42CrMo4 (acc. to DIN 17200)	min.	0.38	—	0.15	—	0.50	—	0.90	—	—	—	P-max. 0.035	Fe—the rest
	max.	0.45	—	0.30	0.40	0.80	—	1.20	—	—	—	S-max. 0.030	

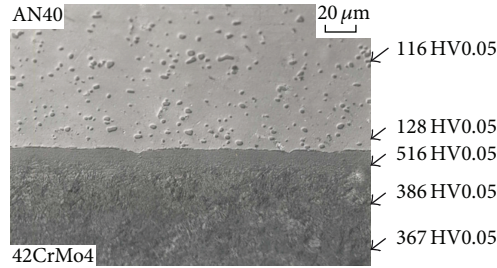


FIGURE 21: The microstructure of the friction welded AN40 alloy-42CrMo4 steel joint.

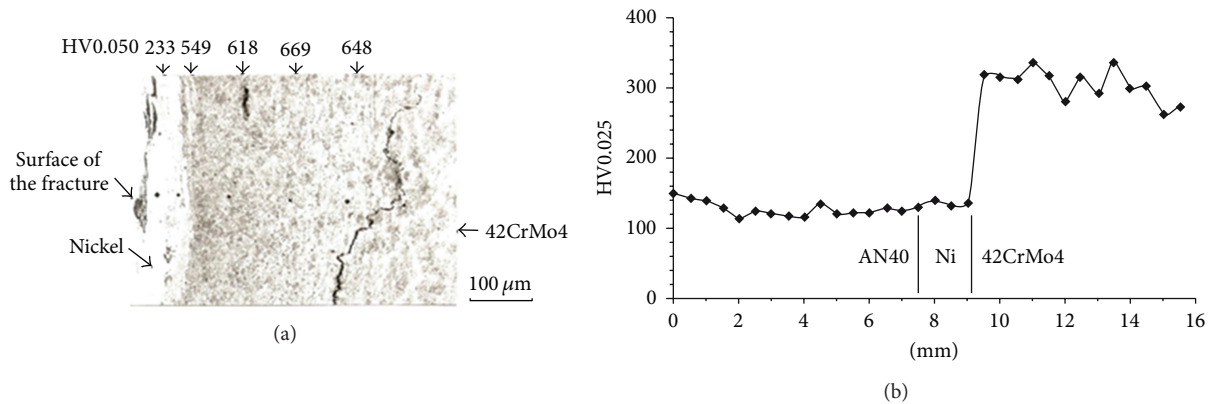


FIGURE 22: The friction welded 42CrMo4 steel-AN40 alloy joints, microstructure after the tensile test (a), and a microhardness pattern (b) (according to [14]).

Further researches have been concerned with a proper preparing of the nickel surface. It has turned out that the rough turning of the front surfaced at the nickel side, instead of an accurate turning, has increased the strength of the joint. It has been stated that the advantageous results were achieved for the front surface with the roughness parameter equal to $R_a = 43 \mu\text{m}$, $R_z = 162 \mu\text{m}$. The performed attempts of additional soaking in a vacuum oven, to produce a wider diffusion layer on the bonding surface, have not resulted in the increase of the joint's tensile strength.

The metallographic researches have proved that after the friction welding of 42CrMo4 steel and nickel, on the steel side, a zone with quenching structures and a microhardness of 648 HV 0.050 has occurred, when the microhardness of the base material was 310 HV 0.050 (Figure 22). In the joints, after the tensile test, some microcracks in this zone have been observed, despite the fact that the fracture of the sample has occurred in the AN40-Ni bonding.

To remove the zone with high hardness in steel, the friction welded 42CrMo4 steel-nickel joint has been heat treated (680°C, 60 minutes, vacuum oven). After such annealing, the next stage of the friction welding has been performed, that is, the AN40 alloy-Ni/42CrMo4 steel joint. The temperatures occurring on the bound of the aluminium alloy-nickel/42CrMo4 steel joint have not caused the austenitization in steel, so the quenching structures were not formed, unlike for welding with materials with higher melting temperatures. The results of the investigations on

the microhardness of such joints are shown in Figure 22. It shows that the heat treatment has caused a disappearance of the hard zone on the steel side (microhardness of steel at the contact zone has reached about 330 HV).

The most advantageous mechanical properties of the joint-tensile strength of about 270 MPa (which is about 70% of tensile strength for AN40 alloy) have been obtained for the joint formed with the following steps: steel-nickel friction welding, heat treatment (high-temperature tempering), and one another friction welding of the achieved steel-nickel joint with aluminium alloy. The view of the joint after the friction welding is presented in Figure 23(a), and the view of the joint after removal of the flash with a visible interlayer from nickel can be seen in Figure 23(b). The microstructure of the joint is shown in Figure 24. On the contact surface of AN40 alloy-nickel, on both sides, there was a visible discontinuous intermetallic phase separation (Figure 24(b)).

The fracture during the tensile test has occurred on the surface of the nickel-aluminium alloy joint. Due to achieving the marginal pressure force values in the device for friction welding (about 400 kN), it has not been possible to use higher upsetting pressure, at samples with a diameter of 45 mm, which would allow improving the mechanical properties of the joint.

There is also a possibility to bond aluminium and steel or aluminium alloys, with the friction stir welding method (FSW) [32, 33]. In the dissertation [34], some examples of welding the AA6061 aluminium alloys with SS400 low carbon

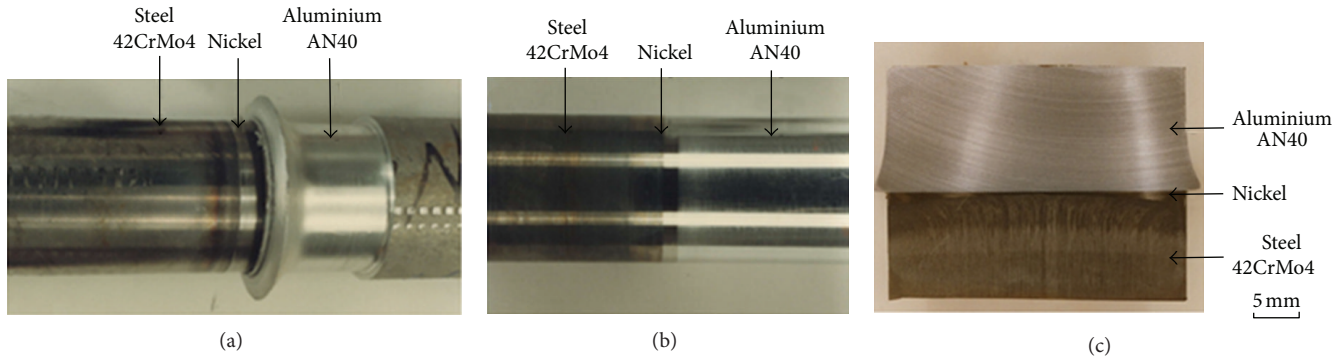


FIGURE 23: The view of the joint after the friction welding of 42CrMo4 steel-AN40 alloy with nickel interlayer, directly after the welding (a), after removal of the flash (b), and the macrostructure of the joint (c).

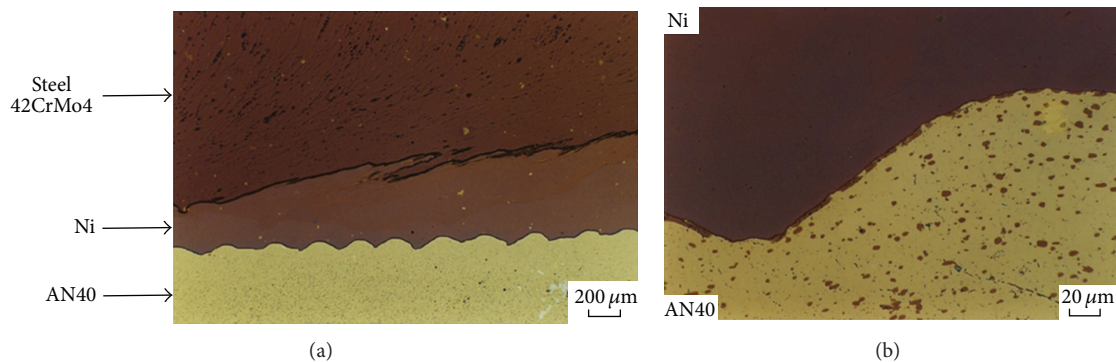


FIGURE 24: The microstructure of the 42CrMo4 steel-AN40 alloy joint with the nickel interlayer (a) and a fragment of an enlarged microstructure of the nickel-AN40 alloy bounding zone (b).

steel were presented. The authors have used the analysis of variance and other techniques of statistic methods, for the interpretation of the experiment's results. The joints have been formed with two different values of the rotational speed of the device (550 min^{-1} and 800 min^{-1}) and three values of the feed speed (0.9 ; 1.2 ; and $1.5 \text{ mm}\cdot\text{s}^{-1}$). It has been stated that the lowest fracture work has reached 36 J and has occurred for the joints formed with the lowest of the investigated rotational speed values of the device (550 min^{-1}).

The results of the butt welding of X5CrNi1810 austenitic steel and Al 6013 aluminium alloy were presented in [35]. The microscopic observations have proved an inhomogeneous layout of the deformed particles of stainless steel with irregular shapes surrounded by a matrix of aluminium alloy. In some of the particles of steel, which have been in the closure weld, microcracks have occurred. This has been explained as a result of high degree of deformation and an intensive mixing of the materials. The endurance limit of the joint has been about 30% lower than the endurance limit of the aluminium alloy.

3. Conclusion

The different research issues that can occur during friction welding of dissimilar materials were described in this paper.

The structural effects during welding, mechanical properties of joints, and different configurations of the process in order to obtain high-quality welds were analyzed.

The analysis of the aluminium-iron dual system leads to the conclusion that long time and high temperatures of the process can cause the formation of intermetallic phases. They are likely to be the reason for brittleness of joints. Depending on the type of joined materials and the process parameters different metal compounds having different properties may be formed.

During the friction welding of pure aluminum with austenitic steel intermetallic phases are formed, but the mechanical properties of the joints (strength and the plasticity) are still good and breaking occurs on the aluminum side.

In the industry, especially in marine, aviation, and refrigeration industries, the joints of aluminium alloys and chromium-nickel austenitic steel are applicable. But the alloying additions, which are present in aluminium alloys (especially magnesium), usually aggravate the metallurgic conditions of aluminium bonding. They cause acceleration of the formation of the intermetallic phases at the joint's boundary, because of the increase of the diffusion coefficient. Numerous attempts to reduce the number of brittle compounds in the transition zone associated with the selection of process parameters or changing the geometry of bonding's surface did not bring the expected results. The way to obtain

good plastic properties in this kind of joint is the use of different kinds of interlayers, for example, titanium, nickel, aluminium, or mixed as titanium-aluminium interlayers. Moreover if the steel has a tendency to create the quenching structures it is possible to remove the zone with high hardness in steel with the use of heat treatment.

Nomenclature

p_{t1}/p_{t2} :	Friction pressure (MPa)
t_{t1}/t_{t2} :	Friction time (s)
p_s :	Upsetting pressure (MPa)
s_t/s :	Shortening (mm)
R_m :	Minimum ultimate tensile strength (MPa)
R_z :	Roughness parameter (ten-point height) (μm)
R_a :	Roughness parameter (arithmetic average height) (μm)
$F_{t\text{max}}$:	Maximum shearing work (kJ)
F_1 :	Shearing work (kJ).

Conflict of Interests

The authors declare that there is no conflict of interests regarding the publication of this paper.

References

- [1] P. D. Sketchley, P. L. Threadgill, and I. G. Wright, "Rotary friction welding of an Fe3Al based ODS alloy," *Materials Science and Engineering A*, vol. 329–331, pp. 756–762, 2002.
- [2] I. Bhamji, M. Preuss, P. L. Threadgill, and A. C. Addison, "Solid state joining of metals by linear friction welding: a literature review," *Materials Science and Technology*, vol. 27, no. 1, pp. 2–12, 2011.
- [3] N. Alberti and L. Fratini, "Friction stir welding: a solid state joining process," *Advanced Manufacturing Systems and Technology*, vol. 486, pp. 67–86, 2005.
- [4] M. Sahin, "Friction welding of different materials," in *International Scientific Conference*, pp. 19–20, Gabrovo, Bulgaria, November 2010.
- [5] R. N. Shubhavardhan and S. Surendran, "Friction welding to join dissimilar metals," *International Journal of Emerging Technology and Advanced Engineering*, vol. 2, no. 7, 2012.
- [6] M. Sahin, "Joining of stainless-steel and aluminium materials by friction welding," *International Journal of Advanced Manufacturing Technology*, vol. 41, no. 5-6, pp. 487–497, 2009.
- [7] H. Ochi, K. Ogawa, Y. Yamamoto, and Y. Suga, "Friction welding of aluminum alloy and steel," *International Journal of Offshore and Polar Engineering*, vol. 8, no. 2, pp. 140–143, 1998.
- [8] S. Sundaresan and K. G. K. Murti, "Formation of intermetallic phases in aluminium-austenitic stainless steel friction welds," *Metals Forum*, vol. 17, no. 3, pp. 301–307, 1994.
- [9] S. Fukumoto, H. Tsubakino, K. Okita, M. Aritoshi, and T. Tomita, "Microstructure of friction weld interface of 1050 aluminium to austenitic stainless steel," *Materials Science and Technology*, vol. 14, no. 4, pp. 333–338, 1998.
- [10] H. Seli, A. I. M. Ismail, E. Rachman, and Z. A. Ahmad, "Mechanical evaluation and thermal modelling of friction welding of mild steel and aluminium," *Journal of Materials Processing Technology*, vol. 210, no. 9, pp. 1209–1216, 2010.
- [11] T. J. Jessop, E. D. Nicholas, and W. O. Dinsdale, "Friction welding dissimilar metals. Advances in welding processes," in *Proceedings 4th International Conference*, pp. 23–36, The Welding Institute, Harrogate, England, 1978.
- [12] S. J. NA, *Das Reibschweissen Ungleichartiger Metalle*, Praca doktorska TU, Braunschweig, Germany, 1983.
- [13] A. Ambroziak, *Badania Zgrzewanych Tarciowo Zlaczty AlMg3-Stal Austenityczna*, Inzynieria Materialowa, 2003.
- [14] A. Ambroziak, *Zgrzewanie Tarciove Stali 42CrMo4 Ze Stopem Aluminium AlCuMgNi*, Energetyka, 2008.
- [15] T. B. Massalski, H. Okamoto, P. R. Subramanian, and L. Kacprzak, *Binary Alloy Phase Diagrams*, ASM International, 2nd edition, 1990.
- [16] S. Elliott and E. R. Wallach, "Joining aluminum to steel," *Metal Construction*, vol. 13, no. 3, pp. 167–171, 1981.
- [17] B. S. Yilbaş, A. Z. Şahin, N. Kahraman, and A. Z. Al-Garni, "Friction welding of StAl and AlCu materials," *Journal of Materials Processing Technology*, vol. 49, no. 3-4, pp. 431–443, 1995.
- [18] A. Ambroziak, *Zgrzewanie Tarciove Materialow o Różnych Właściwościach*, Oficyna Wyd. PWR, Wrocław, Poland, 2011.
- [19] J. Senkara and H. Zhang, *Mechanizm I Czynniki Technologiczne Wplywajace Na Pękanie Stopu AlMg3 Podczas Wielopunktowego Zgrzewania Rezystancyjnego*, Przegląd Spawalnictwa, 2006.
- [20] V. V. Trutnev and M. H. Šoršonov, *Diffuzjonnaia Svarka Austenitnoj Stali S AlumInem I Jevo SplavamI*, 1967.
- [21] M. Kikuchi, H. Takeda, and S. Morozumi, "Bonding interfaces in friction- and explosive- welded aluminum and steel joints," *Journal of Japan Institute of Light Metals*, vol. 34, no. 3, pp. 165–173, 1984.
- [22] S. Fukumoto, M. Ohashi, H. Tsubakino et al., "Microstructures of friction welded joint of 6061 aluminium alloy to 304 stainless steel," *Journal of Japan Institute of Light Metals*, vol. 48, no. 1, pp. 36–41, 1998.
- [23] S. Fukumoto, H. Tsubakino, K. Okita, M. Aritoshi, and T. Tomita, "Friction welding process of 5052 aluminium alloy to 304 stainless steel," *Materials Science and Technology*, vol. 15, no. 9, pp. 1080–1086, 1999.
- [24] S. Fukumoto, H. Tsubakino, K. Okita, M. Aritoshi, and T. Tomita, "Amorphization by friction welding between 5052 aluminium alloy and 304 stainless steel," *Scripta Materialia*, vol. 42, no. 8, pp. 807–812, 2000.
- [25] G. Kawai, K. Ogawa, and H. Tokisue, "Friction welding of 6061 aluminium alloy pipe to S25C carbon steel pipe," *International Journal of Offshore and Polar Engineering*, vol. 8, no. 2, pp. 144–147, 1998.
- [26] A. Ambroziak, M. Korzeniowski, and M. WINNICKI, *Ocena Właściwości Mechanicznych Zgrzewanych Tarciowo Zlaczty Stop Aluminium EN AW-5754-Stal Austenityczna*, Przegląd Spawalnictwa, 2010.
- [27] A. Ambroziak, *Dobór Warstw Przejściowych Dla Różnoimiennych Zlaczty Zgrzewanych Tarciowo*, Biuletyn Instytutu Spawalnictwa w Gliwicach, 1999.
- [28] K. Mechner and H. Klock, *Grenzflächengefüge Von Reibschweissverbindungen Aus Aluminium Und Stahl*, Aluminium, 1983.
- [29] R. Lison, *Schweissen Und Löten Von Sondermetallen Und Ihren Legierungen*, Düsseldorf, Germany, 1996.

- [30] R. Lison, *Wege Zum Stoffschluss Über Schweiß- Und Lötprozesse*, Fachbuchreihe Schweißtechnik, 1998.
- [31] A. Ambroziak, *Zgrzewanie Tarcowe Metali Trudno Topliwych W Cieczy Na Tle Innych Metod Spajania*, Oficyna Wyd. PWr, Wrocław, Poland, 1998.
- [32] R. S. Mishra and M. W. Mahoney, *Friction Stir Welding and Processing*, United States of America, ASM International, 2007.
- [33] R. S. Mishra, R. K. Islamgaliev, T. W. Nelson, Y. Hovansky, and M. W. Mahoney, "Abnormal grain growth during high temperature exposure in friction stir processed 7050 and 2519 aluminum alloys," in *Proceedings of Symposium on Friction Stir Welding and Processing*, pp. 205–216, Indianapolis, Ind, USA, November 2001.
- [34] T. Chen and W.-B. Lin, "A study on dissimilar FSW process parameters in aluminum alloy and low carbon steel," in *International Conference on Smart Manufacturing Application (ICSMA '08)*, pp. 9–14, Gyeonggi-do, Korea, April 2008.
- [35] H. Uzun, C. Dalledonne, A. Argagnotto, T. Ghidini, and C. Gambaro, *Friction Stir Welding of Dissimilar Al 6013-T4 To X5CrNi18-10 Stainless Steel*, Materials and Design, 2005.

Review Article

The Importance of Materials Data and Modelling Parameters in an FE Simulation of Linear Friction Welding

R. Turner,¹ F. Schroeder,^{1,2} R. M. Ward,¹ and J. W. Brooks¹

¹ School of Metallurgy & Materials, The University of Birmingham, Edgbaston, Birmingham B15 2TT, UK

² Hilti Corporation, 9494 Schaan, Liechtenstein

Correspondence should be addressed to R. Turner; r.p.turner@bham.ac.uk

Received 10 January 2014; Accepted 11 January 2014; Published 26 February 2014

Academic Editor: Wenya Li

Copyright © 2014 R. Turner et al. This is an open access article distributed under the Creative Commons Attribution License, which permits unrestricted use, distribution, and reproduction in any medium, provided the original work is properly cited.

Linear friction welding has become a key technology in the aeroengine industry due to its capability to produce blisk components. Finite element (FE) simulation of linear friction welding applications has been studied in recent years by a number of institutions, using a variety of software codes. Several codes have been demonstrated to be capable of predicting with reasonable accuracy some or all of the critical outputs of friction welding, namely, the thermal loading, plastic deformation, and residual stresses generated. The importance of reliable material data in performing these calculations is paramount. Available material data in the published literature is often restricted to lower temperatures and strain rate regimes. Extrapolation methods used on this data to estimate high temperature properties can lead to uncertainties in the modelled predictions. This paper reviews the approach to materials modelling, including material datasets and material constitutive laws, for FE simulation work in the literature regarding linear friction welding. Best-practice methods for materials constitutive laws, materials data-sets, and the associated experimental temperatures and strain rates used to gather data are suggested. Finally, successfully validated modelled outcomes—when a robust, reliable, and accurate material database has been selected—are demonstrated for a number of the FE methods considered.

1. Introduction

Linear friction welding is a solid-state joining process which, if successfully implemented into the civil aeroengine industry, could allow for a significant reduction in the weight of these engines and in turn produce benefits in performance, economy, and emissions [1]. This is achieved by replacing the dovetail mechanical joint that holds the blades to the discs with a weld line—to form an integrally bladed disc or blisk component [2]. The process has been well described within the literature, in terms of its process parameters and the process phases [3]. Whilst much of the research has been focused upon microstructural characterisation and weld quality, a number of papers have considered the governing process physics and used FE analysis to better understand these process fundamentals. Linear friction welding is an ideal method of joining components, such as the blisk, given the nonaxisymmetric nature of the joint and the size of the component. In essence, the process consists of holding one component stationary, whilst linearly oscillating a second

component, with the two in contact and under an applied normal force, as illustrated in Figure 1.

Whilst solid-state welding methods are not the only processing route for such a component—mechanical fixturing of the blade-root such as a dovetail joint and machining from solid would also be possibilities—there are distinct benefits that a solid-state weld such as linear friction welding offers. These include: (i) the capability to join together different materials or to join hollow blades to the disc—something that machining from solid could not achieve [4]—and (ii) a significant reduction in component weight in comparison to a mechanical fixturing at the blade-disc interface.

1.1. FE Simulation Methods in the Literature. Process modelling of linear friction welding has been studied in recent years by a number of academic and industrial organisations [5–15], with various FE software packages demonstrated to be reasonably capable of representing this joining technology, including DEFORM [9–11, 14], FORGE [13], Elfen [5],

TABLE 1: Details of current LFW FE simulation publications, their material formulation, meshing used, and validation methods.

Publication	Software	Dimension	Finest mesh size [mm]	Material data	Validated results
Vairis and Frost [5]	ELFEN	2D	n/a	Tabular	Temperatures and shear stress
Li et al. [6]	ABAQUS	2D	0.5	Johnson-Cook	n/a
Ceretti et al. [10] Fratini et al. [9], Fratini and La Spisa [11]	DEFORM	2D, 3D	0.6 0.5, 0.25	Tabular Equation-based	Upset rate
Sorina-Müller et al. [12]	ANSYS	3D	0.125	Tabular	Upset rate
Turner et al. [13]	FORGE 2008	2D	0.25	Tabular & Norton-Hoff	Flash morphology, temperatures upset rates, and residual stress
Schroeder et al. [14]	DEFORM	2D	0.08	Tabular	Temperatures, upset rates, and flash morphology

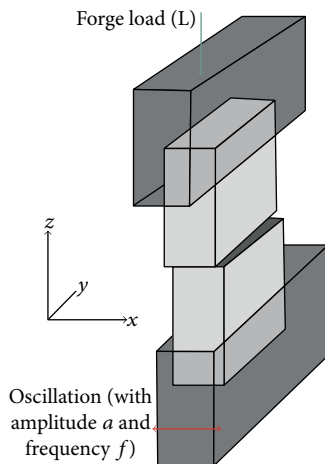


FIGURE 1: Schematic of a linear friction weld, showing the testpieces, tooling, and axes of motion.

ABAQUS [6–8], and ANSYS [12, 15]. Table 1 summarises the literature on FE simulation of the LFW process. However, the accuracy of any such models will depend upon the input data, including the mesh used (see Figure 2), thermal profiles (if these are not predicted internally), boundary conditions employed to replicate the tooling and clamping, and the materials data used to describe the alloys being joined. Given that this technology is so far most widely used in aeroengine industries, most of the research to date has been focused upon the traditional aerospace materials: titanium alloys [5, 6, 12–14], nickel alloys, and steels [9–11]. The linear friction welding process must be modelled as a fully coupled thermal-mechanical analysis as the heating produced by the shearing and deformation of the material is necessary for the process to operate.

A purely analytic solution to the thermal field arising during a friction welding process was proposed by Grong [16]; however, the first attempt at an FE simulation of the LFW

process was made by Vairis and Frost [5], in which groundbreaking research within this field was made. The model was computed in Elfen, using a mesh of 764 elements, a considerable computational problem for the computers of the time. The model was reduced to consider just a half of the welded joint, one side of the weld line. Materials data for the alloy Ti-6Al-4V was entered into the model in tabular format, at limited temperatures, with the software interpolating data for other temperatures. A linear decay of yield stress with increasing temperature was assumed. Other materials data was entered at the average values for the temperature range anticipated. The model achieved reasonable correlation for thermal predictions when compared to thermocouple measurements; the authors comment that thermocouples can underestimate the actual conditions due to the limited control over the thermal inertia, the response time, and the positioning of the junction in the specimen. It was demonstrated that a purely analytic model with assumed temperature-independent material properties predicted significantly higher temperatures than the FE model. It was also first stated that the sparks produced during the process were of negligible impact upon the process, meaning that FE simulation of the component, ignoring losses through this exothermic reaction, would be sufficient.

Li et al. [6–8] published work on 2D LFW modelling of a titanium alloy in ABAQUS, suggesting that temperatures achieved during linear friction welding were higher than Vairis proposed, reaching approximately 1000°C before achieving a relatively steady state. The materials data that was implemented into the model by Li used the Johnson-Cook law to describe the material flow-stress behaviour, given in

$$\sigma_y = [A + B(\epsilon_p)^n] [1 + C \ln(\dot{\epsilon}_p^*)] \left[1 - \left(\frac{T - T_0}{T_m - T_0} \right)^m \right], \quad (1)$$

where σ_y is the flow-stress, ϵ_p is the plastic strain, $\dot{\epsilon}_p^*$ is the normalised plastic strain rate, T_0 is a reference temperature,

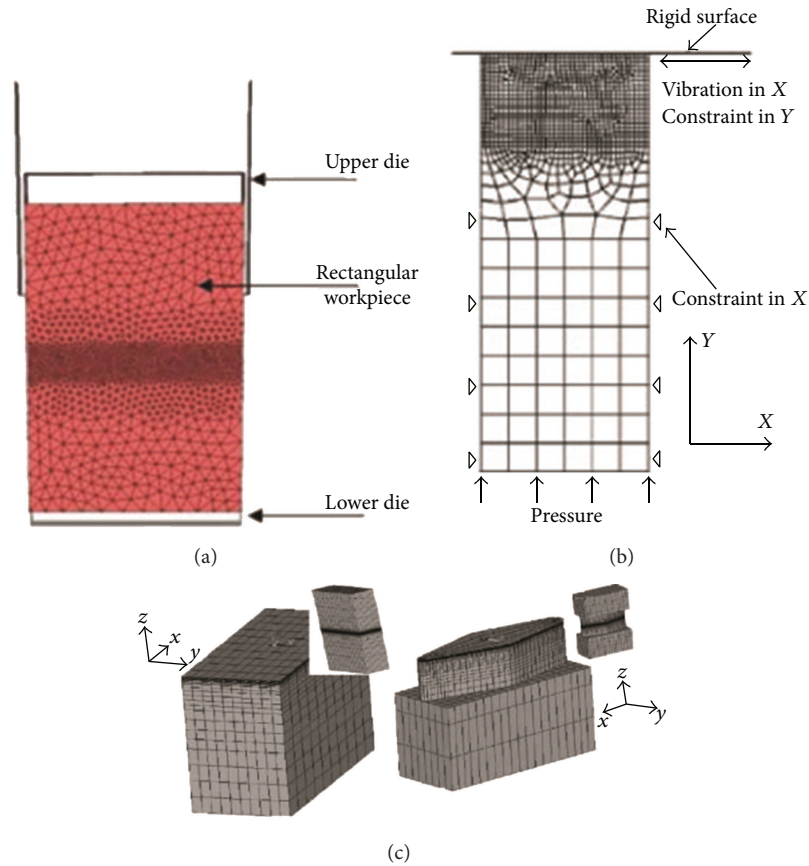


FIGURE 2: Diagrams showing the meshing used typically for a 2D testpiece LFW process model in various LFW FE simulations: (a) 2D simulation of both sides of the joint, (b) 2D simulation of 1 side of the joint, and (c) 3D simulation.

T_m is a melting temperature, and A , B , C , m , and n are material constants. Values assigned to A , B , C , m , and n are detailed within literature [6]. A temperature-independent density and Poisson ratio were used. Temperature-dependent measurements of properties such as thermal conductivity and heat capacity were included. However, measured data available within the literature commonly only reaches temperatures of 600°C , and as such extrapolation methods are required to estimate materials properties higher than this. Li et al. estimated materials properties up to 1000°C . Therefore, should the predicted temperature at any node exceed 1000°C , the software would be required to extrapolate outside of its known database. The mesh employed by Li et al, shown in Figure 2, was finer than that of the ELFEN model, owing largely to the far superior computing power available to the researchers compared to a decade before. Elements at the weld line were 0.5 mm in length, coarsening gradually away from the weld. The ABAQUS model was again considering one half of the weld only. It is probable that the refined element size was the key contributor to increasing the modelled weld line temperatures, owing to the steep thermal gradient located close to the weld. Larger elements would not be capable of capturing the resolution of such steep thermal gradient over such a small distance.

Fratini and Ceretti et al. [9–11] developed a modelling capability using the software package DEFORM by SFTC.

Work presented using a 2D approach [10] had a tabular AISI 1045 steel material file from the software's material library and a mesh with a minimum element size of 0.6 mm . Temperatures were generated using a time dependent shear factor at the interface. The results were validated in terms of upset rate; however, the flash morphology predicted by the model was not validated. The thermal gradient at the weld interface was approximately 900°C across 9 elements with a peak gradient of about 600°C across 3 elements. With thermal gradients being this high, material properties are likely to vary considerably across the size of an element which could limit the accuracy of the model (examples of a typical tabular input for the thermal conductivity and specific heat for Ti-6Al-4V found in literature [17] are given in Figure 3). This could be confirmed by consideration of the data or a mesh sensitivity study. A 3D model was presented by the authors [9] applying an equation-based material formulation and a minimum mesh size at the weld interface of 0.5 mm [10] which was further reduced to 0.25 mm in [9]. A temperature-dependent shear friction coefficient was assumed; however, it is not clear how this was determined. Predicted upset rates from the 2D and 3D models were compared to experimental results and displayed better agreement for three dimensional models. The model with reduced mesh size was interrogated for predicted weld interface temperatures at different process parameters, and these were compared to

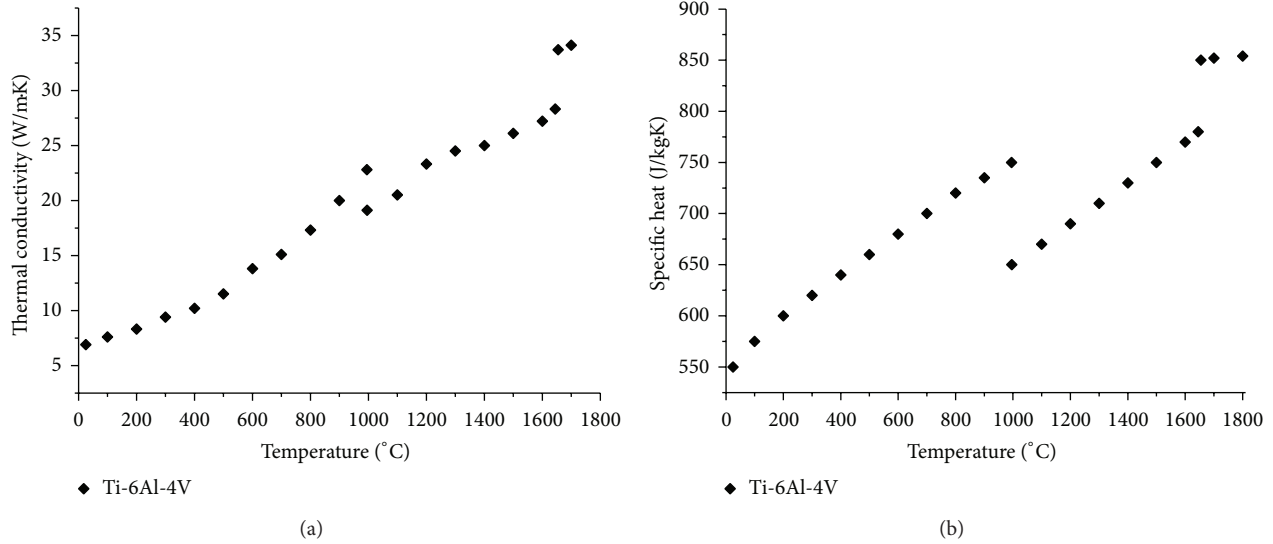


FIGURE 3: Titanium alloy data available within the literature [17] for (top) thermal conductivity and (bottom) specific heat.

data from experiments. A comparison of the upset was made, demonstrating reasonable agreement during the initial stage; however, constant upset during the equilibrium phase of the process appears higher in the experiment compared to the model.

Sorina-Müller et al. [12] presented an ANSYS 3D model of linear friction welding of titanium alloys. They developed work from simple block geometry to a small-scale “blade-like” geometry. The mesh employed in the ANSYS model contained elements with length 0.125 mm at the weld and gradually coarsened away from the weld—see Figure 2. The model was primarily validated using axial shortening data from experiments. Materials data was entered into the ANSYS model as a temperature-dependent tabular format. Materials tests, including dilatometry, differential scanning calorimetry, and the laser flash method, were employed to determine the thermal expansion, heat capacity, and thermal diffusivity, respectively. It was recommended that materials properties should be measured or estimated up to temperatures of approximately 1250°C. This would prevent any unwanted software extrapolation of results—so long as modelled temperatures do not reach this high. Peak temperatures at the weld line will be dependent upon process parameters. Hence, the material database will need to consider the LFW process parameters to ensure that the model remains within the range of input data. The rigorous approach to materials modelling produced an FE model which agreed well with experiments. Sorina-Müller et al. also state that their linear friction welding simulation would be capable of considering different material conditions on either side of the weld line, specifically a different processing route for the titanium alloys to produce subtly different material. This would suggest that a full model, rather than half-model, would produce a more rigorous modelling approach, when considering industrial materials and components.

Turner et al. [13] proposed a 2D FE simulation using a plane-strain mode, using FORGE2008. This model

considered the full weld, as opposed to just half, and represented the joining of the alloy Ti-6Al-4V to itself. As with other work, a graded mesh was employed—see Figure 2 for a comparison of meshes. The material data used to perform the FE calculations came from Sente software’s JMatPro database. This data included a tabular flow-stress input deck for varying strains (0.01 to 4), strain rates (0.001 s⁻¹ to 1000 s⁻¹), and temperatures (25°C to 1200°C); tables for thermal conductivity, thermal expansion, specific heat, density, and Poisson’s ratio—all as a function of temperature (25°C to 1200°C). Upon analysis of the FE model, strain rates predicted by the model at the weld line were reported to be as high as 2500 s⁻¹ for certain modelling conditions, although generally they were below 1000 s⁻¹. This could have led to unwanted extrapolation of data as processing conditions were occasionally out of the specified input range. It was noted that, in the FORGE2008 work, the models which used the tabular data offered the more accurate solutions for all outputs (i.e., temperature, residual stress, and distortion), when compared to models based on the Norton-Hoff equation:

$$\sigma_y = \sqrt{3}^{(m+1)} K \dot{\epsilon}^n \epsilon^m e^{-\beta T}, \quad (2)$$

where σ_y is the flow-stress, ϵ is the plastic strain, $\dot{\epsilon}$ is the plastic strain rate, T is the material temperature, and m , n , K , and β are material constants.

Despite potentially increasing the computational demand, a tabular dataset can excel in accurately representing the material behaviour at a wide range of processing conditions [18]. Equation-based approaches—and the coefficients considered—must be carefully selected to produce the same successful outcome. An equation-based material flow-stress law, such as the Johnson-Cook or the Norton-Hoff, may struggle to accurately reflect material behaviour for a wide range of both temperature and strain rate. However, the equation-based approach does remove any need for data

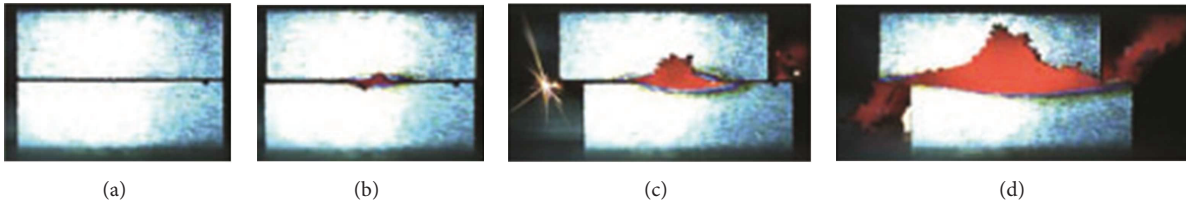


FIGURE 4: High-speed photography of a titanium alloy linear friction weld [14].

interpolation—something which is reliant on the software rather than the material model and is more computationally efficient than a tabular method. It is important for the tabular dataset to be well populated—as titanium alloys such as Ti-6Al-4V are known to undergo a rapid degradation of mechanical and structural properties [19] at elevated temperatures. A well-populated dataset would be able to represent this rapid degradation by a sensible distribution of data points. However, for both a tabular and an empirical equation-based fit, there is no capture of the thermomechanical processing history effects. The full impact upon microstructure and material properties of work-hardening or the heat treatment undergone during the rapid heating within a friction weld is something that these approaches do not consider, and a microstructural modelling capability would be required if these effects were to be incorporated within the modelling framework.

The model from [13] was developed further by Schroeder et al. [14] in DEFORM, again considering a 2D plane-strain methodology, targeting the different process phases of conditioning and equilibrium. Thermal profiles generated during conditioning were predicted and subsequently validated to establish an initial condition for the equilibrium model. It was shown that the temperatures depend on not only process parameters but also the shape of the thermal profile. Thermal loading at the weld line during equilibrium was suggested to be even higher than previously measured or modelled (subject to weld parameters used), with weld line temperatures exceeding 1200°C predicted. Thermal measurements made with thermocouples confirmed temperatures exceeding 1200°C . High-speed photography methods were implemented to better understand the fundamental process physics associated with material extrusion and flash formation. These images were then compared to the modelled predictions for flash formation mechanisms. Still images from the high-speed photography are presented in Figure 4 [14].

Research by Kiselyeva et al. [15], using the popular FE code ANSYS, has explored the 2D simulation of the equilibrium phase of a linear friction weld. The titanium alloy being modelled was assumed to have an isotropic elastic material model during the heating stage, switching to a viscoelastic model to accurately predict the deformation and flash formation. Although element size at the weld line is not quoted, it appears to be of a similar size to those used in other ABAQUS and DEFORM linear friction weld models.

2. Results and Discussion

Once an established material modelling database has been created and incorporated into the FE model, the model outputs can be studied. The DEFORM models by Schroeder et al. [14], the FORGE models by Turner et al. [13], the ANSYS models by Sorina-Müller et al. [12], and the ABAQUS models by Li et al. [6–8] were all analysed for their predicted temperatures at the weld line. Each model predicted that weld line temperature would exceed 1000°C —subject to the welding process parameters—offering reasonable assurances that the FE models, whilst built in different software codes, utilising different methods of modelling the associated material, were considering the correct physical processes and mechanics to simulate the weld. All modelling techniques considered the heating within the component via plastic deformation during steady-state welding. The thermal results are presented in Figures 5(a), 5(b), and 5(c) and demonstrated the localised nature of heating. The FORGE models, considering different applied axial loads, predict the peak weld line temperatures varying from weld to weld by $\sim 100^{\circ}\text{C}$. The mechanism of extruding the hot material out of the weld and into the flash maintains a reasonably constant thermal profile across the three welds.

It is important to understand which of the modelled outputs are considered critical to the success of an FE model. The different papers sought to validate their models using different outputs, such as upset rates, flash morphology, residual stresses, and temperatures to validate the models.

Within their 2D linear friction welding simulations considering both sides of the weld, Turner et al. and Schroeder et al. targeted upset rates, thermal loads, and accurate flash morphology. Other FE models studied in the literature have less accurate flash formation morphology prediction, but this may not have been targeted as an important output for them. Flash formation could be considered an output of secondary importance, given that it will not form any part of the final weld condition in a real component. However, the possibility of material being dragged back inside the weld after being exposed to the atmosphere would suggest that flash formation is a potentially critical model output. Turner et al., and in turn Schroeder et al., targeted flash morphology accuracy to provide a visual verification that their FE models were considering the correct deformation modes and that material data was reasonable. Flash morphology gives reasonable insight into the welding process

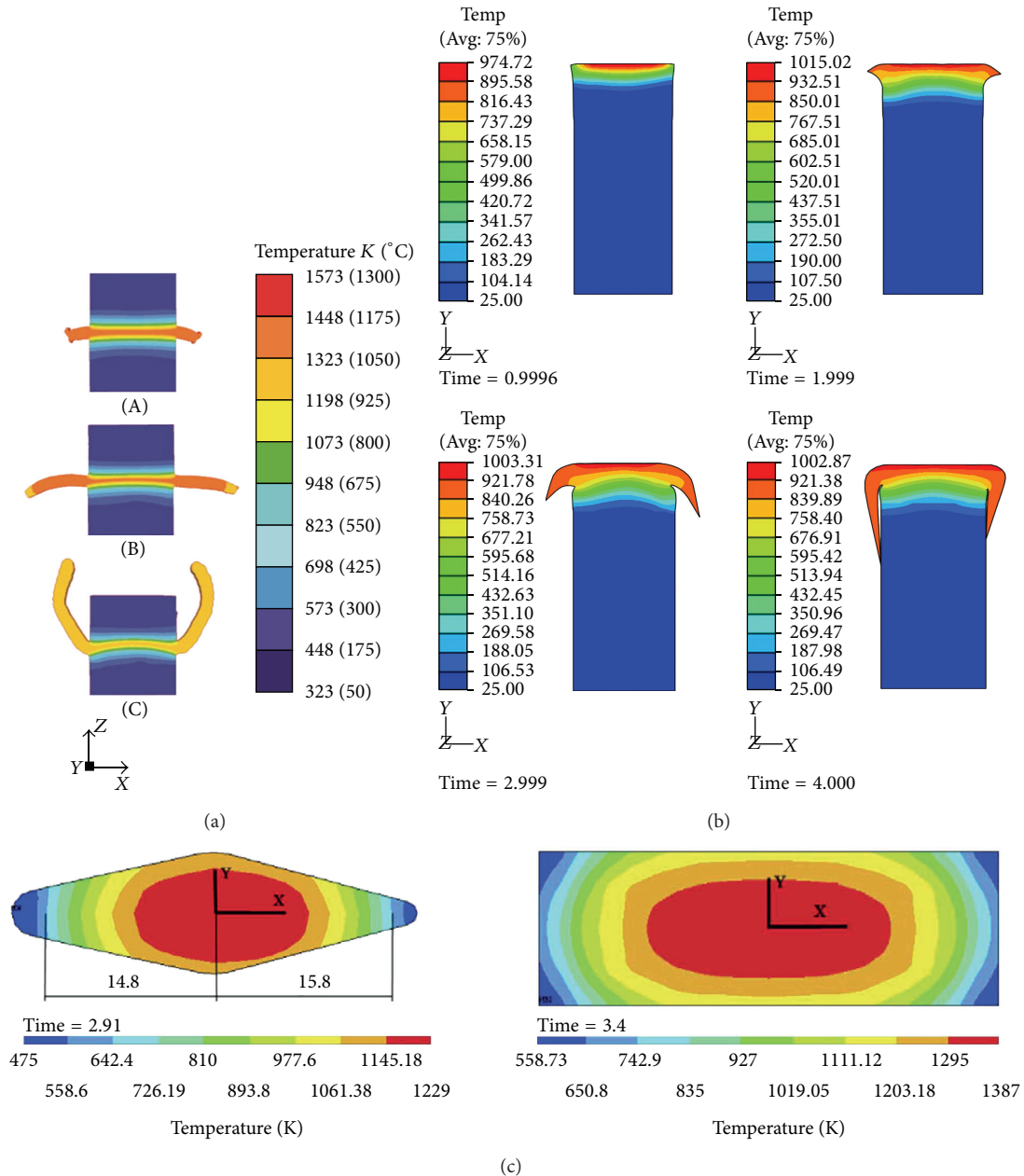


FIGURE 5: (a) Thermal profiles predicted for 2D LFW simulation considering both sides of the weld, at three different pressures: (A) low pressure, (B) medium pressure, and (C) high pressure [13]. (b) Thermal profile predicted for 2D LFW simulation considering only one side of the weld, for Ti-6Al-4V, at different times during the process [6]. (c) Thermal profile on the weld interface for a 3D LFW simulation, considering a “blade-representative” geometry [12].

and can potentially allow for initial assessments of weld line quality. Figure 6 illustrates the predicted flash morphology within the models, for (top) low amplitude and high pressure and (bottom) high amplitude and low pressure welds, and compares the modelled predictions to similar experimental welds. The nature of the flash morphology between modelled prediction and experiment is similar. The distinct rippling observed in the 2nd case suggests that the flow-stress tabular input for Ti-6Al-4V used in these FE models has captured the correct flow and behaviour properties of this material, relating to the deformation mode of the flash as it is extruded

from the weld line. Flash formation and material extrusion resulting in parameter specific upset rates are the product of accurate material data and temperatures. Comparison of upset rates of models and experiments showed they were in good agreement over a wide range of parameters.

3. Conclusions

FE simulation of linear friction welding is currently being driven predominantly by aeroengine manufacturers, often through their associated academic partners, due to the

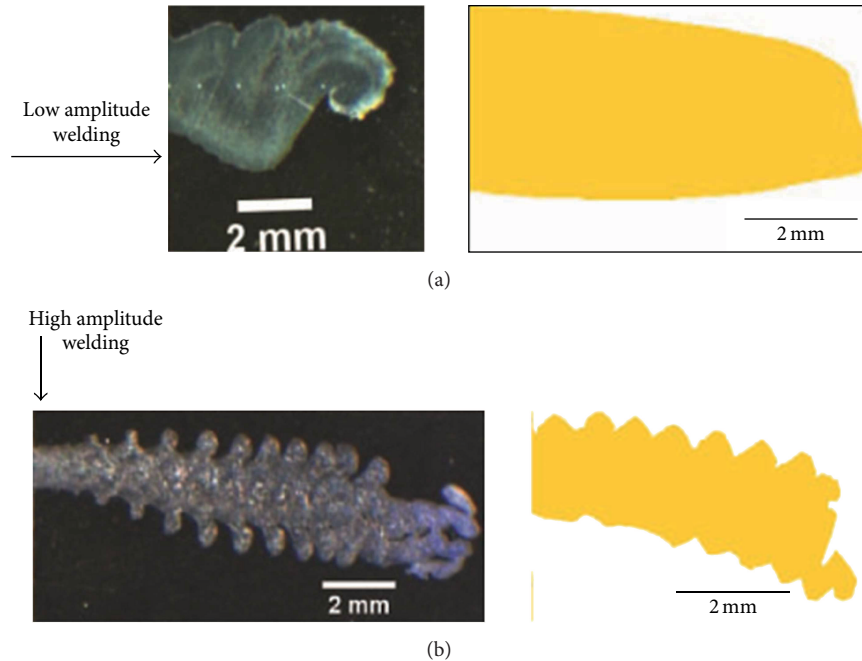


FIGURE 6: Examples of flash formation during LFW; top: smaller amplitude and high applied load and associated modelling; bottom: large amplitude and lower applied load and associated modelling [14].

importance of this process in producing high-value blisk components. Probably related to the locations of the technology centres for these aeroengine manufacturers, research institutions in the UK, the USA, Germany, and China have published simulation work on LFW in recent years, developing the initial model created by Vairis et al., first reported in 1998. When constructing an FE model of LFW, it is important that the intended outputs of the model are considered carefully, by appropriate choices regarding the material database and the modelling parameters such as meshing. With the computational developments over the last decade, modern FE models have the potential to work in much greater detail than previously. This detail could take the form of a finer weld line mesh—if required for the desired model outputs—or real component geometry, as opposed to the simple rectilinear testpieces often used in simulations.

The authors have reviewed the current state of FE simulations of the linear friction welding process and in particular the approach to the materials modelling database and the meshing strategy that each FE method used. The following conclusions are made.

- (i) Several general FE software codes have been demonstrated capable of simulating linear friction welding. Whilst each code may require some detailed knowledge to accurately replicate the process, such as the oscillating motion and the merging of separate meshes, experienced FE users can often adapt these generic codes for their specific purposes.
- (ii) Both tabular and equation-based flow-stress models have been successfully implemented in a linear

friction weld simulation. Each method offers different benefits to the simulation; the tabular approach generally appears to be a more robust and reliable method than the empirically fitted equations chosen to represent various materials so far, whilst an empirical equation-based approach offers greater computational efficiency than tabular.

- (iii) For a tabular approach, data should be sufficient such that the model never has to extrapolate outside of the defined range. In the case of strain rate, it is suggested that data up to 2000 s^{-1} is included. In the case of temperature, the peak temperatures predicted by the model will depend upon process parameters. Generally however, 1300°C should certainly be an acceptable upper limit for the datasets for Ti-6Al-4V.
- (iv) Meshing strategies should be tailored according to the desired modelling outputs. If accurate material flow behaviour is required, and as such flash morphology is considered important, then a fine mesh at the weld line is recommended, with elements potentially as small as $0.1\text{--}0.2 \text{ mm}$ edge length. If thermal and upset results only are important, then potentially the weld line elements can be larger.

Conflict of Interests

The authors declare that there is no conflict of interests regarding the publication of this paper.

References

- [1] J. C. Williams and E. A. Starke Jr, "Progress in structural materials for aerospace systems," *Acta Materialia*, vol. 51, no. 19, pp. 5775–5799, 2003.
- [2] P. Wanjara and M. Jahazi, "Linear friction welding of Ti-6Al-4V: processing, microstructure, and mechanical-property inter-relationships," *Metallurgical and Materials Transactions A*, vol. 36, no. 8, pp. 2149–2164, 2005.
- [3] A. Vairis and M. Frost, "High frequency linear friction welding of a titanium alloy," *Wear*, vol. 217, no. 1, pp. 117–131, 1998.
- [4] M. E. Nunn, "Aero-engine improvements through linear friction welding," in *Proceedings of the 1st International Conference on Innovation and Integration in Aerospace Sciences*, Queen's University Belfast, Northern Ireland, UK, 2005.
- [5] A. Vairis and M. Frost, "Modelling the linear friction welding of titanium blocks," *Materials Science and Engineering A*, vol. 292, no. 1, pp. 8–17, 2000.
- [6] W.-Y. Li, T. Ma, and J. Li, "Numerical simulation of linear friction welding of titanium alloy: effects of processing parameters," *Materials & Design*, vol. 31, no. 3, pp. 1497–1507, 2010.
- [7] W. Li, S. Shi, F. Wang, Z. Zhang, T. Ma, and J. Li, "Numerical simulation of friction welding processes based on ABAQUS environment," *Journal of Engineering Science and Technology Review*, vol. 5, no. 3, pp. 10–19, 2012.
- [8] W. Y. Li, S. X. Shi, F. F. Wang, T. J. Ma, D. Guo, and A. Vairis, "Heat reflux in flash and its effect on joint temperature history during linear friction welding of steel," *International Journal of Thermal Sciences*, vol. 67, pp. 192–199, 2013.
- [9] L. Fratini, G. Buffa, D. Campanella, and D. La Spisa, "Investigations on the linear friction welding process through numerical simulations and experiments," *Materials & Design*, vol. 40, pp. 285–291, 2012.
- [10] E. Ceretti, L. Fratini, C. Giardini, and D. La Spisa, "Numerical modelling of the linear friction welding process," *International Journal of Material Forming*, vol. 3, no. 1, pp. 1015–1018, 2010.
- [11] L. Fratini and D. la Spisa, "Numerical simulation of Linear Friction Welding (LFW) processes," in *Proceedings of the 14th International Conference on Material Forming (ESAFORM '11)*, vol. 1353 of *AIP Conference Proceedings*, pp. 1284–1289, Belfast, UK, April 2011.
- [12] J. Sorina-Müller, M. Rettenmayr, D. Schneefeld, O. Roder, and W. Fried, "FEM simulation of the linear friction welding of titanium alloys," *Computational Materials Science*, vol. 48, no. 4, pp. 749–758, 2010.
- [13] R. Turner, R. M. Ward, R. March, and R. C. Reed, "The magnitude and origin of residual stress in Ti-6Al-4V linear friction welds: an investigation by validated numerical modeling," *Metallurgical and Materials Transactions B*, vol. 43, no. 1, pp. 186–197, 2012.
- [14] F. Schroeder, R. M. Ward, R. Turner, M. M. Attallah, J.-C. Gebelin, and R. C. Reed, "Linear friction welding of titanium alloys for aeroengine applications: modelling and validation," in *Proceedings of the 9th International Trends in Welding Research Conference*, 2012.
- [15] S. K. Kiselyeva, A. M. Yamileva, M. K. Karavaeva et al., "Computer modelling of linear friction welding based on the joint microstructure," *Journal of Engineering Science and Technology Review*, vol. 5, no. 3, pp. 44–47, 2012.
- [16] O. Grong, *Metallurgical Modelling of Welding*, Cambridge University Press, Cambridge, UK, 1994.
- [17] K. C. Mills, *Recommended Values of Thermophysical Properties for Selected Commercial Alloys*, NPL, Woodhead, 2002.
- [18] Z. Guo, R. Turner, A. da Silva et al., "Introduction of materials modelling into processing simulation," *Materials Science Forum*, vol. 762, pp. 266–276, 2013.
- [19] S. Zharebtsov, G. Salishchev, R. Galeyev, and K. Maekawa, "Mechanical properties of Ti-6Al-4V titanium alloy with sub-microcrystalline structure produced by severe plastic deformation," *Materials Transactions*, vol. 46, no. 9, pp. 2020–2025, 2005.

Research Article

Mechanical Behaviors of Friction Stir Spot Welded Joints of Dissimilar Ferrous Alloys under Opening-Dominant Combined Loads

Md. Abu Mowazzem Hossain,¹ Md. Tariqul Hasan,¹ Sung-Tae Hong,¹
Michael Miles,² Hoon-Hwe Cho,³ and Heung Nam Han³

¹ School of Mechanical Engineering, University of Ulsan, Ulsan 680-749, Republic of Korea

² Department of Manufacturing Engineering Technology, Brigham Young University, Provo, UT 84602-9601, USA

³ Department of Materials Science & Engineering and Center for Iron & Steel Research, RIAM, Seoul National University, Seoul 151-744, Republic of Korea

Correspondence should be addressed to Sung-Tae Hong; sthong@ulsan.ac.kr

Received 9 December 2013; Accepted 19 December 2013; Published 29 January 2014

Academic Editor: Wenya Li

Copyright © 2014 Md. Abu Mowazzem Hossain et al. This is an open access article distributed under the Creative Commons Attribution License, which permits unrestricted use, distribution, and reproduction in any medium, provided the original work is properly cited.

Mechanical properties and failure behaviors of friction stir spot welded (FSSW) joints of two dissimilar ferrous alloys, cold-rolled carbon steel (SPCC) and 409L stainless steel (SUS 409L), are investigated under opening-dominant combined loads. The texture of dissimilar FSSW joints depends on the upper sheet material. The failure contours for the FSSW joints under combined loads are constructed in terms of the axial load and shear load by modifying existing failure criteria for resistance spot welds. The shape of the failure contour also depends on the upper sheet material. The failure contours are nearly elliptic in shape when the upper sheet is SPCC and are relatively straight lines when the upper sheet is SUS 409L.

1. Introduction

Friction stir spot welding (FSSW) is a solid-state joining process that originated from friction stir welding (FSW), a technique patented in 1991 by TWI [1]. Compared with conventional resistance spot welding (RSW), FSSW provides several technical advantages including low energy requirements, fewer problems related to cracking and porosity, less residual stress, and a smaller heat affected zone (HAZ) [2, 3]. Also, an additional interesting technical advantage over conventional RSW is that FSSW can easily join dissimilar metal alloys.

Even though RSW has been the technique most commonly used in the automotive industries for joining ferrous alloys, RSW is also known to be problematic for several specific ferrous alloys [4]. Moreover, the use of dissimilar ferrous alloys is increasing in the automotive industry to improve the crashworthiness of the automobile structure without significantly increasing weight and manufacturing cost. It is clear that RSW of dissimilar ferrous alloys can be extremely

difficult due to the different physical, chemical, and mechanical properties of the base metals [5].

Due to FSSW's technical advantages, including its ability to join dissimilar alloys easily, interest has increased in FSSW as a substitute for RSW in joining similar or dissimilar ferrous alloys in automotive applications. However, even though many pioneering works on FSSW of ferrous alloys have been conducted over the last decade, substituting FSSW for the RSW commonly used in automotive applications will require further investigation. Feng et al. [6] performed an introductory study that examined the feasibility of FSSW of AHSS steel; this study suggested that the mechanical strength of the FSSW joint improves as the width of the bonding ligament increases. Baek et al. [7] examined the effect of tool penetration depth on the microstructures and mechanical properties of FSSW joints of low-carbon steel. Their results showed that the tensile shear strength of low-carbon steel FSSW joint increases as the tool penetration depth increases. Hovanski et al. [8] investigated the microstructure and mechanical

properties of FSSW joints of hot-stamped boron steel, as well as their failure mechanism: cracking initiated at the interface of the upper and lower sheets and then propagated along the thin ferritic region within weld nugget. Miles et al. [9] investigated the effect of tool wear on joint strength using tools composed of polycrystalline cubic boron nitride (PCBN) and tungsten rhenium (W-Re), where tools with a greater proportion of PCBN were found to provide the best combination of joint strength and wear resistance. Sun et al. [10] experimentally investigated the failure behavior of FSSW joints of mild steel, suggesting based on the result of shear tensile tests, that FSSW joints undergoing fracture by the plug failure mode have higher shear tensile strength compared to FSSW joints undergoing fracture by the interfacial failure mode.

A critical mechanical property of a joint in an automobile body structure is its failure behavior. For RSW, research has been conducted on joint failure, including the development of different fracture models formulated in terms of the local loads acting on the spot welds, as well as in terms of the appropriate strengths of the weld. Chao [11] developed a failure criterion for spot welds and performed strength tests using cross tension and lap shear samples made of high-strength steel. Wung [12] and Wung et al. [13] investigated the failure of spot welds under in-plane torsion and proposed a force-based failure criterion. Radaj [14], Radaj and Zhang [15], and Zhang [16] adopted a fracture mechanics approach and provided a very detailed description of the stress distribution around a weld nugget. Radaj [14] showed that the fatigue strength of spot-welded joints can be assessed on the basis of the local stress state at the weld spot edge. Radaj and Zhang [15] developed the relations between notch stress and crack stress intensity in the case of plane shear loading (mode II) for the elliptical hole and the blunt crack. Zhang [16] derived approximate stress formulas of structural stress and notch stress for a newly proposed multiaxial spot weld specimen that enables a spot weld to be tested under combined loads ranging from pure shear to pure tension.

The failure behavior of RSW joints under combined or multiaxial loads also has been investigated by many researchers. The failure behavior of a joint under combined loads is typically important in the structural durability and crash safety of the automobile structure. Lee et al. [17] performed a failure test of RSW joints in U-shaped specimens under combined shear and tension loads and proposed an ultimate strength model to fit their experimental results. Lin et al. [18, 19] analyzed the failure mechanism of spot welds in square-cup specimens made from mild steel and HSLA steel under combined loads. They proposed a quadratic-form engineering failure criterion in terms of the normalized axial and shear loads with consideration of the sheet thickness and the nugget radius under combined loads. More recently, a different failure criterion in terms of the axial and shear loads has been suggested by Song and Huh [20] to predict the failure behavior of RSW joints.

However, the failure behavior of FSSW joints under combined or multiaxial loads has been rarely investigated until recently, even though the failure behavior of FSSW joints can differ from that of RSW joints [21] due to the different joining

TABLE 1: The chemical compositions provided by the manufacturer and mechanical properties of SPCC and SUS 409L.

(a)									
Chemical compositions (wt%)									
	C	Mn	P	Si	S	S-AL	Fe		
SPCC	0.0361	0.205	0.015	0.019	0.006	0.037	At balance		
(b)									
Chemical compositions (wt%)									
	C	Cr	Mn	P	Si	S	Ni	Ti	Fe
SUS 409L	≤0.03	11.44	≤1.0	≤0.04	≤1.0	≤0.03	≤0.08	≤0.75	At balance
(c)									
Mechanical properties									
	Tensile strength (MPa)		Yield strength (MPa)		Elongation at fracture (%)				
SPCC	316.8		163.8		46				
SUS 409L	494		236		36				

mechanisms of FSSW and RSW. In the present study, the failure behavior of FSSW joints of two dissimilar ferrous alloys under opening-dominant combined loads was investigated experimentally. Based on the experimental result, failure contours for the FSSW joints were constructed in terms of the axial and shear loads. A failure criterion, which was originally developed for RSW joints, was then modified to describe the experimental failure contours of the FSSW joints.

2. Experimental

The two dissimilar ferrous alloys used in the present study were 1.2 mm thick steel sheets of cold-rolled carbon steel (SPCC) and 409L stainless steel (SUS); Table 1 lists the nominal chemical compositions and mechanical properties of these alloys. Cross-sectional samples for microstructure analysis were first prepared from FSSW joints of four different material combinations. The welding was carried out using a convex scrolled shoulder tool made of polycrystalline cubic boron nitride (PCBN)-based composite. The process parameters and tool geometry used to fabricate the FSSW joints are listed in Table 2. During the FSSW process, an argon shroud was introduced using a gas cup located around the tool to minimize the surface oxidation of the joint. The samples were mechanically ground and electrolytically polished in a solution of 10 mL perchloric acid + 90 mL ethanol using a Struers Lectropol-5 electrolytic polisher. High-resolution EBSD studies were performed using a Jeol JSM6500F FE-SEM equipped with an HKL Channel 5 EBSD system. The accelerating voltage was 20 kV, the probe current was 4 nA, and the working distance was 15 mm, with the sample stage tilted by 70°. The camera resolution was 1000 × 800 pixels in the operation of 8 × 8 binning. The mapping grid was a regular square with 0.7 μm steps. The limits of the low-angle

TABLE 2: Friction stir spot welding parameters and tool geometry used in the experiments.

Rotation (rpm)	Process parameters				Tool geometry		
	Plunging rate (mm/min)	Depth (mm)	Control mode	Dwell time (sec)	Shoulder diameter (mm)	Pin diameter (mm)	Pin length (mm)
1400	8	1.45	Servo control	2	36.8	5.7	1

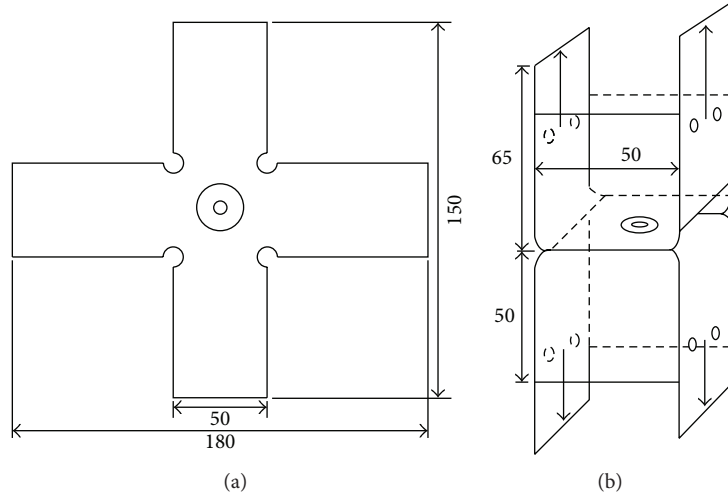


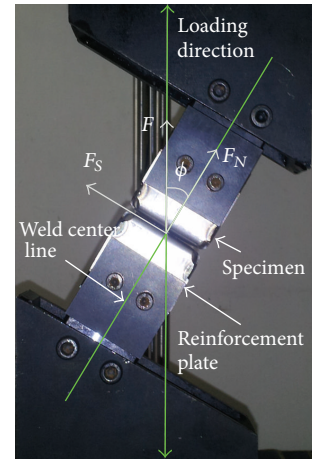
FIGURE 1: Schematics of fabricated and welded specimens: (a) top view of unfolded square-cup specimen and (b) folded square-cup specimen with FSSW (dimensions in mm).

boundaries (LABs) and high-angle boundaries (HABs) were, respectively, set to 2° and 15° . The grain size was measured using the linear intercept method. The hardness profiles in the stir zone and surrounding regions of the FSSW joints were also measured as a function of distance from the weld center.

Square-cup specimens made of SPCC and 409L SUS were then fabricated; these specimens were then friction stir spot welded as depicted schematically in Figure 1, with four different material combinations: SPCC/SPCC, SPCC (top)/SUS (bottom), SUS (top)/SPCC (bottom), and SUS/SUS. Once again, the welding was carried out using a convex scrolled shoulder tool made of PCBN-based composite with the process parameters listed in Table 2. Note that the four corners of each square-cup specimen were arc-welded to ensure adequate stiffness of the cup specimen under opening-dominant combined loads and to guarantee a relatively uniform loading along the circumference of spot weld.

In order to impose a combined load on the FSSW joint, four fixture sets were designed with different inclined loading angles ϕ of 0° , 15° , 22° , and 30° (Figure 2), where ϕ is the angle between the load application line and the center line of the FSSW joint. In each experimental setup, the welded square-cup specimens were mounted to the fixture set by means of bolts through the specimen holes. The reinforcement plates were attached to the specimen to prevent plastic deformation near the specimen holes during loading. Using the inclined loading angle ϕ , the applied load F can be simply decomposed into the axial load F_N and the shear load F_S as

$$\begin{aligned} F_N &= F \cos \phi, \\ F_S &= F \sin \phi. \end{aligned} \quad (1)$$

FIGURE 2: Experimental setup for $\phi = 30^\circ$.

Quasi-static tests of the FSSW joints under combined loads were conducted using a universal testing machine with a displacement rate of 2 mm/min along the load application line. During each test the load and displacement were recorded as functions of time. In general, the test was terminated when the FSSW joint was completely separated. The cross section through the weld center of each failed FSSW joint was examined using an optical microscope to understand the failure behavior for each loading condition.

3. Results and Discussion

3.1. Microstructures. FSSW joints without visible macroscopic defects were successfully produced with the selected

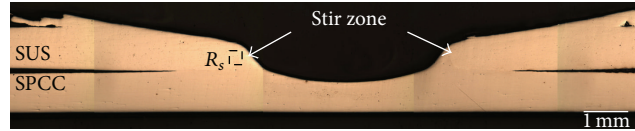
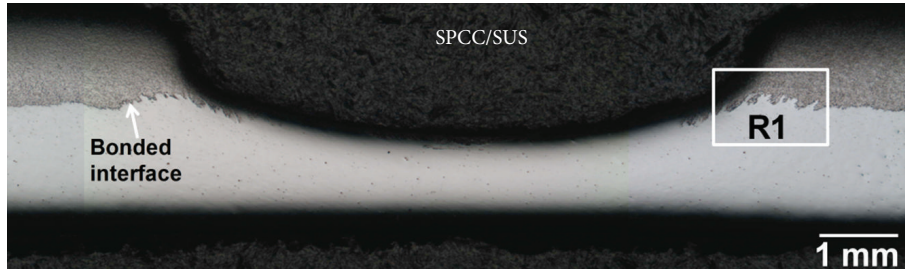
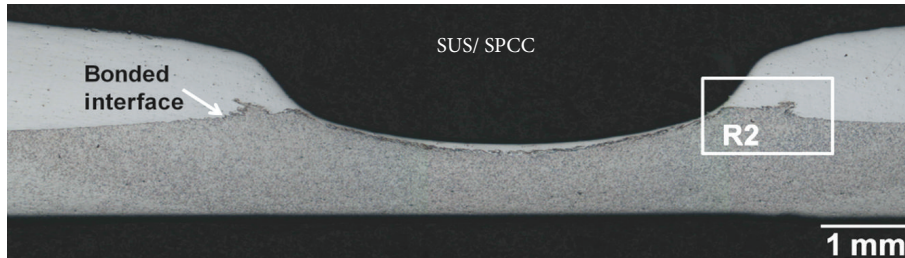


FIGURE 3: A cross-sectional macrograph of a SUS/SPCC FSSW joint.



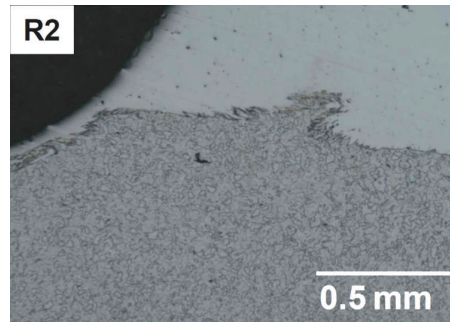
(a)



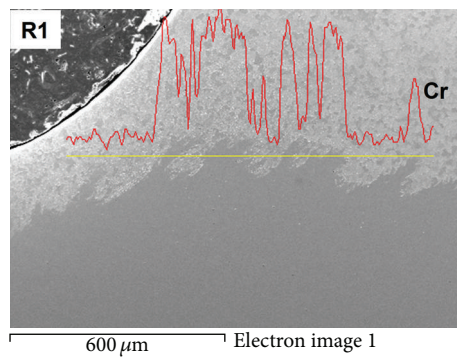
(b)



(c)



(d)



(e)

FIGURE 4: Optical micrographs of (a) SPCC/SUS and (b) SUS/SPCC FSSW joints; (c) region R1 in (a) and (d) region R2 in (b); (e) Cr distribution profile in region R1 [21].

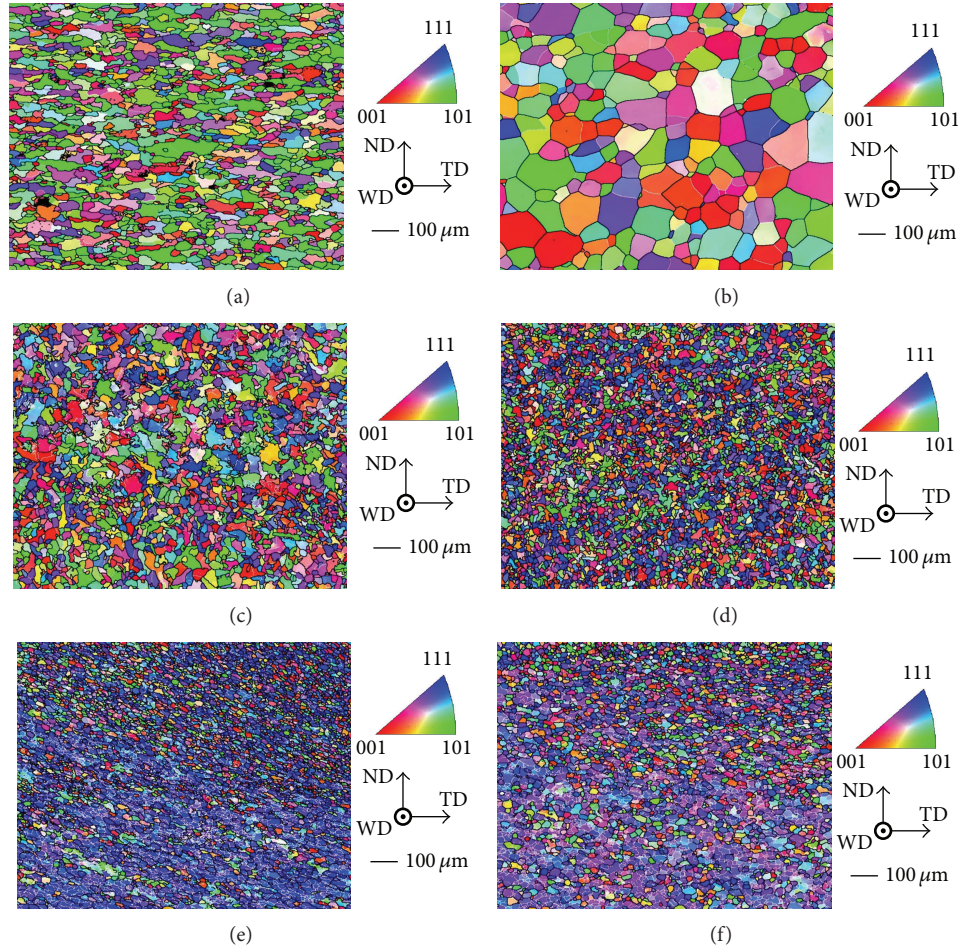


FIGURE 5: Orientation maps of the base material in (a) SPCC and (b) SUS and the stir zone in (c) SPCC/SPCC, (d) SPCC/SUS, (e) SUS/SPCC, and (f) SUS/SUS, respectively; WD, TD, and ND, respectively, correspond to the welding, transversal, and normal directions.

process parameters for all four material combinations studied, as evidenced by a representative cross-sectional macrograph of SUS/SPCC FSSW joint in Figure 3 [21]. The indentation profile of the joint reflects the shape of the pin and the convex shoulder of the tool. The surface of the tool was examined visually after each weld. There was no significant tool wear observed throughout the entire set of experiments conducted for the present study.

The mixing of materials in the stir zone of dissimilar FSSW joints (SPCC/SUS and SUS/SPCC) was already presented in our previous study [21]. We present the mixing of materials in the stir zone here once again just for the completeness of the study. The mixing of materials in the stir zone of dissimilar FSSW joints depends on the material combination (Figures 4(a) and 4(b)) [21]. For the SPCC/SUS FSSW joint, the lower SUS sheet material was pulled upward and mixed into the upper SPCC sheet material as layers (Figure 4(c)). On the other hand, for the SUS/SPCC FSSW joint, a small portion of SPCC in the lower sheet was pulled upward into the SUS in the upper sheet and relatively little mechanical mixing occurred between the SPCC and the SUS (Figure 4(d)). The result of a line scan of the Cr content along

the interface of the region R1 confirms the mechanical mixing between the SPCC and SUS as shown in Figure 4(e).

The orientation maps of the stir zone underneath the root of the pin (R_s in Figure 3 and similar locations for FSSW joints of other material combinations) show that considerably finer homogeneous grains developed in the stir zone in comparison with the base materials as shown in Figures 5(a)–5(f). The average grain size of the base material was approximately $13.2\ \mu\text{m}$ for SPCC and $27.4\ \mu\text{m}$ for SUS. Note that the grain sizes of the stir zone differed somewhat among the four different material combinations. The average grain size of the stir zone of the SPCC/SPCC joint, $10.74\ \mu\text{m}$, was somewhat larger than that of the SUS/SUS joint, $6.89\ \mu\text{m}$. This may be explained by the different phase transformation temperatures of the base materials. A further discussion on the phase transformation of the base materials during FSSW is beyond the scope of the present study and will be discussed elsewhere.

It is interesting to note that the texture of dissimilar FSSW joints strongly depends on the upper sheet material. Even though the $8.76\ \mu\text{m}$ average grain size of the SPCC/SUS joint is only slightly larger than that of the SUS/SPCC joint, $8.39\ \mu\text{m}$, as shown in Figures 5(e) and 5(f), the texture of the

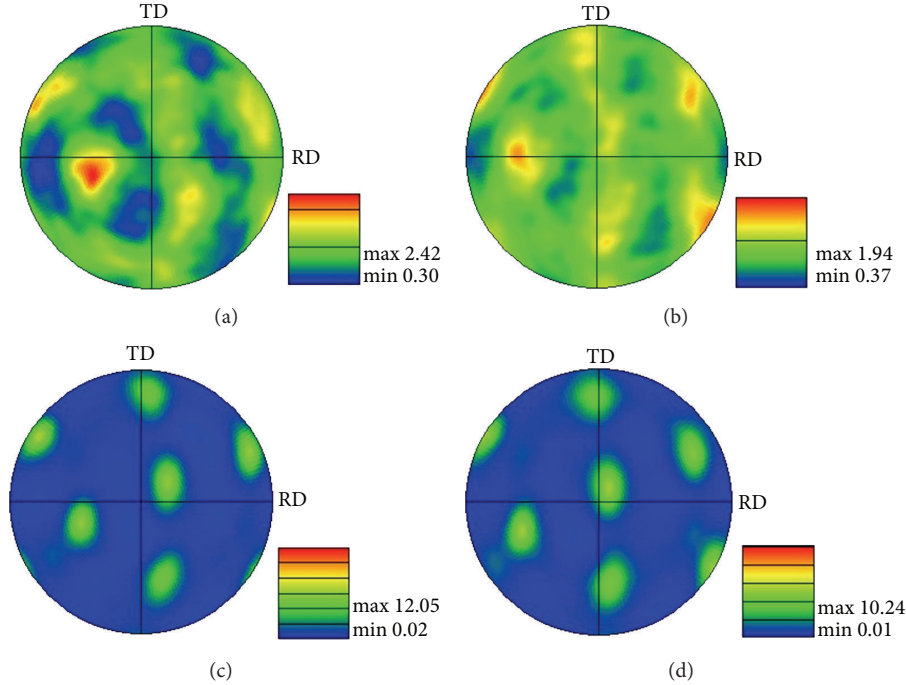


FIGURE 6: Pole figures of the stir zone in (a) SPCC/SPCC, (b) SPCC/SUS, (c) SUS/SPCC, and (d) SUS/SUS, respectively; RD and TD correspond to rolling and transversal directions, respectively.

stir zone of the SPCC/SUS joint is almost random (a very weak shear texture) and differs considerably from that of the SUS/SPCC joint as shown in Figures 6(b) and 6(d). In the stir zone of the SUS/SPCC joint, a clear shear texture developed, similar to the texture of the SUS/SUS joint as shown in Figures 6(c) and 6(d). The dependence of the microstructural characteristics on the upper sheet material is probably due to that only the upper sheet material contacts the tool directly during most of the FSSW process.

Hardness profiles were made with a spacing of 0.3 mm along three parallel lines: two lines in the upper sheet and one line in the lower sheet (Figure 7(a)); these profiles were collected for FSSW joints of each of the four material combinations tested (Figures 7(b)–7(e)). The hardness profiles in Figures 7(b)–7(e) show typical hardness distributions across the base metal, the heat affected zone (HAZ), and the stir zone. The hardness of the stir zone is generally higher than that of the base metal for both SPCC and SUS due to the large plastic deformation and fine-grained microstructure in the stir zone [22]; a slight decrease of the hardness in the HAZ is also observed.

3.2. Mechanical Behavior under Combined Loads. Load-displacement curves for FSSW joints of four different material combinations at four different loading angles clearly show that the maximum failure load and toughness of the joints depend on the material combinations and loading angles (Figure 8); the maximum load decreases as the loading angle increases for all material combinations studied as listed in Table 3. This tendency of the maximum load is similar to that

TABLE 3: The quasi-static failure loads of the FSSW joints under various loading conditions.

Loading angle (°)	Maximum load* (kN)			
	SPCC/SPCC	SPCC/SUS	SUS/SPCC	SUS/SUS
0	7.81 (0.095)	8.42 (0.060)	8.60 (0.230)	10.00 (0.201)
15	7.70 (0.032)	7.75 (0.008)	6.54 (0.183)	8.81 (0.283)
22	7.40 (0.077)	7.60 (0.062)	6.43 (0.220)	8.43 (0.092)
30	6.93 (0.060)	7.40 (0.073)	6.10 (0.090)	8.30 (0.052)

* Average of the results of two FSSW specimens; values in the parentheses are the standard deviations.

observed in RSW experiments reported by Lin et al. [18] and Song and Huh [20].

Under a pure opening load ($\phi = 0^\circ$), failure occurred by a typical nugget pullout mode. By contrast, under a combined load, the joint's failure initiated with a nugget rotation due to the shear component of the combined load, followed by complete separation of the upper sheet by tearing off from the joint. A comparison of the top and bottom views of the completely separated SPCC/SPCC FSSW joints under a pure opening load ($\phi = 0^\circ$, Figures 9(a) and 9(b)) and a combined load of $\phi = 30^\circ$ (Figures 9(c) and 9(d)) shows that nugget rotation occurred under the combined load (Figures 9(c) and 9(d)), while a typical nugget pullout fracture occurred under the pure opening load (Figures 9(a) and 9(b)). As shown in Figure 9(d), the upper sheet was torn off at the final stage of the failure as the rupture propagated along the circumference of the nugget. A similar failure mechanism was observed for

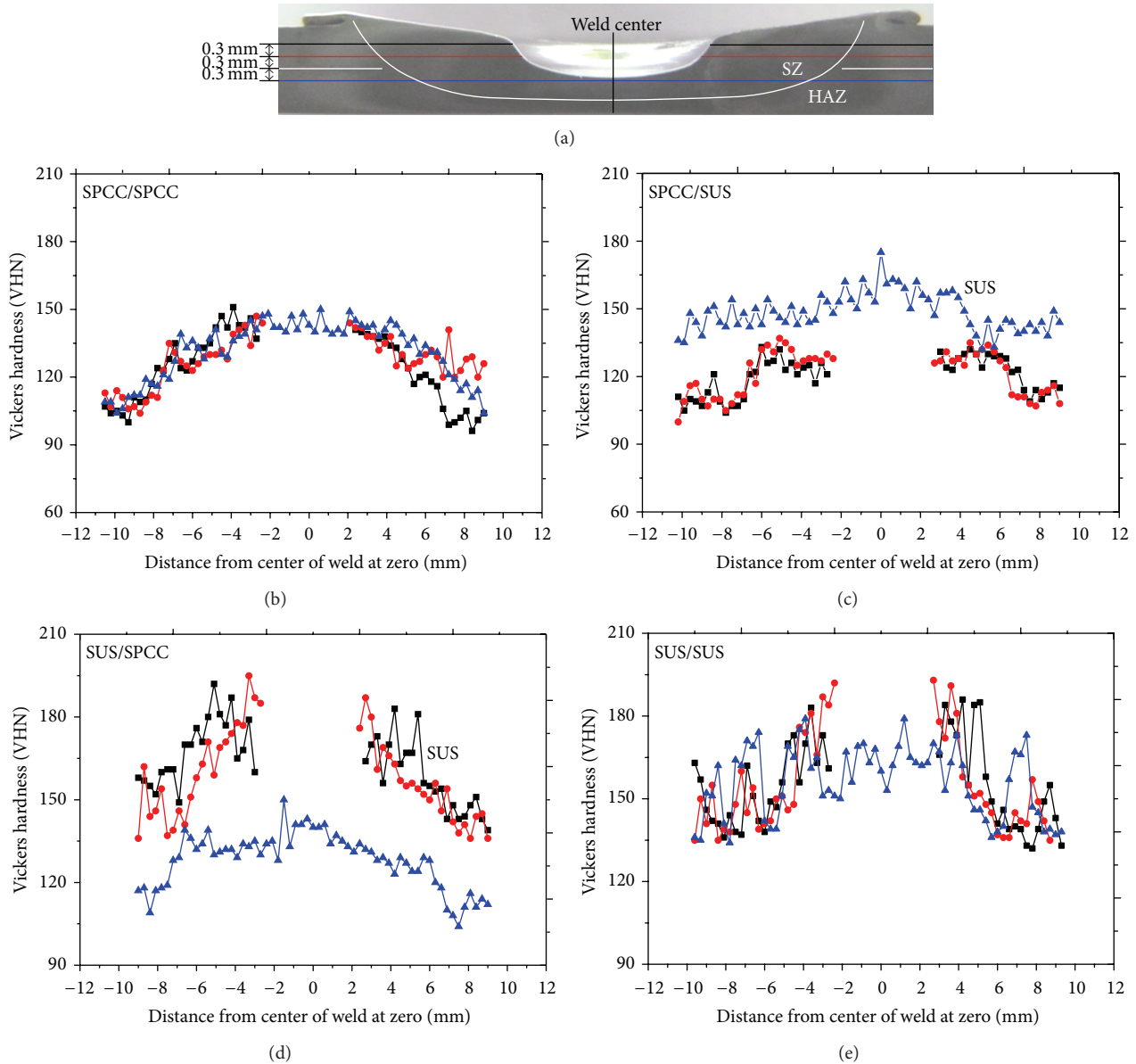


FIGURE 7: (a) Locations of the three parallel hardness traverses for a SPCC/SPCC joint; hardness profiles of FSSW joint cross sections, showing typical hardness distributions across the base metal, the HAZ, and the stir zone: (b) SPCC/SPCC, (c) SPCC/SUS, (d) SUS/SPCC, and (e) SUS/SUS.

RSW by Lin et al. [18], Song and Huh [20], and Song et al. [23].

The cross-sectional optical micrograph of a completely failed SPCC/SPCC FSSW joint under a pure opening load ($\phi = 0^\circ$) shows that the typical nugget pullout failure occurred by uniform necking/shear along the circumferential boundary of the nugget as shown in Figure 10(a). The cross-sectional optical micrograph of a completely failed FSSW joint under a combined load of $\phi = 22^\circ$ (Figure 10(b)) shows that the failure of the joint under a combined load was initiated by necking and shear at the stretching side with respect to the shear component of the load (marked as A in Figure 10(b)), even though signs of necking are also observed on the opposite side. The rupture then propagated along the

circumference of the weld nugget. Finally, the upper sheet was completely torn off from the lower sheet at nearly the opposite side from the location where the rupture initiated (marked as B in Figure 10(b)). The failures of FSSW joints for the material combinations of SPCC/SUS, SUS/SPCC, and SUS/SUS and at different combined loading angles $\phi = 15^\circ$ and 30° were quite similar to the result shown in Figure 10 and not shown here.

The maximum loads under combined loads were simply decomposed into the axial and shear components using (1) for the four different material combinations. A failure contour then can be constructed in terms of the axial and shear load. Several failure criteria have been proposed to describe the failure of RSW under combined loads. Lee et al. [17] proposed

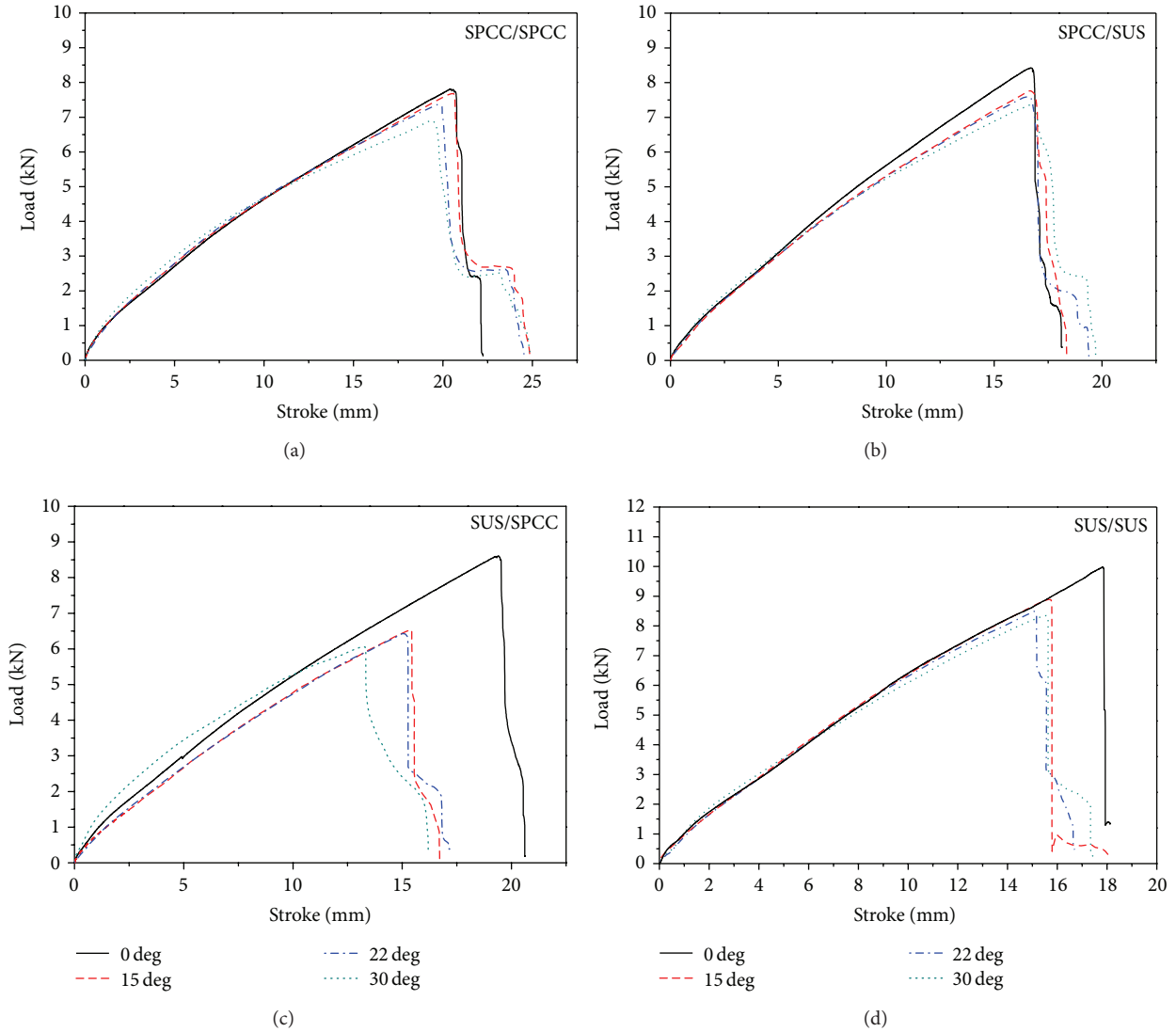


FIGURE 8: Load-displacement curves for FSW joints of (a) SPCC/SPCC, (b) SPCC/SUS, (c) SUS/SPCC, and (d) SUS/SUS at four different loading angles.

a failure criterion based on the normal and shear failure loads of the weld, which were determined under pure opening and shear loads, respectively. Under combined loads, they proposed the following failure criterion:

$$\left(\frac{F_n}{F_N}\right)^n + \left(\frac{F_s}{F_S}\right)^n = 1, \quad (2)$$

where F_n and F_s are the applied normal and shear loads, respectively, F_N and F_S are the normal and shear failure loads of the spot weld, respectively, and n is the fitting parameter. In general, n is set to 2 to fit the experimental results.

Lin et al. [18] proposed an engineering failure criterion in terms of the axial and shear loads with consideration of the sheet thickness and the nugget radius under combined loads.

Their failure criterion, based on the lower bound analysis under combined opening and shear loads, is expressed as

$$\begin{aligned} & [1 - 2\alpha + 2\alpha^2] \left(\frac{F_n}{2\pi r t \tau_0}\right)^2 \\ & + \left[\frac{1}{3} + \left(\frac{4t}{2\pi r}\right)\right] \left(k \frac{F_s}{2\pi r t \tau_0}\right)^2 = 1, \end{aligned} \quad (3)$$

where τ_0 is the shear yield strength, α is the loading parameter, and k is the fitting constant. For a combined load, $\alpha = 0.5$ is used for square-cup specimens [18].

Recently, Song and Huh [20] also proposed a failure criterion to describe the failure behavior of RSW joints under combined loads:

$$\left(\frac{F_n}{F_N}\right)^2 + \beta \left(\frac{F_n}{F_N}\right) \left(\frac{F_s}{F_S}\right) + \left(\frac{F_s}{F_S}\right)^2 = 1. \quad (4)$$

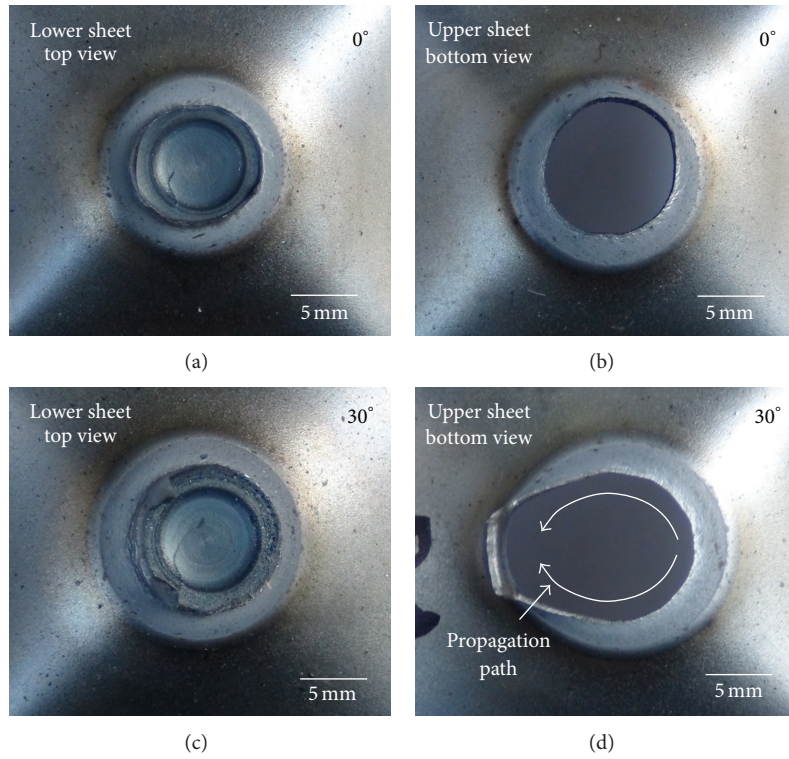


FIGURE 9: Top and bottom views of the completely separated SPCC/SPCC FSSW joints under ((a), (b)) a pure opening load ($\phi = 0^\circ$) and ((c), (d)) a combined load of $\phi = 30^\circ$, respectively.

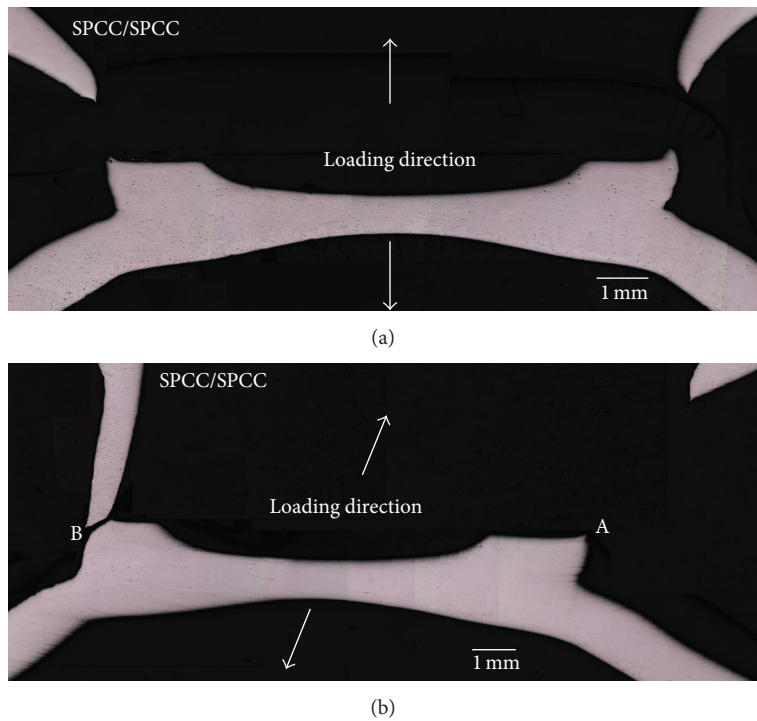


FIGURE 10: Cross-sectional macrographs of completely failed SPCC/SPCC FSSW joints under (a) a pure opening load ($\phi = 0^\circ$) and (b) a combined load of $\phi = 22^\circ$, respectively.

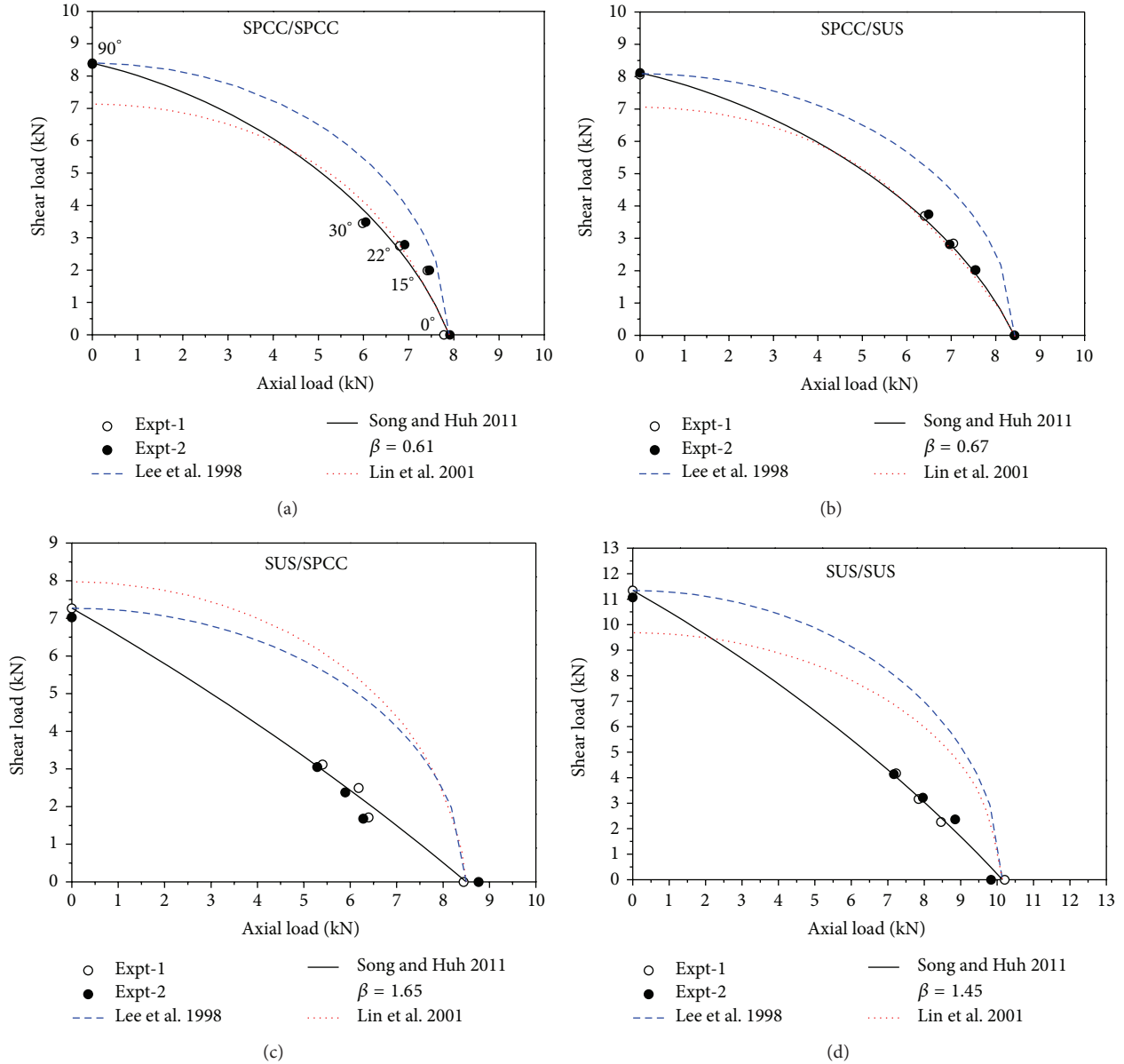


FIGURE 11: Comparison of the experimental result with conventional failure criteria: (a) SPCC/SPCC, (b) SPCC/SUS, (c) SUS/SPCC, and (d) SUS/SUS.

Here, again, F_N and F_S are the normal and shear failure loads of the spot weld, respectively. The variable β is the failure parameter that can be obtained by least-squares fitting to minimize the discrepancy between the experimental result and the interpolated one. The shape of the failure curve is elliptic when $\beta = 0$, and in this condition is identical to the failure criterion proposed by Lee et al. [17].

Based on the experimental results and above mentioned failure criteria, failure contours for FSSW joints under combined loads were constructed in terms of the axial and shear loads for each of the four different material combinations (Figure 11). Note that in constructing the failure contours, the experimental result of lap-shear specimens [21] was used as the shear failure load F_S . Also note that for the failure

contours of dissimilar FSSW joints based on (3), the shear yield strength of the upper sheet material was used since the fracture mainly occurred in the upper sheet material. Comparison of the failure contours suggests that the failure criterion proposed by Lee et al. [17] is inadequate to describe the failure of FSSW joints under opening-dominant combined loads. Although the experimental result of FSSW joints with SPCC on the upper sheet (Figures 11(a)-11(b)) is relatively consistent with the failure criterion suggested by Lin et al. [18], the experimental result of FSSW joints with SUS on the upper sheet (Figures 11(c)-11(d)) does not agree well with that criterion. On the other hand, the experimental results for all four different material combinations can agree well with the failure criterion proposed by Song and Huh [20] by selecting

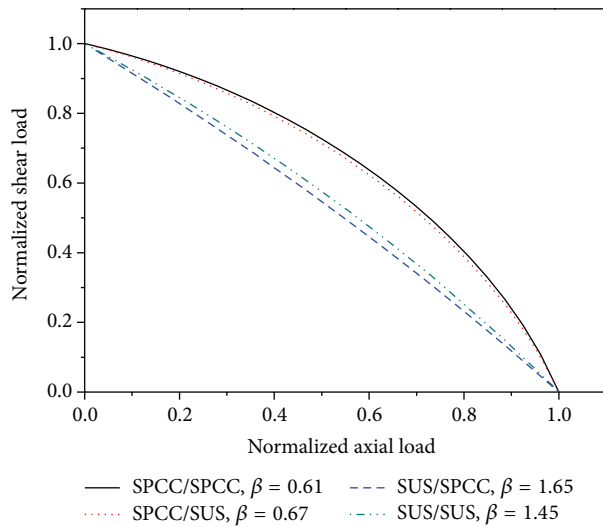


FIGURE 12: Normalized failure contours for the FSSW joints with four different material combinations based on the failure criterion of Song and Huh [20].

different values of β . It is interesting to note that the value of β strongly depends on the material on the upper sheet of the joint; the FSSW joints with a softer and more ductile material on the upper sheet (SPCC/SPCC and SPCC/SUS) have considerably lower values of β . Actually, comparison of the failure contours based on Song and Huh [20] in terms of the normalized axial and shear loads, which were normalized by the corresponding normal (pure opening, $\phi = 0^\circ$) and shear ($\phi = 90^\circ$) failure loads, respectively, confirms the dependence of the failure contours on the upper sheet material (Figure 12). The shape of the failure contours is close to elliptic with SPCC as the upper sheet, while the failure contours take the form of a relatively straight line with SUS as the upper sheet.

4. Conclusions

Mechanical behaviors of FSSW joints of two dissimilar ferrous alloys under opening-dominant combined loads were experimentally investigated. Defect-free spot joints were successfully fabricated with four different material combinations. EBSD analysis shows that extremely fine homogeneous grains developed in the stir zone, while the texture of dissimilar FSSW joints depends on the upper sheet material. The failure contours for the FSSW joints under combined loads were constructed in terms of the axial load and shear load by modifying existing failure criteria for RSW. The shape of the failure contour also depends on the upper sheet material. The failure contours are nearly elliptic in shape when the upper sheet is SPCC and are relatively straight lines when the upper sheet is SUS. The results of the present study also suggest that the mechanical and material properties of FSSW joints of dissimilar ferrous alloys are improved when the lap joint is designed with the “harder” material on the bottom and the “softer” material on top.

Conflict of Interests

The authors declare that there is no conflict of interests regarding the publication of this paper.

Acknowledgments

This research was financially supported by the Ministry of Education (MOE) and National Research Foundation of Korea (NRF) through the Human Resource Training Project for Regional Innovation. Michael Miles acknowledges support from National Science Foundation Grant CMMI-1131203. H.-H. Cho and H. N. Han were supported by Basic Science Research Program through the National Research Foundation of Korea (NRF) and funded by the Ministry of Science, ICT, and Future Planning (2013008806).

References

- [1] W. M. Thomas, E. D. Nicholas, J. C. Needham, P. Temple-smith, S. W. K. W. Kallee, and C. J. Dawes, “Friction stir welding,” UK Patent Application GB 2 306 366 A, 1991.
- [2] W. Yuan, R. S. Mishra, S. Webb et al., “Effect of tool design and process parameters on properties of Al alloy 6016 friction stir spot welds,” *Journal of Materials Processing Technology*, vol. 211, no. 6, pp. 972–977, 2011.
- [3] D.-A. Wang and S.-C. Lee, “Microstructures and failure mechanisms of friction stir spot welds of aluminum 6061-T6 sheets,” *Journal of Materials Processing Technology*, vol. 186, no. 1-3, pp. 291–297, 2007.
- [4] E. Folkhard, *Welding Metallurgy of Stainless Steels*, Springer, New York, NY, USA, 1988.
- [5] O. P. Khanna, *Welding Technology*, Dhanpat Rai Publications, New Delhi, India, 16th edition, 2007.
- [6] Z. Feng, M. L. Santella, S. A. David et al., “Friction Stir Spot Welding of Advanced High-Strength Steels -A Feasibility Study,” SAE World Congress, Detroit, Mich, USA, 2005.
- [7] S. W. Baek, D.-H. Choi, C.-Y. Lee et al., “Structure-properties relations in friction stir spot welded low carbon steel sheets for light weight automobile body,” *Materials Transactions*, vol. 51, no. 2, pp. 399–403, 2010.
- [8] Y. Hovanski, M. L. Santella, and G. J. Grant, “Friction stir spot welding of hot-stamped boron steel,” *Scripta Materialia*, vol. 57, no. 9, pp. 873–876, 2007.
- [9] M. P. Miles, C. S. Ridges, Y. Hovanski, J. Peterson, M. L. Santella, and R. Steel, “Impact of tool wear on joint strength in friction stir spot welding of DP 980 steel,” *Science and Technology of Welding and Joining*, vol. 16, no. 7, pp. 642–647, 2011.
- [10] Y. F. Sun, H. Fujii, N. Takaki, and Y. Okitsu, “Microstructure and mechanical properties of mild steel joints prepared by a flat friction stir spot welding technique,” *Materials and Design*, vol. 37, pp. 384–392, 2012.
- [11] Y. J. Chao, “Ultimate strength and failure mechanism of resistance spot weld subjected to tensile, shear, or combined tensile/shear loads,” *Journal of Engineering Materials and Technology, Transactions of the ASME*, vol. 125, no. 2, pp. 125–132, 2003.
- [12] P. Wung, “A forced-based failure criterion for spot weld design,” *Experimental Mechanics*, vol. 41, no. 1, pp. 107–113, 2001.

- [13] P. Wung, T. Walsh, A. Ourchane, W. Stewart, and M. Jie, "Failure of spot welds under in-plane static loading," *Experimental Mechanics*, vol. 41, no. 1, pp. 100–106, 2001.
- [14] D. Radaj, "Stress singularity, notch stress and structural stress at spot-welded joints," *Engineering Fracture Mechanics*, vol. 34, no. 2, pp. 495–506, 1989.
- [15] D. Radaj and S. Zhang, "On the relations between notch stress and crack stress intensity in plane shear and mixed mode loading," *Engineering Fracture Mechanics*, vol. 44, no. 5, pp. 691–704, 1993.
- [16] S. Zhang, "Approximate stress formulas for a multiaxial spot weld specimen," *Welding Journal*, vol. 80, no. 8, pp. 201s–203s, 2001.
- [17] Y.-L. Lee, T. J. Wehner, M.-W. Lu, T. W. Morrisett, and E. Pakalnins, "Ultimate strength of resistance spot welds subjected to combined tension and shear," *Journal of Testing and Evaluation*, vol. 26, no. 3, pp. 213–219, 1998.
- [18] S.-H. Lin, J. Pan, S.-R. Wu, T. Tyan, and P. Wung, "Failure loads of spot welds under combined opening and shear static loading conditions," *International Journal of Solids and Structures*, vol. 39, no. 1, pp. 19–39, 2001.
- [19] S.-H. Lin, J. Pan, T. Tyan, and P. Prasad, "A general failure criterion for spot welds under combined loading conditions," *International Journal of Solids and Structures*, vol. 40, no. 21, pp. 5539–5564, 2003.
- [20] J. H. Song and H. Huh, "Failure characterization of spot welds under combined axial shear loading conditions," *International Journal of Mechanical Sciences*, vol. 53, no. 7, pp. 513–525, 2011.
- [21] M. A. M. Hossain, M. T. Hasan, S. T. Hong, M. Miles, H. H. Cho, and H. N. Han, "Failure behaviors of friction stir spot welded joints of dissimilar ferrous alloys under quasi-static shear loads," *International Journal of Materials and Product Technology*, vol. 48, no. 1–4, pp. 179–193, 2014.
- [22] Y. Miyano, H. Fujii, Y. Sun, Y. Katada, S. Kuroda, and O. Kamiya, "Mechanical properties of friction stir butt welds of high nitrogen-containing austenitic stainless steel," *Materials Science and Engineering A*, vol. 528, no. 6, pp. 2917–2921, 2011.
- [23] J. H. Song, H. Huh, J. H. Lim, and S. H. Park, "Effect of tensile speed on the failure load of a spot weld under combined loading conditions," *International Journal of Modern Physics B*, vol. 22, no. 9–11, pp. 1469–1474, 2008.

Research Article

Upset Prediction in Friction Welding Using Radial Basis Function Neural Network

Wei Liu,^{1,2} Feifan Wang,³ Xiawei Yang,³ and Wenya Li^{3,4}

¹ State Key Laboratory of Integrated Service Networks, Xidian University, Xi'an, Shaanxi 710071, China

² Department of Physics, Qinghai Normal University, Xining, Qinghai 810008, China

³ State Key Laboratory of Solidification Processing, Northwestern Polytechnical University, Xi'an, Shaanxi 710072, China

⁴ School of Materials Science and Engineering, Northwestern Polytechnical University, Xi'an, Shaanxi 710072, China

Correspondence should be addressed to Wenya Li; liwy@nwpu.edu.cn

Received 18 August 2013; Accepted 9 October 2013

Academic Editor: Achilleas Vairis

Copyright © 2013 Wei Liu et al. This is an open access article distributed under the Creative Commons Attribution License, which permits unrestricted use, distribution, and reproduction in any medium, provided the original work is properly cited.

This paper addresses the upset prediction problem of friction welded joints. Based on finite element simulations of inertia friction welding (IFW), a radial basis function (RBF) neural network was developed initially to predict the final upset for a number of welding parameters. The predicted joint upset by the RBF neural network was compared to validated finite element simulations, producing an error of less than 8.16% which is reasonable. Furthermore, the effects of initial rotational speed and axial pressure on the upset were investigated in relation to energy conversion with the RBF neural network. The developed RBF neural network was also applied to linear friction welding (LFW) and continuous drive friction welding (CDFW). The correlation coefficients of RBF prediction for LFW and CDFW were 0.963 and 0.998, respectively, which further suggest that an RBF neural network is an effective method for upset prediction of friction welded joints.

1. Introduction

Friction welding (FW) is a solid-state joining process where heat is generated directly by mechanical friction between a rotating or oscillating workpiece and a stationary component under pressure. After some time, movement is terminated and softened thermal-plastic material is extruded to form the joint. Due to the advantage of no melting during the FW process, various defects (e.g., hot cracking, porosity, and segregation) inherent in conventional fusion welding processes can be avoided or minimized. FW is now being used with metals and thermoplastics in a wide variety of aviation and automotive applications, and various aspects of research have been done on a large scale, which were reviewed in detail by Maalekian [1].

Although both experimental and FE methods are powerful approaches for the investigation of FW, the ability to perform experiments is seriously limited due to high cost and time required. In addition to these restrictions, it is impossible to experiment with continuously varying processing parameters. Therefore, using the available experimental and

simulated results, further predictions can be made of practical significance for engineering applications.

The Artificial neural network (ANN) is an excellent tool for solving complex engineering problems due to its powerful nonlinear and adaptive nature and self-learning capacity [2]. Originally, ANN attracted the attention of welding researchers and has been primarily employed to predict the weld-bead geometry [3–9], while some researchers have used them to predict joint mechanical properties [10–12]. More recently, applications of ANN in FW have been presented. For example, Okuyucu et al. have proposed a back propagation (BP) algorithm to analyze and simulate the correlation between the FW parameters of aluminum plates and mechanical properties of joints [13]. Sathiya et al. have optimized the welding parameters of FW stainless steel by using a modified ANN technique [14]. Kumaran et al. directly used an ANN-aided external tool to optimize the FW process of tube-to-tube plate [15]. Boldsai Khan et al. introduced a novel real-time feedback system for weld quality control of friction stir welding, with a 95% accuracy [16].

The BP algorithm has been used extensively, while the radial basis function (RBF) algorithm has been rarely used in welding and not all for FW. Therefore, it is necessary to select and compare the appropriate mathematical models which will be used to predict the effects of welding parameters on FW. Inertia friction welding (IFW), continuous drive friction welding (CDFW), and linear friction welding (LFW) are typical FW processes where two components stand against each other with relative motion under a pressure. It follows the subsequent local frictional heat generation and plastic deformation. When the softened thermal-plastic material yields to the welding pressure, a subsequent upset (i.e., axial shortening) of components happens. The original component surfaces will be broken up and extruded out to realize self-cleaning, and then the fresh metal organizes the new atomic contact to form a weld. Therefore, the upset is an important geometric feature for the precise friction welding. In this study, the RBF algorithm model of upset for each FW process has been developed using results of FE simulations of the process.

2. FE Model of IFW

A two-dimensional (2D) axisymmetric model was built, as shown in Figure 1, employing a tubular specimen of 30 mm length, inner diameter of 15 mm, and thickness of 4 mm [17]. The mesh was created using quad elements with coupled displacement-temperature and the twist degree of freedom. The mesh size was chosen to change over the length of the specimen as shown in Figure 1(b), to reduce computation time while maintaining accuracy of the results. Due to the extensive interfacial deformation in the IFW process, the remeshing and map solution techniques were used to overcome excessive element distortion. The self-contact option was also utilized to avoid early simulation abortion. Beside these, the actuator-sensor interaction and user element subroutines available in ABAQUS were adopted to measure transient flywheel rotational speed and upset.

The available energy for heating is equal to the flywheel kinetic energy E_0 , which can be expressed as

$$E_0 = \frac{1}{2}J\omega_0^2, \quad (1)$$

where J is the flywheel moment of inertia and ω_0 the initial flywheel rotational speed. Hence, energy conversion from flywheel kinetic energy to heat during friction can be described as

$$E_{t+\delta t} = E_t - \omega_t \delta t \int_S f_s r dS, \quad (2)$$

where ω_t is the rotational speed, δt the time increment, r the radial distance from the central axis, and S the range of r . The nominal friction force f_s can be divided into two stages to describe heat generation during the welding process according to Moal and Massoni [18]. When temperature is low, at the beginning of friction, friction stress is proportional to the prescribed pressure. With the friction continuing, interface temperature rises quickly and material flow stress

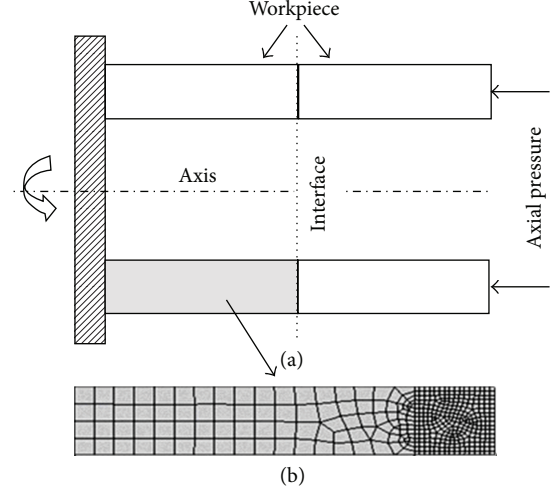


FIGURE 1: The geometry of IFW specimens (a) and meshed 2D axisymmetric model (b).

TABLE 1: Properties of GH4169 superalloy used in simulations [20].

Temperature ($^{\circ}\text{C}$)	20–1300
Young's modulus (GPa)	205–20
Thermal conductivity ($\text{W}\cdot\text{m}^{-1}\cdot\text{K}^{-1}$)	13.4–32.55
Specific heat capacity ($\text{J}\cdot\text{kg}^{-1}\cdot\text{K}^{-1}$)	430–720

decreases rapidly, with friction behavior f_s being defined as a thin Norton-Hoff layer subjected to a shear stress τ , which can be written as

$$\tau = -\alpha p \mu \frac{V_t}{|V_t|}, \quad (3)$$

where α is a constant, p the interface pressure, V_t the relative sliding velocity, and μ the nominal coefficient of friction.

The thermal conduction problem within the joint was solved using the 2D axisymmetric Fourier's heat conduction equation. In addition, heat dissipation through convection was also considered and a constant heat transfer coefficient of $30 \text{ W}\cdot\text{m}^{-2}\cdot\text{K}^{-1}$ was adopted to prescribe the boundary condition between joint surfaces and the environment [19].

2.1. Material Properties and Process Parameters. The temperature dependent material properties of the GH4169 superalloy were used in the finite element simulations. GH4169 according to the Chinese classifications, the same as Inconel 718, is a nickel-based superalloy with the following chemical composition by weight, 0.04% C, 0.13% Si, 0.10% Mn, 52.61% Ni, 18.95% Cr, 3.03% Mo, 5.14% Nb, 0.46% Al, 0.98% Ti, and balance Fe. The thermal and mechanical properties of GH4169 were drawn from literature [20], while some data at high temperatures were extrapolated from existing data, as shown in Table 1. The temperature dependent material flow stress data used in this simulation were drawn from literature [21, 22] as well as shown in Figure 2. In order to study the effects of axial pressure and initial rotational speed

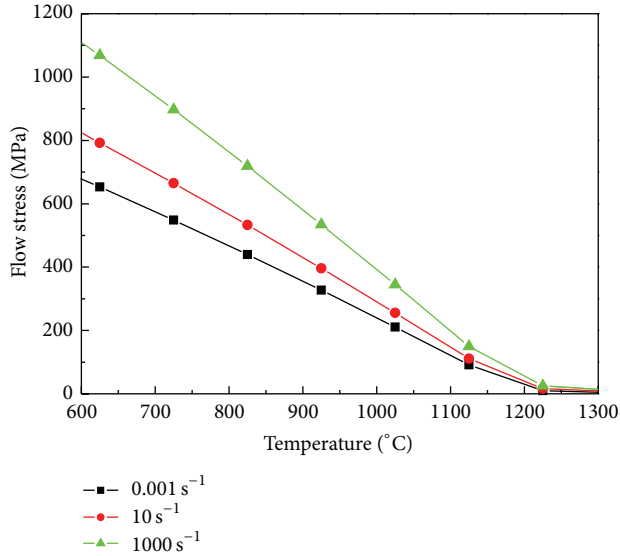


FIGURE 2: Temperature and strain rate dependent flow stress adopted in simulations.

TABLE 2: The IFW processing parameters studied.

Parameter	Value
Moment of inertia ($\text{kg}\cdot\text{m}^2$)	1.178
Axial pressure (MPa)	250, 300, 350, 375, 400, 450, 475, 500
Initial rotational speed (rad/s)	122.8, 132.8, 142.8, 152.8, 162.8

on the IFW process, finite element simulations were carried out using parameters as shown in Table 2.

3. Simulation Results

The simulation was conducted using the reported parameters of IFW of GH4169 superalloy tube by Yang et al. [17]. The moment of inertia, axial pressure, and initial rotational speed were $1.178 \text{ kg}\cdot\text{m}^2$, 400 MPa, and 152.8 rad/s, respectively.

The change of flywheel rotational speed is shown in Figure 3. It is clear that the rotational speed decreases linearly with time at the beginning of friction and decreases sharply just before the arrest of the flywheel. Meanwhile, there is no upset during the first 2 seconds of the process. Then, the upset increases almost linearly with friction time until $t = 4 \text{ s}$. It should be pointed out that the changing tendencies of these variables during IFW are relatively independent of the processing parameters, and the simulated final upset (6.2 mm) is comparable to experiments (about 5.7 mm) with an error of 8.7%. This validation enables the investigation of this parameter in the following sections and the effects of parameters on temperature field and upset as well.

Figure 4 shows temperature contours and upset variation at different welding times. With frictional movement, the heated zone widens from the weld interface due to the heat generated by friction, plastic deformation, and the heat conducted into the specimen. After the interface temperature

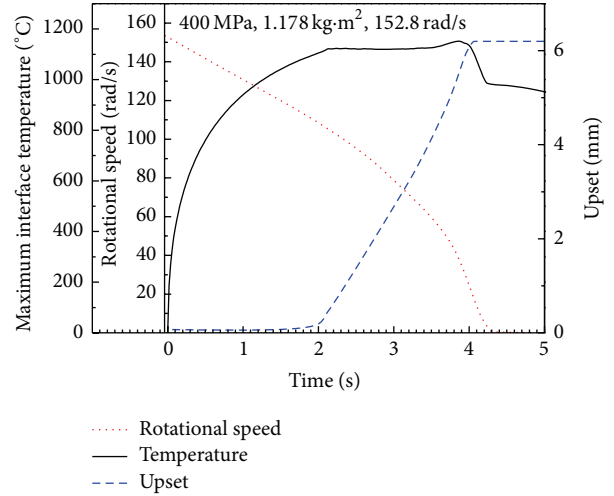


FIGURE 3: Variations of maximum interface temperature, rotational speed, and upset with welding time.

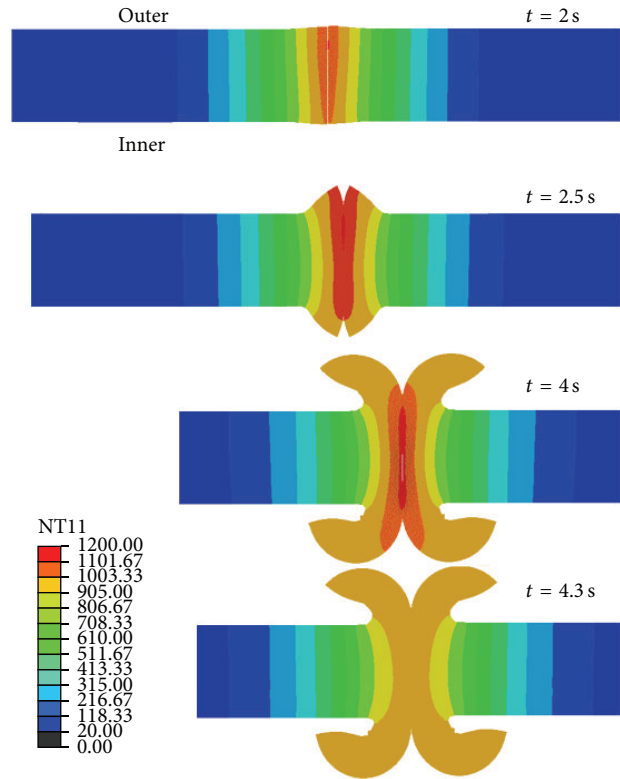


FIGURE 4: Temperature contours and upset variation at different welding times.

reaches about 1100°C at about 2 s (see Figure 4), temperature remains steady, which may suggest that a thermal balance between heat generation and dissipation has formed at the interface. At this time, the plastic material near the interface begins to extrude under axial pressure and a flash is formed (Figure 4, $t = 2.5 \text{ s}$). It is also found that temperature contours and flash shape are asymmetric, which is the result of the nonuniform linear velocity along the radial direction of the

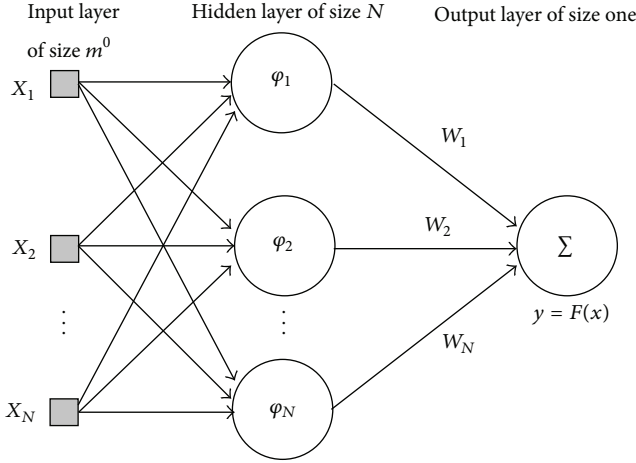


FIGURE 5: Structure of RBF neural network model.

specimen during welding which causes uneven heat generation. In addition, during IFW process, peak temperature at the interface is below the melting point of GH4169 (1260–1340°C).

When the welding time reaches about 4 s, the flash shape remains unchanged and the joint temperature begins to fall as shown in Figure 4. This can be clearly explained by studying the change of weld parameters, while the flywheel has a very small angular speed and the rotation completely stops at 4.3 s as shown in Figure 3. The upset remains constant after 4 s and the joint begins to cool down. The maximum interface temperature decreases quickly from about 1135°C to 980°C from 4 s to 4.3 s, and following this sharp decrease a less steep temperature decline follows. This sharp decrease of temperature is due to the fact that the thermal balance has been disturbed with quick heat dissipation by conduction from the interface to the cold end of specimen being much larger than the small or no heat generation at the interface at this stage.

4. Mathematical Prediction Model Settings

The RBF neural network is commonly used in functional approximation, spline interpolation, and mixed models [23]. The developed RBF neural network is composed of three layers of nodes as shown in Figure 5. The first layer is the input layer that feeds in input or training data to the second layer, which is a hidden layer. This second layer differs greatly from commonly used neural networks as each node represents a data cluster centered at a particular point and has a given radius. The final layer consists of only one node so as to output the second layer of nodes and yield a decision value.

In fact, the upset prediction can be viewed as an interpolation problem, which can be stated as follows.

Given a set of N different points $\{\mathbf{x}_i \in R^{m_0} \mid i = 1, 2, \dots, N\}$ and a corresponding set of N real numbers $\{d_i \in R^1 \mid i = 1, 2, \dots, N\}$, a function $F: R^N \rightarrow R^1$ is necessary to be found that satisfies the interpolation condition

$$F(\mathbf{x}_i) = d_i, \quad i = 1, 2, \dots, N. \quad (4)$$

For a strict interpolation, the interpolating surface (function F) should pass through all training data points.

The RBF technique consists of choosing a function F of the form

$$F(\mathbf{x}) = \sum_{i=1}^N w_i \varphi(\|\mathbf{x} - \mathbf{x}_i\|), \quad (5)$$

where w_i is the weight function at node \mathbf{x}_i and $\{\varphi(\|\mathbf{x} - \mathbf{x}_i\|) \mid i = 1, 2, \dots, N\}$ is a set of N arbitrary (generally nonlinear) functions, known as radial basis functions as

$$\varphi_i(\mathbf{x}) = \varphi(\|\mathbf{x} - \mathbf{x}_i\|) = \exp\left(-\frac{\|\mathbf{x} - \mathbf{x}_i\|^2}{2\sigma^2}\right), \quad i = 1, 2, \dots, N, \quad (6)$$

where $\|\mathbf{x} - \mathbf{x}_i\|$ denotes a norm that is usually Euclidean. The down data points $\mathbf{x}_i \in R^{m_0}$, $i = 1, 2, \dots, N$ are taken to be the centers of the radial basis functions.

According to the interpolation conditions, a set of simultaneous linear equations for the unknown coefficients (weights) of the expansion $\{w_i\}$ are obtained

$$\begin{bmatrix} \varphi_{11} & \varphi_{12} & \dots & \varphi_{1N} \\ \varphi_{21} & \varphi_{22} & \dots & \varphi_{2N} \\ \vdots & \vdots & \vdots & \vdots \\ \varphi_{N1} & \varphi_{N2} & \dots & \varphi_{NN} \end{bmatrix} \begin{bmatrix} w_1 \\ w_2 \\ \vdots \\ w_N \end{bmatrix} = \begin{bmatrix} d_1 \\ d_2 \\ \vdots \\ d_N \end{bmatrix}, \quad (7)$$

where

$$\varphi_{ij} = \varphi(\|\mathbf{x}_i - \mathbf{x}_j\|), \quad i, j = 1, 2, \dots, N. \quad (8)$$

Let

$$\mathbf{d} = [d_1, d_2, \dots, d_N]^T, \quad (9)$$

$$\mathbf{w} = [w_1, w_2, \dots, w_N]^T.$$

The N -by-1 vectors \mathbf{d} and \mathbf{w} represent the desired response vector and linear weight vector, respectively, where N is the size of the training sample. Let Φ denote an N -by- N matrix with elements φ_{ij} as follows:

$$\Phi = \{\varphi_{ij}\}_{i,j=1}^N. \quad (10)$$

This is the interpolation matrix. Then (12) can be rewritten in a compact form

$$\Phi \mathbf{w} = \mathbf{b}. \quad (11)$$

Assuming that Φ is nonsingular, then

$$\mathbf{w} = \Phi^{-1} \mathbf{b}. \quad (12)$$

Normally, training and testing points (x_{ij}) must be normalized within a range to enhance the efficiency of the model. In this paper, training and testing data are linearly normalized to a range of -1 to 1 by (13), and the output data are reverse normalized,

$$\bar{x}_{ij} = \frac{2 \times [x_{ij} - \min(x_{ij})]}{[\max(x_{ij}) - \min(x_{ij})]} - 1, \quad (13)$$

where x_{ij} is the normalized data and x_{ij} the training and testing points.

TABLE 3: The final upsets under different IFW processing parameters.

No.	Parameters		Upset (mm)
	Axial pressure (MPa)	Initial rotational speed (rad/s)	
1	350	122.8	0.13
2	375	122.8	0.73
3	400	122.8	1.36
4	350	132.8	1.40
5	375	132.8	2.15
6	400	132.8	2.85
7	250	142.8	0.01
8	300	142.8	1.18
9	350	142.8	2.99
10	375	142.8	3.78
11	400	142.8	4.53
12	450	142.8	5.76
13	475	142.8	6.31
14	500	142.8	6.86
15	250	152.8	0.51
16	300	152.8	2.80
17	350	152.8	4.73
18	375	152.8	5.51
19	400	152.8	6.20
20	450	152.8	7.47
21	475	152.8	8.06
22	500	152.8	8.56
23	250	162.8	2.12
24	300	162.8	4.70
25	350	162.8	6.46
26	375	162.8	7.24
27	400	162.8	7.99
28	450	162.8	9.18
29	475	162.8	9.86
30	500	162.8	11.50

5. Results and Discussion

30 sets of final upsets under different IFW processing parameters are shown in Table 3, which were used to build and train the RBF neural network. Following extensive optimization, it was found that an RBF neural network with 25 neurons in the hidden layer gives the best prediction of the upset. The performance mean squared error of this neural network model at the end of training is shown in Figure 6. The surface plot of the RBF predicted upset as a function of axial pressure and initial rotational speed is shown in Figure 7. Upset ranging from 0 to 15 mm can be clearly seen when axial pressure and initial rotational speed change from 200 MPa to 500 MPa and from 120 rad/s to 200 rad/s, respectively. This can be useful in parameter selection and upset prediction of IFW.

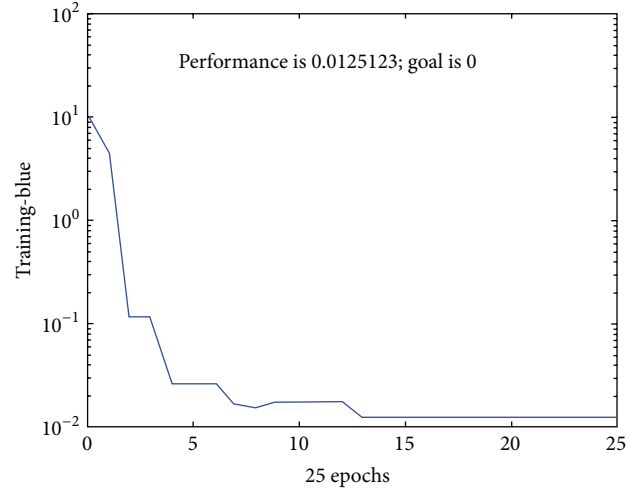


FIGURE 6: Mean squared error of the network to predict upset of IFW.

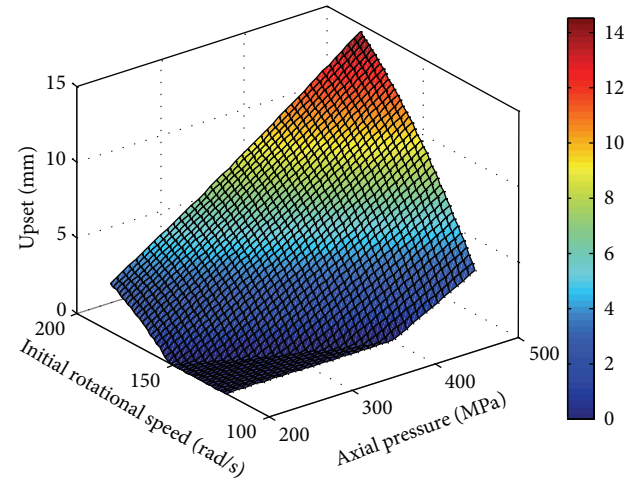


FIGURE 7: Surface plot of prediction results by RBF network.

To explore the feasibility of using such a network and the precision of its predictions, another 9 sets of FE simulated data, not used in the initial neural network training, were produced. The comparison between FE simulated upsets and RBF predicted ones and the relative error is shown in Table 4. It is clear that the RBF predicted values are close to the ones produced by the finite element model, with an acceptable absolute error of less than 0.3 mm. However, it also can be found that a frustrating large relative error of 8.16% existed at the condition of 300 MPa-147.8 rad/s, although a normal absolute error (0.16 mm) is obtained. This is probably because of the limited training data of the RBF network.

From the surface plot of prediction results as shown in Figure 7, both the initial rotational speed and axial pressure greatly affect final upset. As the total welding heat for IFW should be converted from the flywheel kinetic energy, the initial flywheel kinetic energy is assumed to be a special parameter which affects the welding process. There is a proportional relationship between the flywheel kinetic energy,

TABLE 4: Comparison between FE simulated upsets and RBF predicted ones.

No.	Condition	Upset (mm)		Absolute error (mm)	Relative error (%)
		FE simulated	RBF predicted		
1	300 MPa—147.8 rad/s	1.96	2.12	0.16	8.16
2	300 MPa—157.8 rad/s	3.72	3.64	0.08	2.15
3	300 MPa—167.8 rad/s	5.53	5.23	0.30	5.42
4	400 MPa—147.8 rad/s	5.38	5.35	0.03	0.56
5	400 MPa—157.8 rad/s	7.09	7.06	0.03	0.42
6	400 MPa—167.8 rad/s	8.75	8.83	0.08	0.91
7	500 MPa—147.8 rad/s	7.72	7.64	0.08	1.04
8	500 MPa—157.8 rad/s	9.43	9.54	0.11	1.17
9	500 MPa—167.8 rad/s	11.63	11.5	0.13	1.12

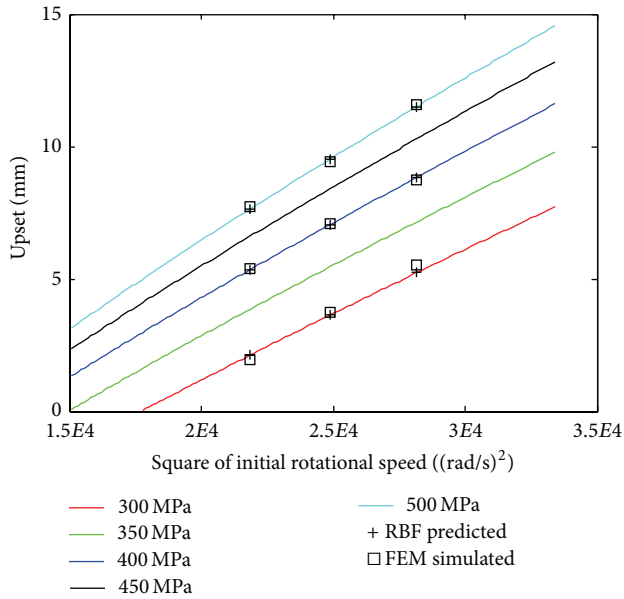


FIGURE 8: Effect of square of initial rotational speed on upset predicted by RBF network.

and the square of initial rotational speed, with the effect of flywheel kinetic energy on the upset shown in Figure 8. There is very good agreement between RBF network predicted and FE simulated upset as shown in Table 4 and plotted in Figure 8. Furthermore, there exists a clear linear relationship between upset and the square of initial rotational speed which means that the final upset is almost predetermined by flywheel initial kinetic energy, when axial pressure is constant.

However, it should also be noted that there is almost no upset under 300 MPa and when the square of initial rotational speed is smaller than 17689 (rad/s)^2 (i.e., speed of 133 rad/s), suggesting that insufficient deformation develops at the interface. In a similar fashion, when axial pressure increases, there is also a low threshold of acceptable initial rotational speed necessary to produce the upset for a given axial pressure.

5.1. Effect of Axial Pressure on Upset. The effect of axial pressure on the upset was investigated and the results predicted

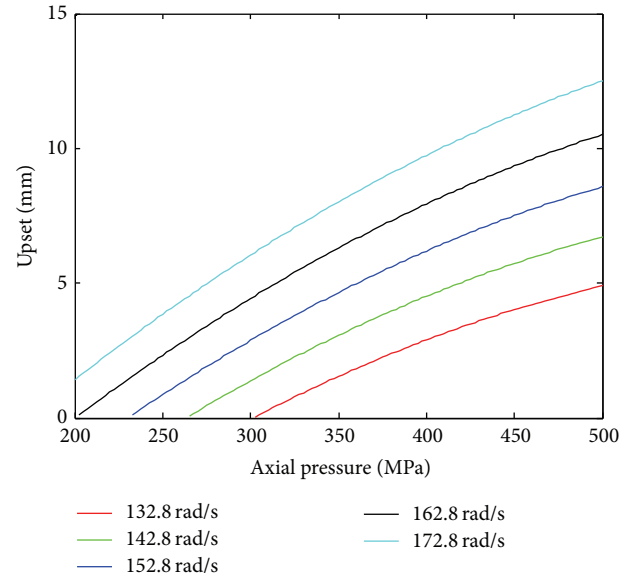


FIGURE 9: Effect of axial pressure on upset predicted by RBF network.

by the RBF network are shown in Figure 9. One can see an exponentially increasing relationship between upset and axial pressure at different initial rotational speeds. It indicates that the upset changes more rapidly under relative low axial pressure which is not the case under relatively high axial pressure. Similar to the effect of initial rotational speed, the underlying mechanism of axial pressure on the upset can also be found in energy conversion.

For example at the initial rotational speed of 142.8 rad/s, there is almost no upset under an axial pressure smaller than 265 MPa, while the upset reaches 5 mm under 420 MPa. According to the principle of IFW, the rotated flywheel is the sole mechanical energy source for welding, and the total energy for welding is up to its initial rotational speed. Thus the most appropriate expression for the upset change could be that the axial pressure affects significantly the efficiency of the conversion of mechanical energy to effective heat. Although the available flywheel kinetic energy is sufficient, it is difficult to heat rapidly (i.e., effective heat) at the interface and yield locally the workpiece under a relative low axial

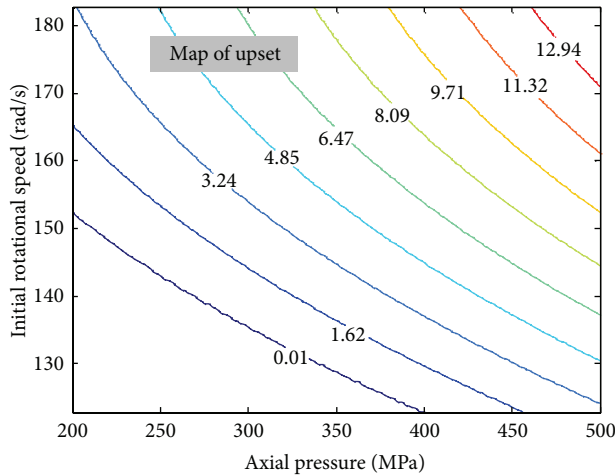


FIGURE 10: Parameter window based on the predicted upset by RBF network.

pressure. Therefore, in a similar fashion to critical initial rotational speed, there is a critical axial pressure for each initial rotational speed whose finding is necessary for process parameter selection.

In fact, insufficient deformation (small upset) during IFW is generally considered as the reason for lacking of bonding, weak self-cleaning, and severe oxidation. According to Ates et al. [24], a serious decrease in the tensile strength of friction welded joints could be attributed to insufficient deformation under low axial pressure.

Moreover, according to the results above, the RBF network predicts the critical welding parameters. To further develop the capability of the RBF network, the parameter prediction window was established based on the upset as shown in Figure 10. With a given upset, continuously changed welding parameters could be obtained from the prediction window for the studied workpiece in this study. Therefore, the RBF network could be helpful to predict and select processing parameters of IFW.

5.2. Applications to LFW and CDFW. In published works [19, 25], simulations of CDFW and LFW have been conducted with FE models. The effects of processing parameters on temperature profile and upset have been explored in a systematic way. Based on these simulations, applications of RBF network on LFW and CDFW have been attempted.

In literature [25], a 2D thermomechanically coupled finite element model of LFW TC4 titanium alloy was built and heat generation was produced due to friction between deformable and rigid surfaces. Using this model, the effect of most important parameters, such as oscillation frequency, amplitude, and friction pressure, on temperature profile and upset were examined. As a result, a mathematical upset prediction model was established in this study. A correlation coefficient (R^2) of 0.963 for the scatter diagram of RBF prediction versus actual upset (of the simulated results) was obtained as shown in Figure 11.

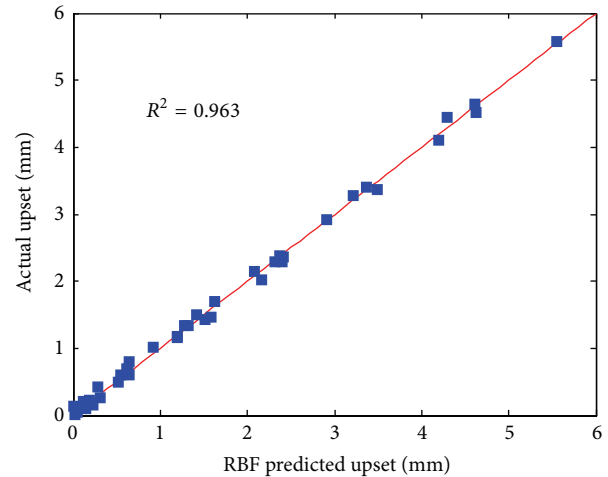


FIGURE 11: Scatter diagram of RBF prediction versus actual upset of LFW.

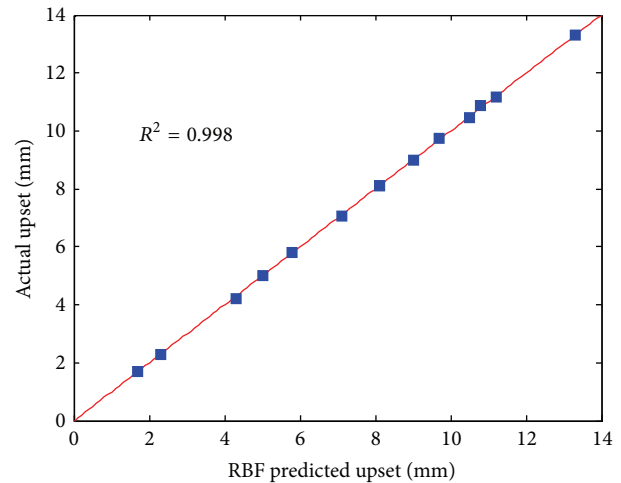


FIGURE 12: Scatter diagram of RBF prediction versus actual upset of CDFW.

In addition, the FE simulation of the CDFW process has also been developed using a 2D axisymmetric thermal-mechanically coupled model, of a mild steel bar with a length of 150 mm and diameter of 20 mm. Furthermore, experimental and calculated upsets show an error of only 2.5%. Based on simulations using parameters provided in literature [19], a similar RBF regression analysis for the CDFW case has been obtained. The scatter diagram of RBF prediction versus actual upset (of the FE simulated results) shows a correlation coefficient of 0.998 in Figure 12. Therefore, the RBF neural network model can also be used to predict the outputs of LFW and CDFW with a significant accuracy.

6. Conclusions

According to the analysis in this paper, the following conclusions can be drawn.

- (1) The finite element modeling of IFW: a superalloy can well reveal the friction and upsetting processes. Based on these simulations, an RBF neural network was applied initially to establish a welding parameter prediction window based on the upset.
- (2) The developed RBF network model shows that there is a critical axial pressure for acceptable upset for each initial rotational speed. Similarly, there is also a critical initial rotational speed, that is, critical flywheel kinetic energy, for each axial pressure.
- (3) Depending on the energy conversion, the analysis of effects of IFW parameters on the upset indicates that the initial rotational speed determines the heat source and that axial pressure will significantly affect the heat accumulation at the weld interface.
- (4) Applications of the RBF network on LFW and CDFW were also developed, with correlation coefficients for LFW and CDFW being 0.963 and 0.998, respectively, suggesting that RBF is an effective prediction method for friction welding.

Conflict of Interests

The authors declare that they do not have a direct relation with any commercial identities that might lead to a conflict of interests for any of them.

Acknowledgments

The authors would like to thank for financial support the National Natural Science Foundation of China (51005180 and 61065009) and the III Project (B08040).

References

- [1] M. Maalekian, "Friction welding—critical assessment of literature," *Science and Technology of Welding and Joining*, vol. 12, no. 8, pp. 738–759, 2007.
- [2] F. M. Ham and I. Kostanic, *Principles of Neurocomputing for Science and Engineering*, McGraw-Hill, New York, NY, USA, 1 edition, 2001.
- [3] S. C. Juang, Y. S. Tarng, and H. R. Li, "A comparison between the back-propagation and counter-propagation networks in the modeling of the TIG welding process," *Journal of Materials Processing Technology*, vol. 75, no. 1–3, pp. 54–62, 1998.
- [4] B. Chan, J. Pacey, and M. Bibby, "Modelling gas metal arc weld geometry using artificial neural network technology," *Canadian Metallurgical Quarterly*, vol. 38, no. 1, pp. 43–51, 1999.
- [5] J. Y. Jeng, T. F. Mau, and S. M. Leu, "Prediction of laser butt joint welding parameters using back propagation and learning vector quantization networks," *Journal of Materials Processing Technology*, vol. 99, no. 1, pp. 207–218, 2000.
- [6] D. S. Nagesh and G. L. Datta, "Prediction of weld bead geometry and penetration in shielded metal-arc welding using artificial neural networks," *Journal of Materials Processing Technology*, vol. 123, no. 2, pp. 303–312, 2002.
- [7] K. H. Christensen, T. Sørensen, and J. K. Kristensen, "Gas metal arc welding of butt joint with varying gap width based on neural networks," *Science and Technology of Welding and Joining*, vol. 10, no. 1, pp. 32–43, 2005.
- [8] P. Ghanty, M. Vasudevan, D. P. Mukherjee et al., "Artificial neural network approach for estimating weld bead width and depth of penetration from infrared thermal image of weld pool," *Science and Technology of Welding and Joining*, vol. 13, no. 4, pp. 395–401, 2008.
- [9] M. Vasudevan, V. Arunkumar, N. Chandrasekhar, and V. Maduraimuthu, "Genetic algorithm for optimisation of A-TIG welding process for modified 9Cr-1Mo steel," *Science and Technology of Welding and Joining*, vol. 15, no. 2, pp. 117–123, 2010.
- [10] G. Casalino, S. J. Hu, and W. Hou, "Deformation prediction and quality evaluation of the gas metal arc welding butt weld," *Proceedings of the Institution of Mechanical Engineers B*, vol. 217, no. 11, pp. 1615–1622, 2003.
- [11] S. Pal, S. K. Pal, and A. K. Samantaray, "Artificial neural network modeling of weld joint strength prediction of a pulsed metal inert gas welding process using arc signals," *Journal of Materials Processing Technology*, vol. 202, no. 1–3, pp. 464–474, 2008.
- [12] B. Acherjee, S. Mondal, B. Tudu, and D. Misra, "Application of artificial neural network for predicting weld quality in laser transmission welding of thermoplastics," *Applied Soft Computing Journal*, vol. 11, no. 2, pp. 2548–2555, 2011.
- [13] H. Okuyucu, A. Kurt, and E. Arcaklioglu, "Artificial neural network application to the friction stir welding of aluminum plates," *Materials and Design*, vol. 28, no. 1, pp. 78–84, 2007.
- [14] P. Sathiyaa, S. Aravindan, A. N. Haq, and K. Paneerselvam, "Optimization of friction welding parameters using evolutionary computational techniques," *Journal of Materials Processing Technology*, vol. 209, no. 5, pp. 2576–2584, 2009.
- [15] S. S. Kumaran, S. Muthukumaran, and S. Vinodh, "Optimization of friction welding of tube to tube plate using an external tool by hybrid approach," *Journal of Alloys and Compounds*, vol. 509, no. 6, pp. 2758–2769, 2011.
- [16] E. Boldsaiikhan, E. M. Corwin, A. M. Logar, and W. J. Arbegast, "The use of neural network and discrete Fourier transform for real-time evaluation of friction stir welding," *Applied Soft Computing Journal*, vol. 11, no. 8, pp. 4839–4846, 2011.
- [17] J. Yang, S. N. Lou, Y. Zhou, J. M. Yan, and W. Q. Shi, "The dynamic recrystallization properties of superalloy GH4169 inertia friction welding joint," *Journal of Aeronautical Materials*, vol. 22, no. 2, pp. 8–11, 2002 (Chinese).
- [18] A. Moal and E. Massoni, "Finite element simulation of the inertia welding of two similar parts," *Engineering Computations*, vol. 12, no. 6, pp. 497–512, 1995.
- [19] W. Y. Li and F. F. Wang, "Modeling of continuous drive friction welding of mild steel," *Materials Science and Engineering A*, vol. 528, no. 18, pp. 5921–5926, 2011.
- [20] L. W. Zhang, J. B. Pei, Q. Z. Zhang et al., "The coupled fem analysis of the transient temperature field during inertia friction welding of GH4169 alloy," *Acta Metallurgica Sinica*, vol. 20, no. 4, pp. 301–306, 2007.
- [21] M. S. Lewandowski and R. A. Overfelt, "High temperature deformation behavior of solid and semi-solid alloy 718," *Acta Materialia*, vol. 47, no. 18, pp. 4695–4710, 1999.
- [22] J. J. DeMange, V. Prakash, and J. M. Pereira, "Effects of material microstructure on blunt projectile penetration of a nickel-based super alloy," *International Journal of Impact Engineering*, vol. 36, no. 8, pp. 1027–1043, 2009.

- [23] M. P. Phaniraj and A. K. Lahiri, "The applicability of neural network model to predict flow stress for carbon steels," *Journal of Materials Processing Technology*, vol. 141, no. 2, pp. 219–227, 2003.
- [24] H. Ates, M. Turker, and A. Kurt, "Effect of friction pressure on the properties of friction welded MA956 iron-based superalloy," *Materials and Design*, vol. 28, no. 3, pp. 948–953, 2007.
- [25] W. Y. Li, T. Ma, and J. Li, "Numerical simulation of linear friction welding of titanium alloy: effects of processing parameters," *Materials & Design*, vol. 31, no. 3, pp. 1497–1507, 2010.